INTERACTIONS BETWEEN COMPRESSIBLE FLUIDS AND STRUCTURES UNDER MECHANICAL ABUSE

By

Fuming Yang

A DISSERTATION

Submitted to
Michigan State University
in partial fulfillment of the requirements
for the degree of

Civil Engineering – Doctor of Philosophy

2024

ABSTRACT

Energy absorption materials and structures have been extensively used for protecting personnel and infrastructure against collisions, explosions, and impacts. Current existing energy-absorbing materials and structures, such as foams, honeycombs, composites, and thin-walled structures, possess attractive physical and mechanical properties including extreme lightweight, large deformability and easy fabrication. They play a crucial role in enhancing safety measures across various sectors, including transportation, construction, and defense. However, the performance of these materials and structures is susceptible to structural defects, which act as the weakest chain of the system and weaken the overall efficiency. Multiple materials and structures, such as the foam-filled thin-walled tubes, have been combined to further enhance the energy absorption performance. Nevertheless, the bonding strength between dissimilar materials often limits this improvement, as debonding occurs between filler and tube wall under large deformation. Moreover, current solid-based materials lack biocompatibility, preventing direct application for protecting biological tissues.

To address above issues, compressible fluids, specifically liquid nanofoam (LN) and suspension hollow glass microsphere (SHGM) have been developed. The LN system, comprising a liquid phase and hydrophobic nanoporous particles, utilizes pressurized liquid flow in nano-channels as its energy absorption mechanism. The SHGM system, consisting of a liquid phase and hollow glass microspheres, dissipates substantial energy as particles collapse within the pressurized liquid surrounding them. The central hypothesis of this study is that not only the high energy absorption efficiency of compressible fluids, but also the strong interaction between these fluids and the surrounding structures can significantly enhance the energy absorption performance.

To test this hypothesis, this dissertation presents a systematic experimental study on the

interaction between compressible fluids and three different types of structures, specifically structures without imperfections, structures with imperfections, and biostructures. The interaction between compressible fluids and perfect thin-walled tubes has been quantified by an extraordinary strengthening coefficient of 4.3, surpassing achievements by existing solid foam fillers. In addition, compressible fluids are able to mitigate the negative effects of structural imperfections, as the energy absorption capacity of thin-walled tubes filled with compressible fluids is inert from the presence of structural defects. Furthermore, it has been demonstrated that compressible fluids, specifically LN, exhibit excellent biocompatibility and energy absorption efficiency, allowing them to directly interact with biotissues and effectively protect cells and organs from mechanical abuse.

In conclusion, compressible fluids are effective fluid energy absorbers not only due to their high energy absorption efficiency but also because of the strong interactions they form with surrounding structures. Their large deformability and excellent biocompatibility enable direct interact with engineering and biological structures with a wide range of mechanical properties. The scientific findings of this study represent a paradigm shift in designing next generation of advanced energy absorption materials and structures.

To my parents for endless love and support
To Shengyuan Bai, for all kinds of encouragement and understanding.

ACKNOWLEDGEMENTS

The successful completion of this dissertation owes a debt of gratitude to a multitude of individuals whose support and contributions were indispensable.

First and foremost, I would like to express my sincere gratitude to my advisor, Prof. Weiyi Lu, for his guidance, encouragement, and support during my Ph.D. studies. I am profoundly grateful for the invaluable training and resources he provided, which empowered me to navigate the path toward becoming an autonomous and industrious researcher. His significant efforts in refining my manuscripts and presentations, attention to inconspicuous results, and strong desire to reveal the underlying science have inspired my dedication to excellence in both research and life. I am truly honored to have such a great advisor in the pursuit of my Ph.D. degree.

I am deeply indebted to my co-advisor, Prof. Yun Liang, whose exceptional expertise and guidance in her field played a pivotal role in ensuring the efficient resolution of challenges encountered throughout my research journey. Prof. Liang's profound understanding and quick insights not only facilitated the smooth execution of experiments but also significantly enhanced the quality and depth of our findings. Her timely feedback and astute observations were instrumental in steering the course of our investigations toward fruitful outcomes. Furthermore, I wish to express my heartfelt gratitude for Prof. Liang's unwavering support and dedication in meticulously refining our papers. Her keen eye for detail and valuable suggestions greatly enriched the clarity and coherence of our research contributions. Additionally, her encouragement and constructive feedback served as a constant source of motivation, inspiring me to strive for excellence in every aspect of my academic pursuits.

I would also like to extend my sincere thanks to my colleagues and friends, whose encouragement, camaraderie, and shared insights have been invaluable throughout this journey,

Dr. Mingzhe Li, Dr. Chi Zhan, Dr. Lijiang Xu, Dr. Jisheng Chen, Ms. Anqi Zheng, Ms. Runqi Zhu, Ms. Yilin Nie, Mr. Kam Kennicott, Mr. Robert, Bennett, Mr. Michael Schoen, Dr. Per Askeland, Dr. Melinda Frame, Mrs. Abigail Vanderberg, Mrs. Amy Albin, Mrs. Laura Post, Ms. Bailey Weber. I would also like to express my thanks to Dr. Robert McCoy, Mr. Dean Jaradi at Ford Motor Company, for their help and support of my NSF-INTERN experience.

I would like to acknowledge the financial supports from the National Science Foundation (award #1803695) and the Ford-MSU alliance program for my research.

Last but certainly not least, I wish to express my deepest gratitude to my family for their unwavering support and encouragement throughout this journey. To my esteemed parents, Changnian Yang and Zhongjie Feng, your boundless love, unwavering guidance, and steadfast belief in my abilities have served as the cornerstone of my resilience and determination. From instilling in me the value of hard work to nurturing my aspirations, your unwavering dedication has been the guiding light illuminating my path forward.

Above all, I owe an immeasurable debt of gratitude to my boyfriend, Shengyuan Bai. His boundless love, unwavering support, endless patience, and constant encouragement have been the cornerstone of my inspiration and drive.

TABLE OF CONTENTS

Chapter 1 Introduction

1.1 Motivation

Energy absorption materials and structures such as thin-walled structures [1–3], sandwich panels [4,5], plates [6,7], foams [8–14], and bio-inspired materials [15] have been widely used in contact sports to mitigate personal injuries, and in ground vehicles to enhance the crashworthiness of vehicles [16] (Fig. 1-1). With the impact of technology on today's fast-paced society, advanced energy absorption materials structures are needed. According to data from the National Safety Council (NSC), the total motor-vehicles death number was 42,339 in 2020, within which 41.3% cases were related to crashes with other motor vehicles (Fig. 1-2). In addition, the number of annual registered motor vehicles in the US increased from 218 million in 2000 to 290 million in 2020 with a steady increase rate of 13% [17].

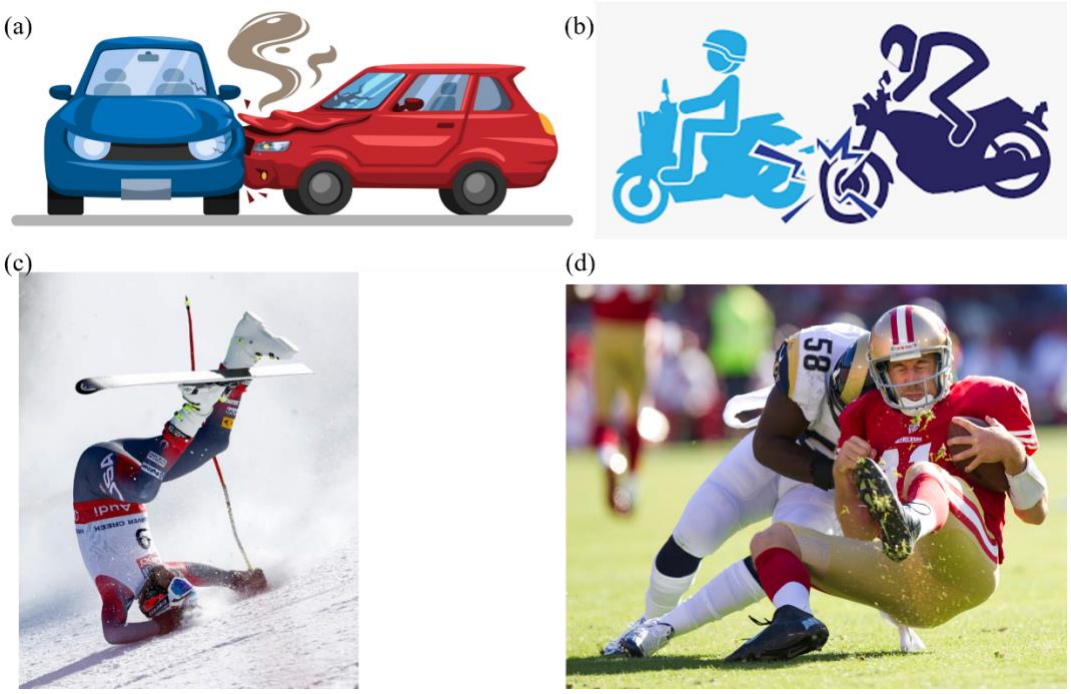

Figure 1-1: Collisions in (a) car accidents, (b) motorcycles, (c) skiing, and (d) American football.

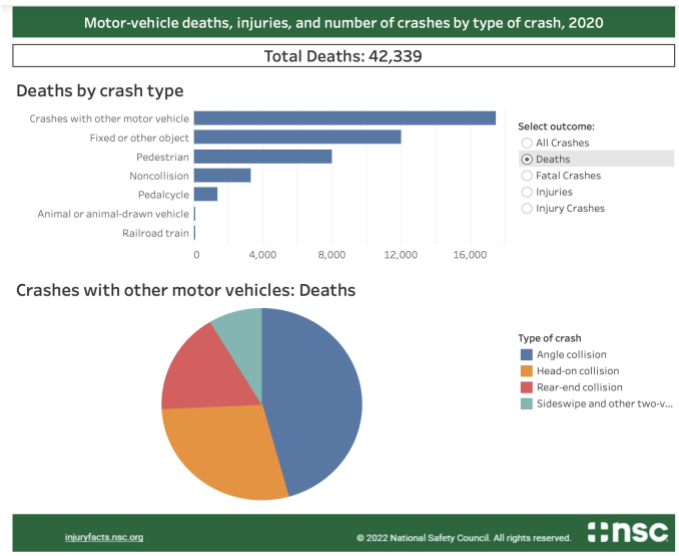

Figure 1-2: Death numbers in 2020 by type of crashes (NSC).

In the field of sports like American football, skiing, ice hockey, boxing, and auto racing, helmets, gloves, and other protective gears are used to prevent athletes from injuries, especially concussions. For instance, skiing and snowboarding are popular winter sports in the United States, with 10.3 million participants and 59.3 million visits to U.S. ski resorts in the 2018/2019 season alone[19]. Over the past decade, more people have started wearing helmets, with 81-90% of participants in ski resorts now using them. However, head injuries, including traumatic brain injuries (TBIs), are still a major concern. Despite the increase in helmet use, the rate of head injuries hasn't gone down significantly. About 15-20% of the 600,000 annual snow sport injuries in North America involve head injuries. Among younger participants, TBIs are the main cause of fatalities, accounting for 67% of cases [20,21].

From 2017-2021, the National Football League (NFL) players wearing top-performing helmets increased from 41% to 99% [22]. However, the concussion cases only dropped by 33% [23]. These facts suggest that current energy absorbing liners are still far from satisfactory for the prevention of concussion.

TBI is a common type of blunt force trauma (BFT), wherein damage to the brain can lead to long-term cognitive, physical, or emotional impairments. Other types of BFT such as blunt abdominal trauma are also common consequences of collisions in auto accidents and sports fields, which can cause failure or rupture of vital organs such as liver, kidneys, heart and lungs. It is expected that BFT will become the 3rd largest contributor to the burden of disease with 46,980 deaths and 5.4 million injuries caused by motor vehicle crashes in 2021 alone [24]. However, the performance of current materials is still far from satisfactory for protecting against BFT.

This research project aims to develop novel fluid-based energy absorption material systems with much higher energy absorption efficiency. Firstly, the mechanical behavior of these compressible fluids sealed in thin-walled structures with or without structural defects has been investigated under both quasi-static and dynamic tests. Secondly, it has been demonstrated that the interaction between the compressible fluids and the thin-walled structures is much stronger than solid-solid systems, which significantly improves the energy absorption performance and stability of the energy absorption material systems. Lastly, the interaction between the developed fluid-based energy absorption material systems has been proven effective in protecting biological tissues at both cellular and organ scales in BFT.

1.2 Current Challenges

Current existing energy materials, including foams, composites and bio-inspired materials have the following three main challenges.

Challenge 1 – Drawbacks of Current Energy Absorption Materials

Solid foams such as metallic foam such as aluminum foam [25] (Fig. 1-3a) and polymeric foam [26,27] (Fig. 1-3b) are widely used for energy absorption. The working mechanism is based on the buckling and bending of structural members [28,29]. Polymeric foams such as polypropylene and

polyurethane foams, have limited capability to absorb energy under mechanical abuse because of the low working pressure. Therefore, most of the input energy is transmitted to the protected object [30]. To increase the energy absorption efficiency, stronger or density-graded metallic foams [31,32] are developed. However, the increased stiffness of the cell structure and the strain rate effect require relatively large stress to initiate the energy absorption process, which makes those foams not ideal for the protection of soft tissues. Under high strain rate impact condition, the foams cannot response immediately to respond to the external mechanical abuse, and thus have much lower efficiency in energy absorption.

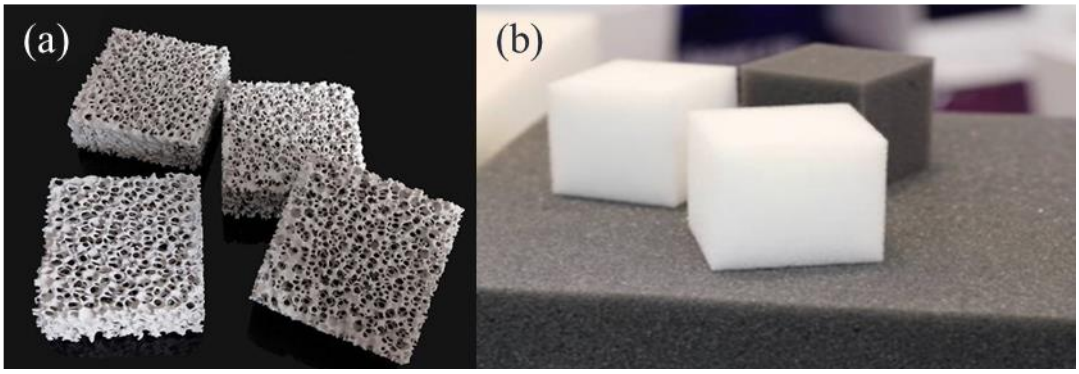

Figure 1-3: (a) Aluminum foam (copyright: Wuxi Forest Trade Co., Ltd), (b) Polymer foam (copyright: Gautam ZEN UK LTD).

Natural livings like plants [33,34], insects and animals often possesses many unique structures to protect themselves from mechanical abuse (Fig. 1-4). Those biological structures usually have high energy absorption efficiency, high strength and low density [35]. Inspired by these natural structures, novel structures for energy absorbers have been designed [36,37] (Fig. 1-5). However, the extraordinary mechanical properties of biological structures are achieved by the natural processing of the complex multiscale microstructures. It is extremely challenging to mimic the complicated microstructures through the conventional manufacturing processes. Even with the aid of additive

manufacturing [36], it is challenging to achieve the manufacturing resolution and the complex structural design at smaller length scale.

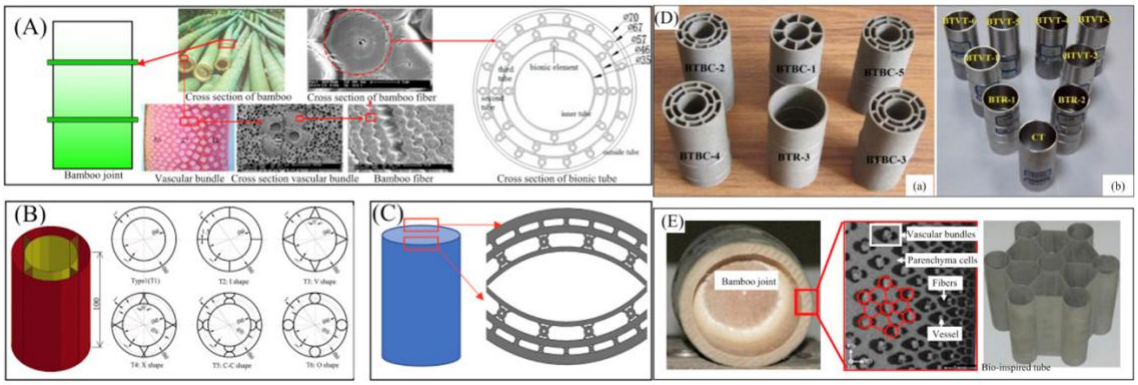

Figure 1-4: Bamboo-inspired structures. (a) with the bionic element close to the vascular structures, (b) with different bionic elements, (c) with modified bionic element, (d) with simplified bionic element, (e) novel bionic elements [38].

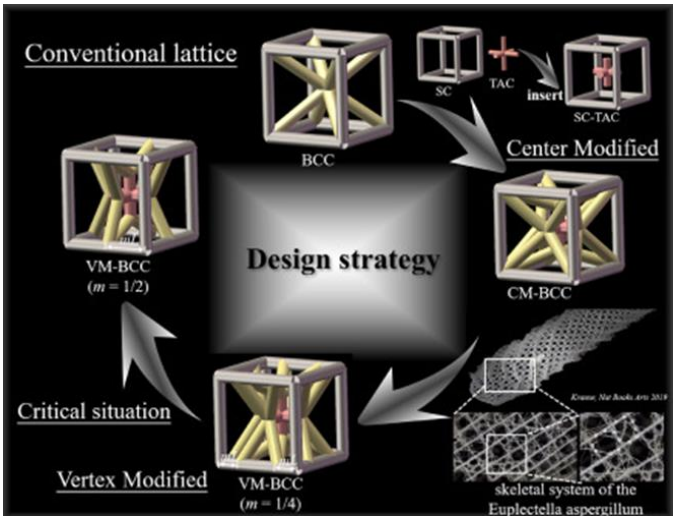

Figure 1-5: Schematics of the design strategy partially inspired by the skeletal system of deep-sea glass sponge (Euplectella aspergillum), from conventional BCC lattice to center modified BCC (CM-BCC) lattice to vertex modified BCC (VM-BCC) lattice.

Challenge 2 – Negative Effect of Structural Defects

The energy absorption performance as well as other mechanical properties are highly dependent on the structural integrity. It has been demonstrated that the load carrying capacity, the post-buckling strength and the energy absorption capacity of structures are significantly compromised when structural imperfections exist [39–44]. Unfortunately, structural imperfections are

inevitably introduced during the manufacturing, transporting, and handling processes. In addition, the structural imperfection significantly reduces the service life and can lead to unexpected sudden failure of the structures. There is lack of solutions to effectively suppress the negative impact of structural imperfections on the mechanical performance.

Challenge 3 – Poor Soft Tissue Protection

Traumatic brain injuries caused by head-to-head collisions in the sports of ice hockey and American football (Fig. 1-6a and b) are an important public health issue. It is necessary to develop headgear to prevent brain injuries [45–47], which is extremely challenging as bio-tissues can be damaged at a pressure in the range of 0.1-0.2 MPa [48]. The current headgear liners are made of polymeric cellular materials [49]. However, medical studies have shown that the presence of padded headgear does not reduce the rate of head injuries [50–52]. This is because traditional solid energy absorption materials are too rigid and robust to effectively protect biological tissues from mechanical abuse.

Additionally, forceful impacts like falls and motor vehicle crashes can cause serious injuries to vital organs, potentially leading to life-threatening situations [53]. About 65% of severe trauma cases involve organs such as the liver, kidneys, heart, and lungs, requiring urgent medical attention and possibly resulting in long-term complications or death. While foam materials are good for cushioning and protecting structures, shielding biological tissues from blunt force trauma poses a challenge [54]. The energy-absorbing efficiency of current foam materials for biotissue protection is

limited to around 0.5 J/g to 20 J/g [55] due to working pressure constraints, which is insufficient for effective protection from blunt force trauma.

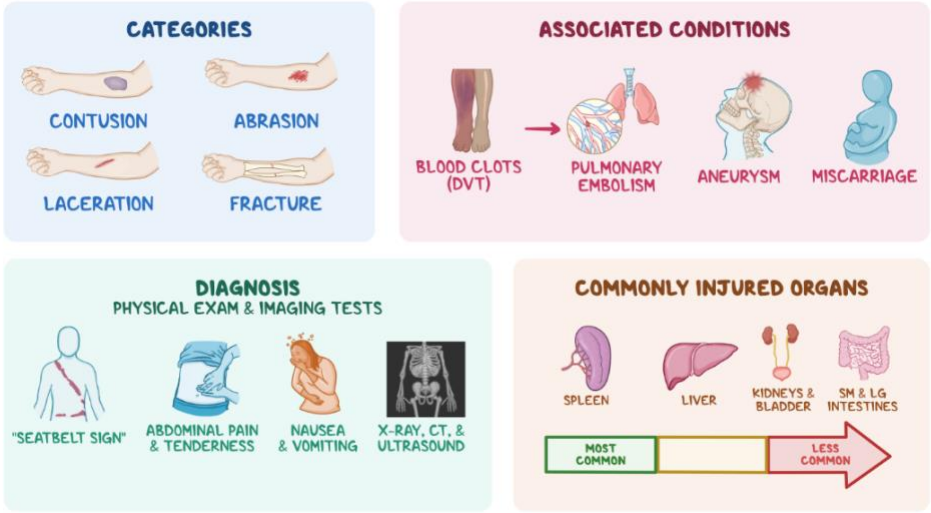

Figure 1-6: Blunt force trauma.

The same challenge exists for current armor materials. The main functioning of the armor (Fig. 1-7c) is to protect the body from casualties and damages caused by ballistic impacts, stabbing, fragmentation, etc. [56]. With recent efforts, today's armors are stronger, but also lighter and more flexible [57]. For example, Shear Thickening Fluid (STF), woven fibers and Epoxy have been used to combine with the Kevlar fabrics to fabricate lightweight and flexible body armors [58]. These strong armors can fully stop high-velocity projectiles, but lack of energy dissipation capabilities [59]. Only a small amount of the impact energy can be dissipated by the composite material, which leaves solders a great possibility to get traumatic injuries after the impact (Fig. 1-7b).

Airbags are a type of soft, but efficient energy absorber based on fluid (Fig. 1-7c). They lower the risk of hitting head and body against hard surfaces, being ejected from the vehicle, or suffering severe injuries due to glass and debris. However, they do not come without risk and can often lead to their own kinds of injuries. Damage to the soft tissue is still common, as face, chest, neck, and

back are vulnerable to directly contact with the highly pressurized airbags during car crash. In addition, the thickness of the airbag is not feasible for most of the wearable protective devices.

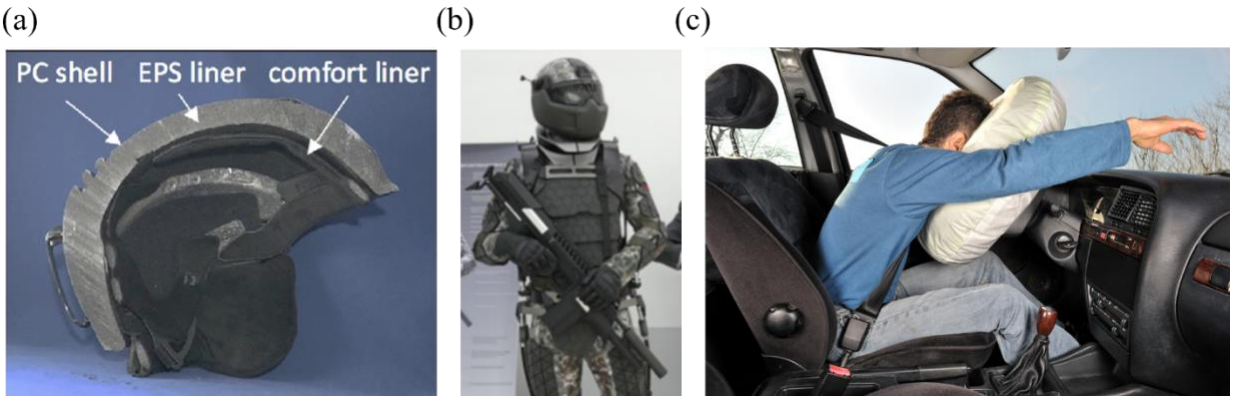

Figure 1-7: (a) Cross-sectional area of typical helmet, (b) Bullet-proof armor (copyright: daily mail), (c) Airbag.

1.3 Research Objective

The above challenges are common for most of the solid-based energy absorption materials and structures. New mechanisms and material systems having higher energy absorption efficiency, defect suppression and the ability to protect soft tissues are desired. To this end, we have developed liquid suspensions of glass bubble (GB) or nanoporous particles as new types of fluid-based energy absorbers. Their energy absorption performance under various loading conditions have been systematically investigated. The research objectives of the thesis are:

- To understand the different deformation mechanisms of the dry and wet GBs, to quantify the interaction between the liquid suspension of GB and the thin-walled tubes, and to demonstrate the extraordinary energy absorption performance of the liquid-based energy absorber.
- To demonstrate that the compressible fluid system, i.e., liquid nanofoam (LN) can transform regular thin-walled structures into dent-inert energy absorbers.
- To evaluate the effectiveness of protection of the compressible fluids on soft tissues.

Chapter 2 Background

2.1 Thin-Walled Tubes

The common use of thin-walled tubes components as energy absorbing devices is due to many important aspects including superior performance under dynamic loading, cost-effective, high efficiency, and ease of manufacturing and installation [60]. The energy absorption mechanism of thin-walled tubes is based on progressive plastic deformation under axial loading due to the ductility nature of the metallic materials [61–66]. There are three collapse modes of the thin-walled tubes – axisymmetric, non-symmetric mode and mixed deformation mode (Fig. 2-1a). The critical structural parameters of the thin-walled structures are the wall thickness to diameter and the length to diameter ratios.

Despite the lightweight and low-cost features, their energy absorption performance has been limited by the high initial peak force and low energy absorption efficiency during the crushing process (Fig. 2-1b). To address these challenges and improve the energy absorption efficiency of the post-buckling as well as the crushing stability of thin-walled structures, novel hybrid structures have been developed by altering the tube topologies [67–69] or filling the thin-walled tubes with foams [70,71] , lattice [72,73], and honeycombs [74,75]. However, the post-buckling performance of polymer foams filler contributes zero effect on the thin-walled tubes indicated in Fig. 2-2a. The Al foam filler enhances the post-buckling performance of the thin-walled tubes. However, the Al foam filler detaches from the tube wall when the local stress reaches a critical value, due to the stiffness mismatch between the filler and the tube wall as well as the stress concentration effect generated by the interfacial imperfections (Fig. 2-2b).

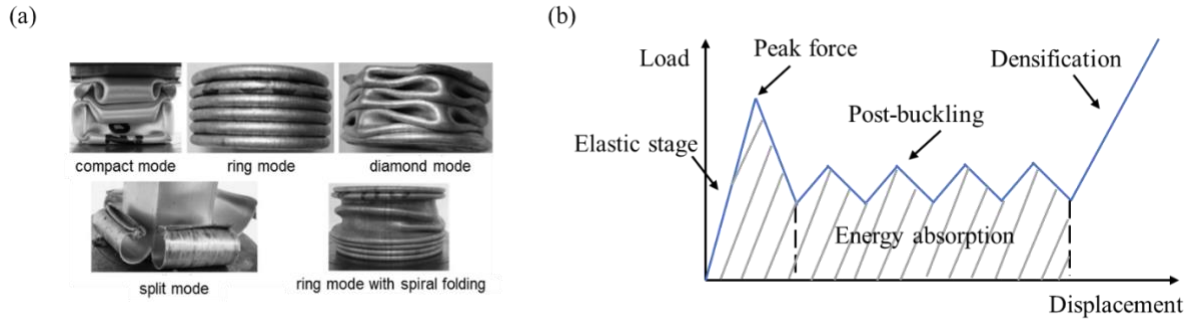

Figure 2-1: (a) Various buckling modes of thin-walled tubes. (b) Typical mechanism axial compression of thin-walled tubes.

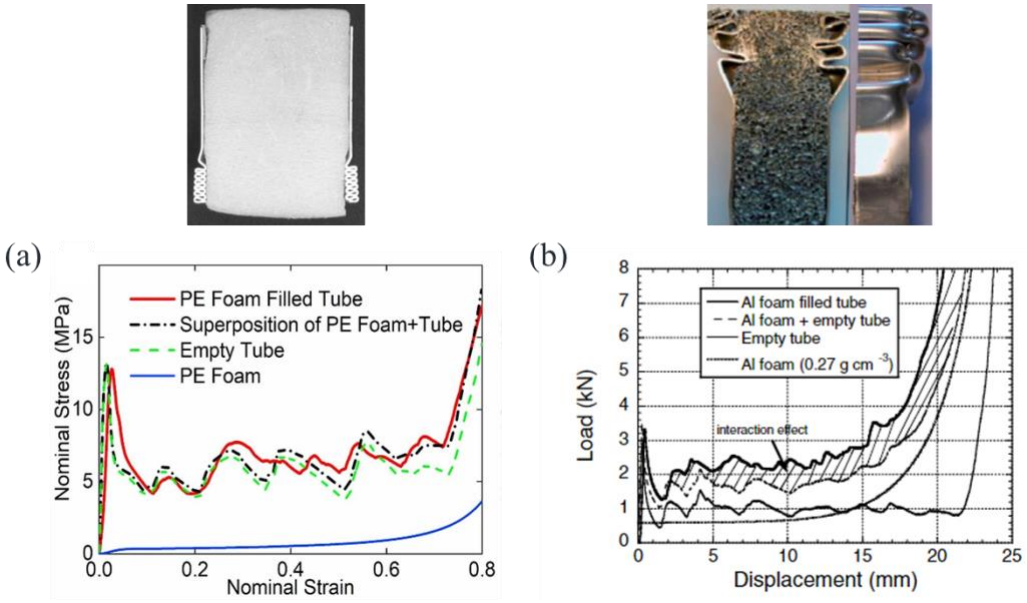

Figure 2-2: (a) Post-buckling performance of polymer foam filler thin-walled tube, (b) Post-buckling performance of Al foam filler thin-walled tube.

2.2 Liquid Nanofoam (LN)

The LN system is composed of the nanoporous particles and the non-wettable liquid phase (Fig. 2-3). Typical matrix material for the nanoporous particles includes silica, carbon, zeolites, celytes, metals, polymers. The typical size of the particles is in the range of 1-100 μm and the specific surface area is in the range of 100 m^2/g ~ 2000 m^2/g. The nanoporous particles can be classified into three categories based on the nanopore size as (1) microporous (< 2 nm), mesoporous (2-50 nm), and macroporous (> 50 nm).

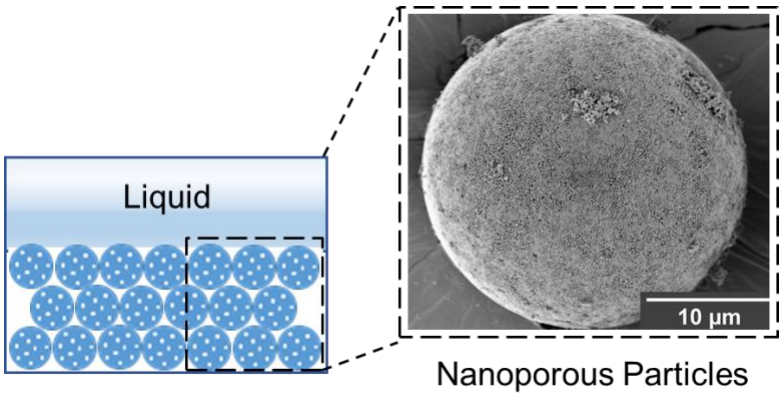

Figure 2-3: Schematic of the LN system and typical SEM image of the nanoporous silica microparticles.

Most nanoporous particles are hydrophilic, and thus absorb the liquid spontaneously when mixing with the liquid and no energy can be dissipated (Fig. 2-4a). In order to make the inner surface hydrophobic, the particles have to be processed by specific surface treatment. After the surface treatment, the nanopore surface is covered by a layer of hydrophobic alkyl chain (Fig. 2-4b). The chemical reaction during the surface treatment is described by the following equation:

$$SiO_2 - OH + R - Si(CH_3)_2 - Cl \longrightarrow SiO_2 - O - Si(CH_3)_2 - CH_3 + HCl \qquad (2-1)$$

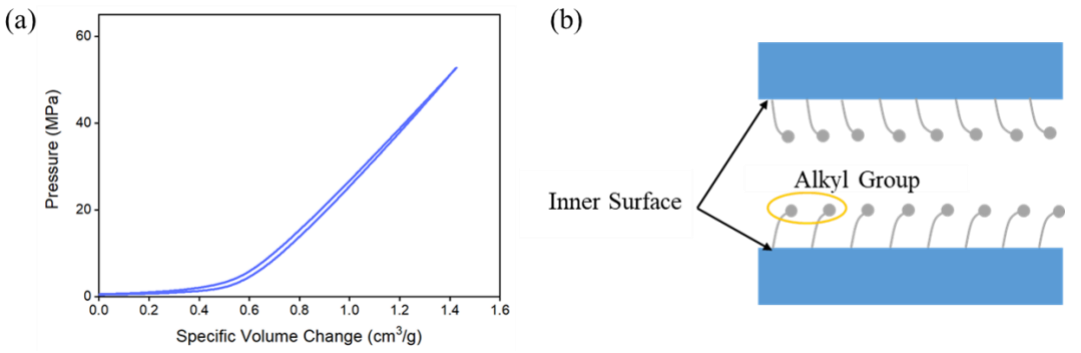

Figure 2-4: (a) Typical compressive behavior of LN containing nanoporous silica without surface treatment. (b) Schematic of surface modification.

The detailed surface treatment procedure is described as follows (Fig. 2-5). About 0.5 g of raw silica nanoporous particles are firstly vacuum dried at 100 °C for 2 h to remove moisture. Then, the particles are immediately immersed in 40 mL dry toluene, which is stirred at 90 °C for 3 hours for well mixing. After cooling to room temperature, 10 mL of surface reagent and 1 mL of pyridine as catalyst are added into the mixture, which is stirred and refluxed at 95 °C in a heating mantle for 5 hours. The surface treated nanoporous particles are washed with dry ethanol and dried in vacuum at 70 °C for two days.

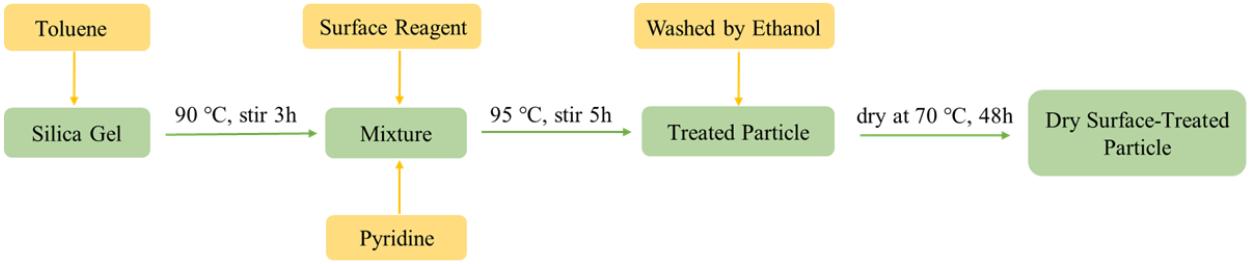

Figure 2-5: Typical surface treatment procedure.

To evaluate the energy absorption performance of the LN, an SS316 testing cell is adopted to seal the LN samples as sketched in Fig. 2-6. The LN is sandwiched by two pistons in a cylindrical sleeve. The sealing is accomplished by the O-ring fixed on each piston. An external force (F) is

applied on the testing cell and the corresponding hydrostatic pressure (P) applied on the sealed LN system is calculated as $P = F/A$.

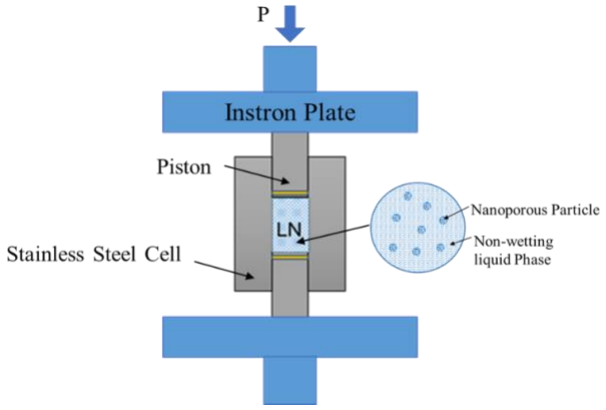

Figure 2-6: Schematic of LN specimen sealed in a testing cell with two pistons.

The energy absorption mechanism of the LN is illustrated in Fig. 2-7a. As the inner surface of the treated particles is hydrophobic, the liquid cannot enter the nanopores spontaneously under ambient conditions. Once the compressive pressure reaches a critical value, namely the infiltration pressure, the capillary effect is overcome, and the liquid molecules are driven into the nanopore. As the nanopore surface is exposed to the liquid, a solid-liquid interface with large area is formed and large amount of energy is dissipated as the interfacial energy[76,77] (Fig. 2-7b).

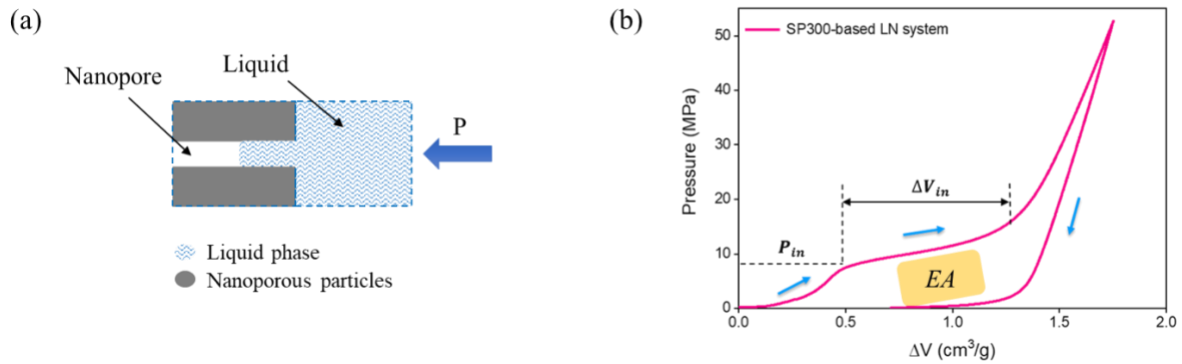

Figure 2-7: (a) Schematic of the liquid infiltration mechanism in a nanopore. (b) Typical compressive behavior of LN containing nanoporous silica with surface treatment.

The liquid infiltration pressure is governed by the Young-Laplace equation,

$$P_{in} = \frac{2\gamma \cdot cos\ \theta}{r} \qquad (2-2)$$

Where γ is defined as the effective solid-liquid interfacial tension, θ is defined as the contact angle between the liquid and nanopore surface, and r is the effective nanopore radius. Thus, P_{in} can be controlled by adjusting the parameters in equation 2-2.

2.3 Advantages of Liquid Nanofoam

The liquid nanofoam has a number of advantages,

High energy absorption efficiency. Because of the specific large surface area of the nanopore, the LN system has higher energy absorption capacity compared with the traditional energy absorption materials.

Light weight and soft. The materials are light weight and soft, which can protect soft tissue from getting injured by mitigating huge amount of energy induced by the impact.

Ultra-fast response and energy mitigation rate. The liquid infiltration activation takes less than millisecond, making LN a promising energy absorber in high strain rate impact [78].

Tunability and fluidity. The LN system can be shaped and filled into customized structures due to the fluidity property [79].

Stable performance under a wide temperature range. The LN system can sustain performance under extreme weather conditions, which makes it a potential material for the building, automobile, and aerospace fields.

Higher strengthening coefficient and strong interacting bonding. The interaction between the LN filler and tube is much stronger than solid foam-tube wall interaction which can enhance the post-buckling performance compared to the traditional materials [80].

2.4 Hollow Glass Microsphere

Hollow glass microsphere (HGM), also known as glass bubbles, is made of soda-lime borosilicate glass, are finely dispersed and free-flowing powders consisting of thin-walled (0.3-1.5 μm) hollow glass microspheres (Fig. 2-8). They have a high strength-to-density ratio (density: 0.12-0.60 g/cm^3), so they are both ultra-light weight and strong enough to survive processing. The size of the particles is in the range of 15-135 μm with the pore surfaces of 1.9 m^2/g-2.7 m^2/g. Due to the variety of the pore size, the crush strength is in a wider range of 1-185 MPa.

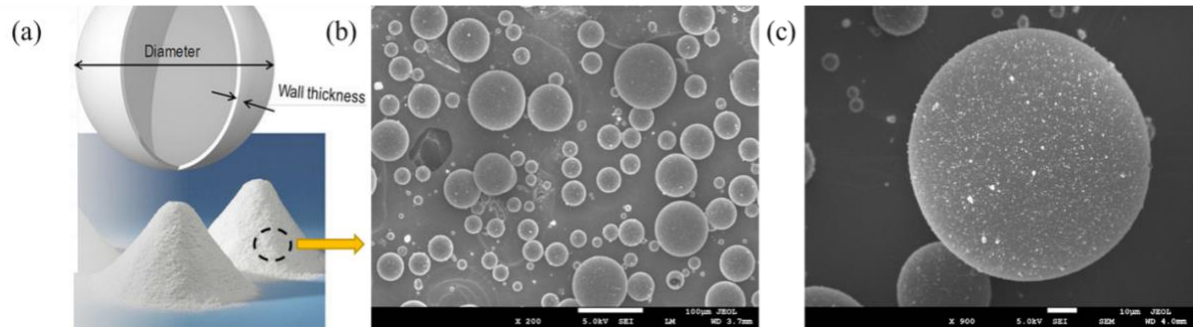

Figure 2-8: (a) Glass Bubble property (copyright: 3M Glass Bubble), (b) and (c) Typical SEM image of the glass bubble.

The properties of chemically inert and nonporous surface offer the glass bubbles the opportunity of a variety of advantages over irregularly-shaped additives or fillers. They render polymers with improved mechanical [81,82], electrical [83], thermal [84–86] and dimensional properties. The advantages of glass bubbles as a type of composite reinforcement are summarized below.

Weight reduction. Glass bubbles are used to reduce weight in applications from plastics, thermosets and sheet- or bulk-molded composites to structural foams and elastomers. All without requiring significant material or process changes, and without compromising the mechanical integrity of the finished product.

Dimensional stability. Glass bubbles can reduce shrinkage and warpage in plastics, spackling compounds, wood composites and other materials, which helps to reduce rejections and

reprocessing. They allow high filler loading, which can improve part stiffness and dimensional stability, helping prevent sink marks and uneven solidification.

Thermal insulation. The addition of glass bubbles to a resin system can decrease thermal conductivity. The low thermal conductivity of glass bubbles makes them ideal for use in thermally insulating syntactic foams for deep sea applications.

To better understand the deformation mechanism of glass bubble, the mechanical response of HGM was characterized by a series of quasi-static compression under the Intron tester with the same 2 mm/min loading speed (Fig. 2-9a). The loading curve can be divided into three regions: 1-linear, 2-stress plateau and 3-densification as indicated in Fig. 2-9b. The schematic of deformation mechanism of HGM in three regions can be referred to Fig. 2-10 accordingly. In region 1, an inhomogeneous force chain network is gradually building up in the dry HGM granular media [87]. Once the critical fracture strength in the force chain network is reached, larger HGM collapse first due to the particle size distribution, followed by the fracture of smaller ones. This critical fracture strength is related to the geometrical parameters of the HGM, such as the microsphere diameter and wall thickness [88]. Therefore, the stress plateau with a positive slope is formed in region 2. Once glass bubbles are crushed, the system reaches densification after the end of the plateau (region 3). Upon unloading, the stress drops abruptly to zero and the system shows a hysteric behavior. The energy absorption can be calculated by the area enclosed by loading and unloading curve.

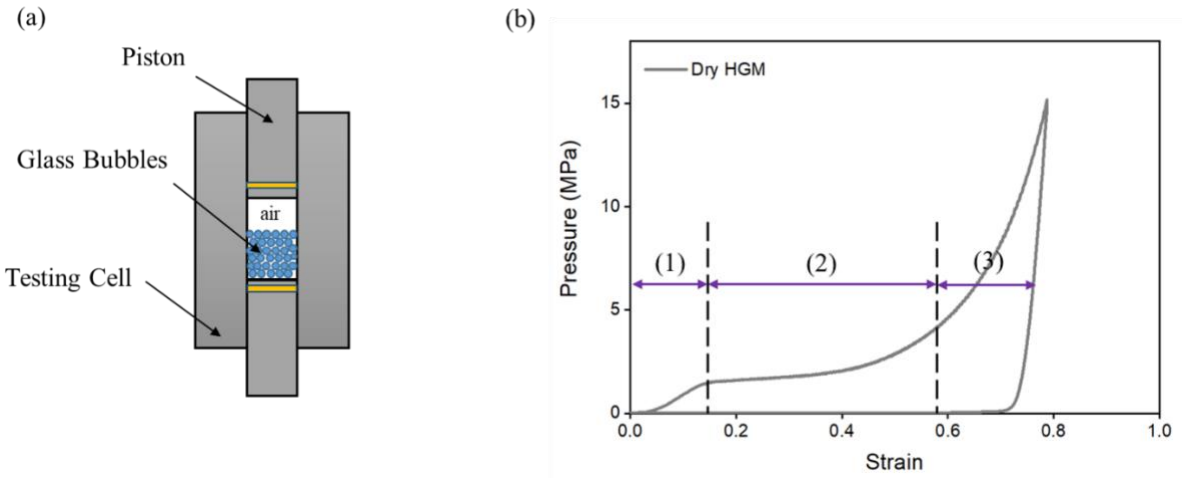

Figure 2-9: (a) Schematic of glass bubble particles sealed in a testing cell with two pistons, (b) Typical quasi-static compression of dry glass bubbles.

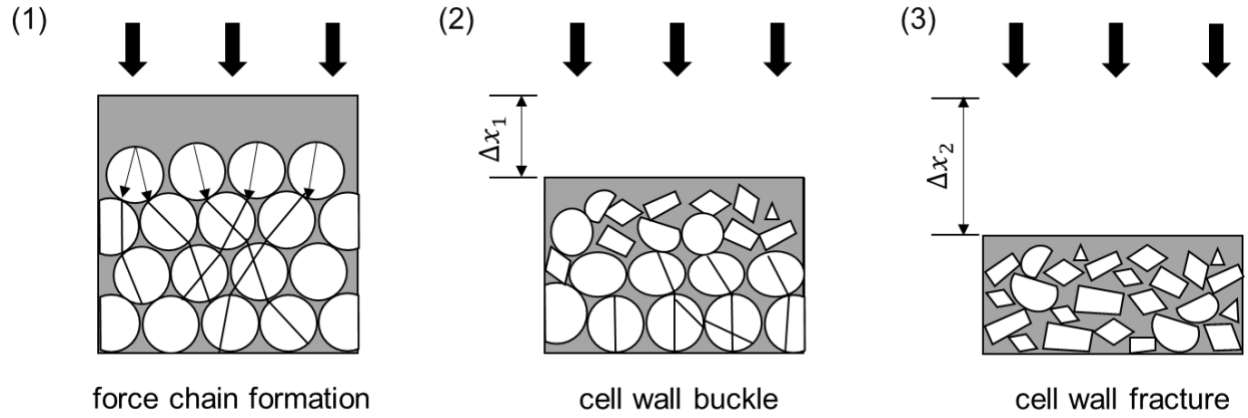

Figure 2-10: Schematic mechanism of HGM under quasi-static compression.

The new configuration of glass bubbles suspended in water (SHGM) overlooked before is studied in this work. When mixed with water, glass bubbles will be suspended in water and stay in a uniform hydrostatic status (Fig. 2-11).

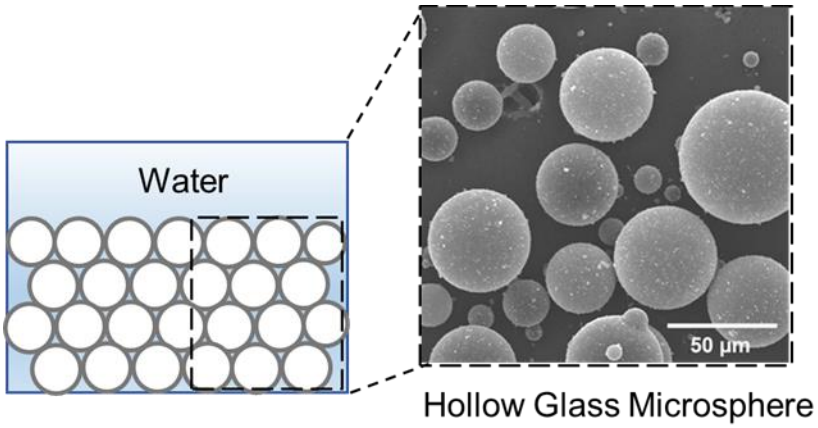

Figure 2-11: Glass Bubbles suspend in water.

To study the deformation mechanism of SHGM, the quasi-static compression test is conducted. The loading curve is divided into three regions similar to the HGM but with much higher stress values as 4-linear, 5-stress plateau and 6-densification (Fig. 2-12). The schematic of deformation mechanism of HGM in three regions are referred to in Fig. 2-13 accordingly. In region 4, the linear pressure increases, no force chain network is formed because the presence of excess water minimizes the contact force between adjacent microspheres. Instead, a hydrostatic pressure builds \up in the SHGM, which is similar to that in soil consolidation [89]. This is confirmed by the higher range of the elastic behavior. At the end of the elastic region, a turning point with a much-reduced slope is observed in region 5. This is due to the collapse of the microspheres under hydrostatic loading condition. With the larger size of glass bubbles damaging first, liquid gets into the hollow core of glass bubbles, followed by smaller size of glass bubbles. Once all glass bubbles are crushed and filled with liquid, the systems become incompressible, leading the stress to go up steeply in region 6.

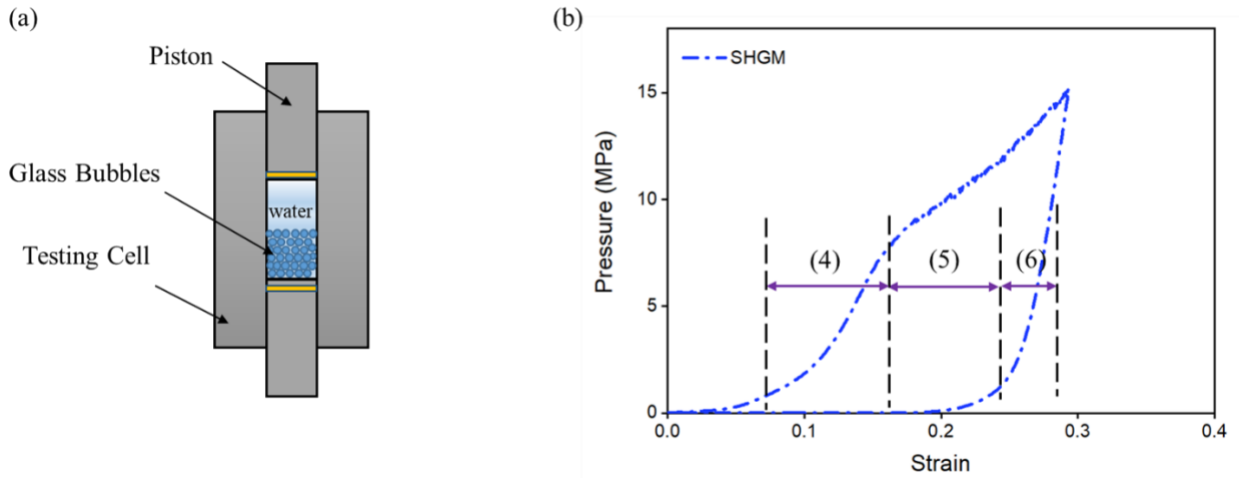

Figure 2-12: (a) Schematic of SHGM sealed in a testing cell with two pistons, (b) Typical quasi-static compression of SHGM.

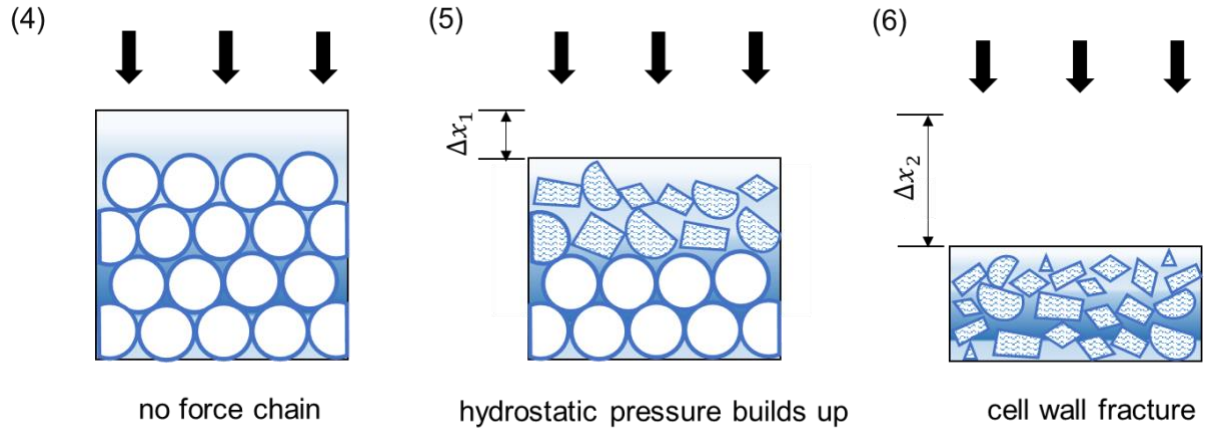

Figure 2-13: Schematic of mechanism of SHGM under quasi-static compression.

The deformation mechanism comparison of HGM system and SHGM system is shown in Fig. 2-14. The HGM system is highly deformable due to the hollow core inside of glass bubble and the air gaps between the GMs. The SHGM system is less deformable as the air gaps between the GMs are filled by water. However, the energy absorption capacity of both systems is close, because the hydrostatic pressure built up in the SHGM brings up the working pressure of the system.

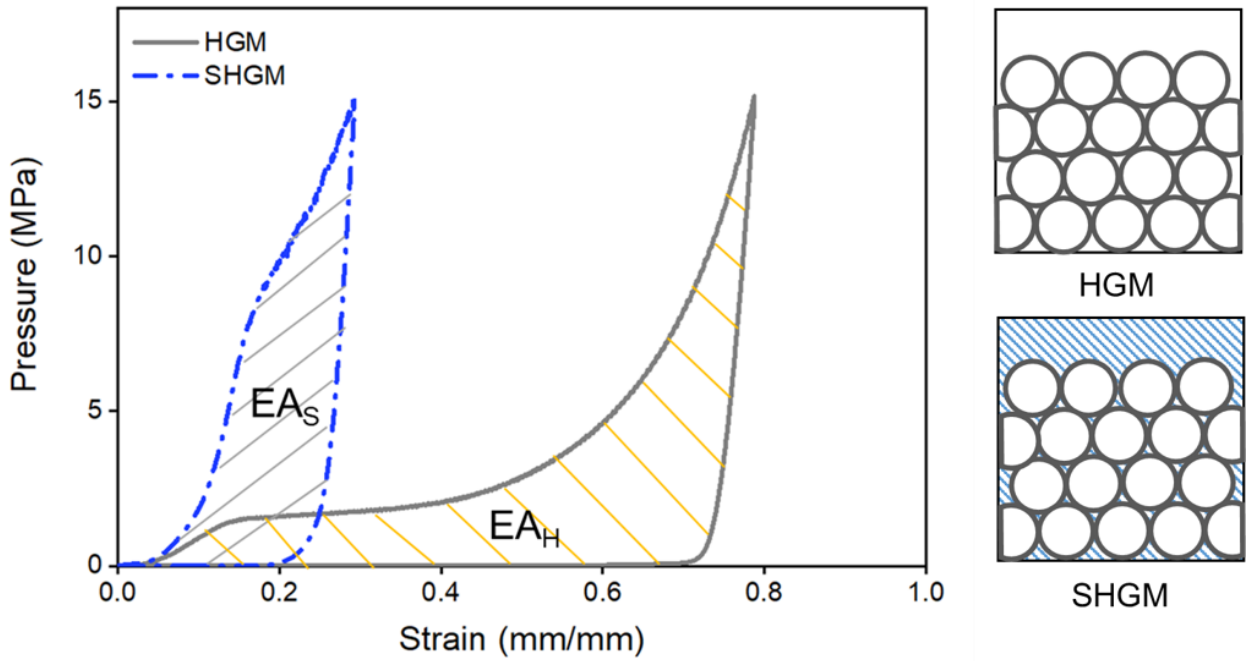

Figure 2-14: Typical quasi-static mechanical response of the SHGM and HGM.

2.5 Summary

This Chapter introduced the basic mechanism of the emergency advanced energy absorption material and thin-walled tube, which lays the foundation for the future study in Chapter 3-5. Chapter 3 will discuss the energy absorption performance of SHGM as a filler material in the thin-walled tubes comparing with the HGM filler. Chapter 4 will demonstrate the energy absorption performance of LN, as a filler in thin-walled tubes with imperfection. Chapter 5 will investigate whether the LN system is effective to protect soft tissues under mechanical abuse.

Chapter 3 Interaction between SHGM and Thin-Walled Tubes

This chapter introduces hollow glass microsphere (SHGM) used as a filling material of thin-walled tubes to tackle the challenge of deviation between the high initial peak force and low mean crushing force of thin-walled tubes that significantly limited its energy absorption efficiency. The axial crushing behavior of SHGM-filled tubes is evaluated by a series of quasi-static compression tests as well as dynamic drop weight impact tests. The filler-tube wall interaction effect contributes to the overall performance through the load transfer effect and inward buckling suppression effect is studied in this chapter. 3D digital image correlation technique is introduced to directly observe the tube wall deformation during the energy absorption process. These results demonstrate the SHGM is a superior filling material for thin-walled structures and the findings from this study can facilitate the design of next generation lightweight composite structures for energy absorption purposes. The material presented in this chapter was published in *Composite Structures*.

3.1 Introduction

Thin-walled structures have been widely used as energy absorbing components to prevent personnel injuries and facility damages in automotive, aerospace, and aviation industries [90–92]. Despite the lightweight and low-cost features, their energy absorption performance has been limited by the high initial peak force and low energy absorption efficiency during the crushing process. To address these challenges, metallic foams have been commonly used as the filling materials to promote the post-buckling force as well as the crushing stability of thin-walled structures [93,94]. A number of strategies such as graded foam filling [95,96], bionic structure [97,98], topology optimization [99,100], multi-cell structure [101,102], tube-reinforced foam [103,104] have also been developed to further improve the energy absorption performance of thin-walled structures.

Regarding the underlying reinforcing mechanism of foam-filling method, researchers have found that the overall performance of the composite tube is composed of three parts: the axial buckling of the tube wall, the deformation of the foam, and their interaction effect [105,106]. Santosa et al. demonstrated that the effect of filler-tube wall interaction contributes as much as 80% of the foam filler, leading to a strengthening coefficient of 1.8 for the foam filler [107]. Thus, tailoring this filler-tube wall interaction through strengthening the bonding at the interface is a promising approach to further improve the crushing response of the composite tube. By applying a layer of adhesive, the contribution from the filler-tube wall interaction effect increases to 180% of the foam filler [108–110]. However, the epoxy curing process is time-consuming and not cost-effective. What's worse, structural defects like molten metal drainage, pore coalescence and foam shrinkage [111] are inevitably introduced during the foaming process. These defects lead to the filler-tube wall debonding during tube crushing and finally weaken the interaction effect as well as the overall performance of the composite tube.

Recently, compressible liquid fillers have shown great potential in strengthening the interfacial bonding as well as the resulted energy absorption of the thin-walled structures [112,113]. Due to its intrinsic flexibility, the liquid filler forms seamless contact with the tube wall, resulting in a much stronger "bonding" between the liquid filler and tube wall. However, liquid fillers with high deformability for thin-walled tubes are still scarce and more effective and efficient liquid filling material are desired to satisfy the growing demand for vehicle crashworthiness applications.

Hollow glass microsphere (HGM), also known as glass bubble, is a type of hollow spherical inorganic powder. Despite these recent progresses of HGM-enabled applications, its liquid counterparts, namely liquid suspension of hollow glass microsphere (SHGM), has long been

ignored. In this work, we propose to use SHGM as the filling material for thin-walled tubes. To this end, SHGM-filled steel tubes have been prepared and the crushing responses under both quasi-static compression and dynamic drop weight impact have been evaluated. The underlying reinforcing mechanisms have also been investigated and the enhanced filler-tube wall interaction induced plastic deformation of the tube wall has been visualized.

Advantages of Glass Bubble Functionalized Liquids

In conclusion, glass bubble functionalized liquids have a number of advantages,

Ultralight weight and higher energy absorption capacity. The volume of the GB system can be minimized due to the lower density (0.12-0.60 g/cm3). When mixing with sufficient water, the energy absorption capacity reaches its highest value.

Tunability and fluidity. Similar to the LN system, the GB system can be shaped and filled into any structure according to the project's needs.

Eliminating the weak network of force chain in the dry glass bubble and enhanced the stress performance during compression.

3.2 Materials and Methods

3.2.1 Specimen Preparation

Commercial seamless thin-walled tubes made of the 304 stainless steel (Product No. 304F10500X006SL, MicroGroup Inc.) were used in current study. The outer diameter and wall thickness of the circular tube were D = 12.7 mm and t = 0.15 mm, respectively. The steel tubes were filled with two different fillers, i.e., SHGM and dry HGM, as shown in Fig. 3-1. The SHGM-filled tube was prepared by sealing a water suspension of HGM in the thin-walled tube with two metallic endcaps using an epoxy glue (Part No. 50112, J-B Weld Company). The mass of HGM and water were 0.6 g and 0.9 g, respectively. The effective height (h) of the tube was 20.3 mm. No

water leakage from the sealing region was observed in all following tests. The HGM-filled (Fig. 3-1 c) tube was prepared in a similar procedure, and empty tubes (Fig. 3-1d) with same end capping were used as reference. For each type of tube, at least three samples were prepared and evaluated.

The HGM employed in this study was a soda-lime-borosilicate glass bubble material (Grade No. K37. 3M Company). The HGM was received in powder form with the average particle size of 45 μm. Fig. 3-1e shows the microstructure of the HGM particles. The SHGM was prepared by mixing HGM and pure water in a gravimetric ratio of 40:60.

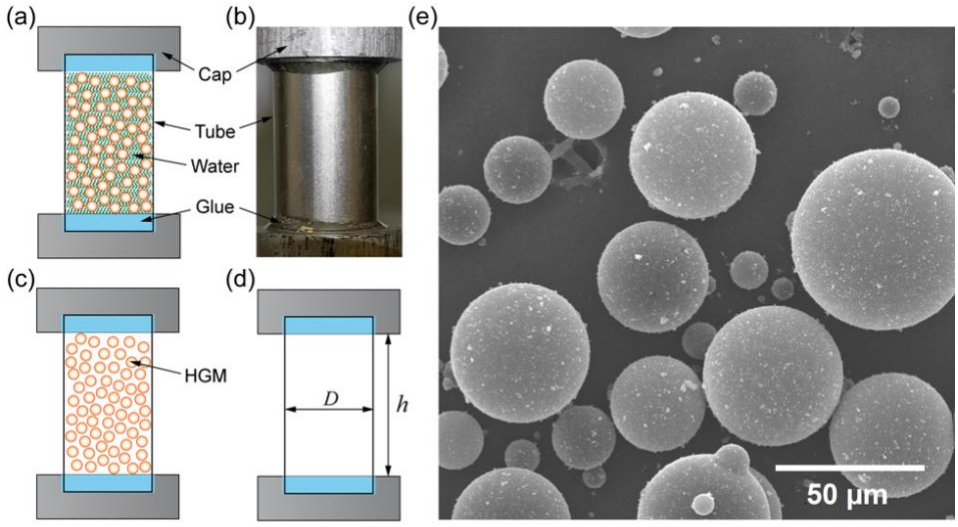

Figure 3-1: (a) Cut view of the SHGM-filled tube (b) A typical SHGM-filled tube specimen (c) Cut view of the HGM-filled tube (d) Cut view of the empty tube (e) Scanning electron microscope (SEM) images of the HGM particles.

3.2.2 Test Procedures

The compressive material properties of the filling materials, including the SHGM and HGM, were characterized first by quasi-static compression tests using a universal tester (Model No. 5982, Instron Corporation). The filling material sandwiched by two metallic pistons in a cylindrical testing cell (Fig. 3-2a) was compressed at a constant loading speed of 2 mm/min. The nominal stress was calculated as $f = F_p/A_p$, where F_p was the load applied on the piston by the Instron machine and A_p = 126 mm^2 was the cross-sectional area of the piston. The nominal strain was

calculated as $\varepsilon_f = \delta/d$ where δ was the displacement of the Instron crosshead and d was the thickness of the filling material in the testing cell.

The mechanical response of all types of thin-walled tubes were characterized by a series of quasi-static compression tests under the Intron tester with the same 2 mm/min loading speed, as shown in Fig. 3-2b. The nominal stress was calculated as $\sigma = F/A$, where F was the force applied on the tube and A was the cross-sectional area of the tube. The nominal strain was calculated as $\varepsilon = \delta/h$.

The dynamic response of the steel tubes was characterized by a customized drop weight impact apparatus (Fig. 3-2c). The drop weight, m_w, was 10 kg. The incident speed was kept at 3.0 m/s by controlling the free-falling height of the drop weight. The deceleration time history was measured by an accelerometer (Model No. 353B03, PCB Group, Inc.) and recorded by a high-speed digitizer (Model No. NI-9215, National Instruments Corp.) at the sampling rate of 10^5 samples/s. The incident speed was confirmed by $v = \int a(\tau)d\tau$, where $a(\tau)$ was the measured deceleration of the drop weight at time. The displacement was calculated as $\delta = \iint a(\tau)\, d^2\tau$. The nominal stress was determined as $\sigma = m_w \cdot \alpha(\tau)/A$.

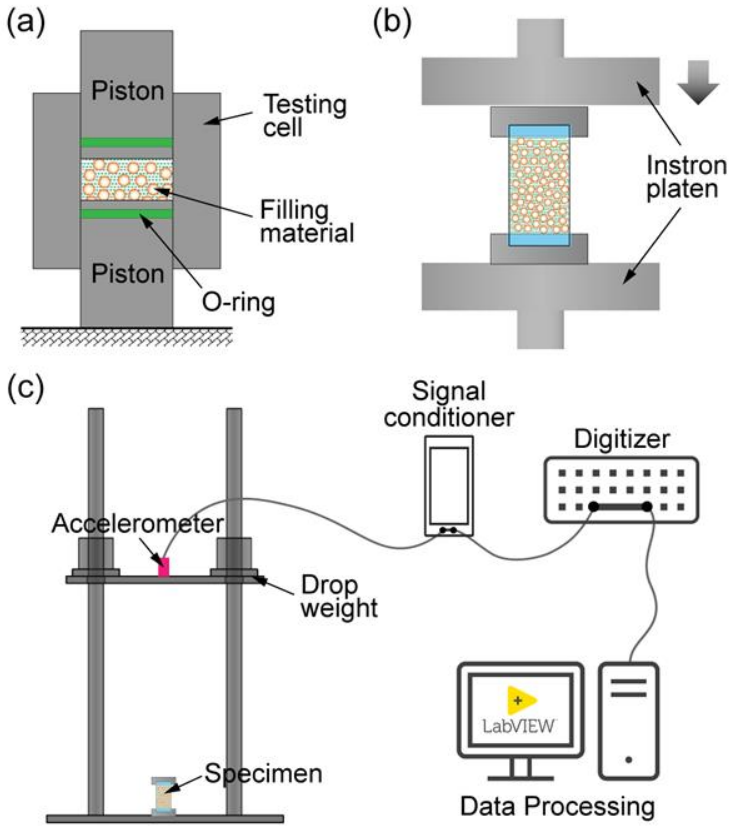

Figure 3-2: Schematic of the characterization of (a) mechanical properties of the filling material (b) quasi-static mechanical response of the tubes (c) dynamic behavior of the tubes.

3.2.3. Crashworthiness Indicators

To assess the energy absorption performance of the thin-walled tubes, a number of crashworthiness indicators are determined during the deformation process. The energy absorption capacity of the tube, EA, is calculated by integrating the load vs displacement curve,

$$EA = \int F \cdot \mathrm{d}\delta \qquad (3-1)$$

The specific energy absorption (SEA), considering of the mass of the composite structure, is one of the most important properties in the design of light-weight structures and can be calculated as

$$SEA = \frac{EA}{m} \qquad (3-2)$$

Where *m* is the total mass of the energy absorber. To evaluate the uniformity and stability of the force response of the steel tube, energy absorption efficiency η [114], also known as the crush force efficiency *CFE* [115], is usually adopted. It can be determined from the energy absorption ratio of actual energy absorber to the ideal energy absorber,

$$\eta = \frac{\int \sigma d\varepsilon}{\sigma_{max}\varepsilon} \qquad (3-3)$$

Where max is the peak stress over the calculated strain range. η is expected to be one for an ideal energy absorber.

3.3 Results and Discussion

3.3.1. Quasi-Static Compressive Behavior of Filling Materials

Two different materials including SHGM and HGM are selected as the filler for the steel tubes in this study. Typical stress-strain curves of these filling materials under quasi-static compression condition are shown in Fig. 3-3a. As the dry HGM is compressed in the testing cell, the system stress increases linearly with the increasing volumetric strain initially. During this process, an inhomogeneous force chain network [116] is gradually building up in the dry HGM granular media. At f = 0.06, the critical fracture strength of the load-carrying microspheres in the force chain network is reached, and a wide stress plateau (with stress ranging from 1.1 MPa to 6 MPa) associated with the collapse of the microspheres is observed. This critical fracture strength is related to the geometrical parameters of the HGM, such as the microsphere diameter and wall thickness [117]. Due to the particle size distribution of the HGM material used in this study, larger microspheres collapse first, followed by the fracture of smaller ones; thus, the stress plateau shows a positive slope. As the strain reaches 0.6, the HGM reaches the densification stage, and the stress goes up quickly. Upon unloading, the stress drops abruptly to zero and the system shows a remarkably hysteric behavior. This hysteresis indicates the HGM undergoes permanent

deformation during the loading process, which can be further validated by the zero deformability in the 2nd loading-unloading cycle. Fig. 3-3b shows the HGM after dry compression and it is confirmed that nearly all microspheres are crushed except those with diameters smaller than 10 μm.

As the SHGM is compressed in the testing cell, no force chain network is formed because the presence of excess water minimizes the contact force between adjacent microspheres, which is similar to that in soil consolidation [118]. Instead, hydrostatic pressure builds up in the SHGM and it shows an elastic behavior which is the combination performance of the HGM and water molecules. As the system pressure reaches about 8 MPa at $\varepsilon_f = 0.07$, a turning point as characterized by a much-reduced slope is observed. This is due to the collapse of the microspheres under hydrostatic loading condition. Distinct from the dry compression of HGM, the isostatic loading in SHGM eliminates the force chain-induced stress concentration effect and results from a much-increased stress level in the plateau region. As the quasi-static compression progresses, the HGM suspending in the water continually, leading to a considerable volume change of the material. As the system reaches the peak pressure 32 MPa, the Instron platen is moved back, and the pressure drops abruptly. When the SHGM is compressed again, it shows nearly zero deformability, revealing that the suspending HGM is crushed in the 1st loading process. After quasi-static compression, the deformed HGM suspending in water is collected and dried for the characterization of its microstructure using SEM. As shown in Fig. 3-3c, the HGM with diameter larger than 20 μm are completely fractured.

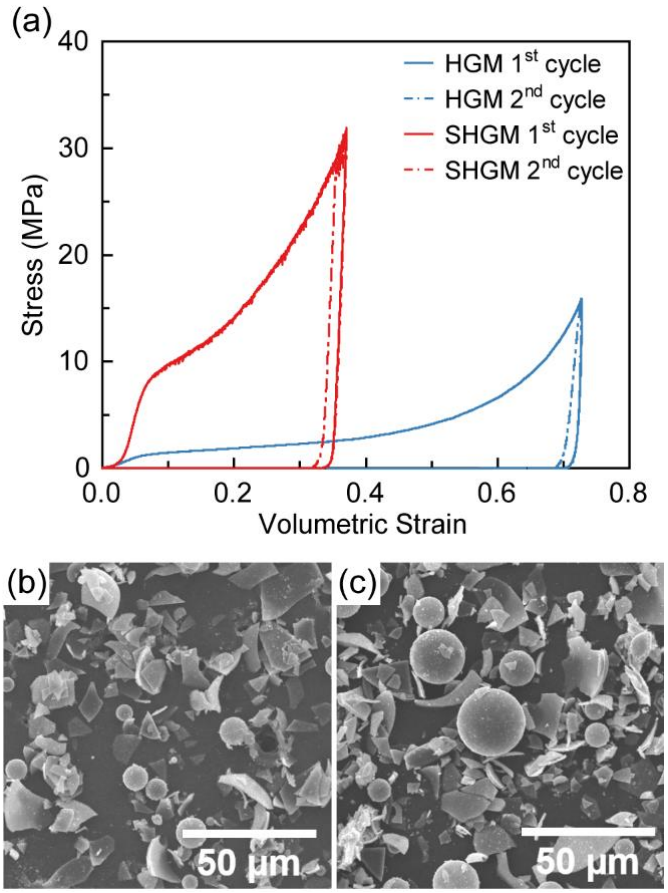

Figure 3-3: (a) Typical quasi-static mechanical response of the filling materials, including SHGM and HGM (b) SEM images of the HGM after quasi-static compression (c) SEM images of the microspheres after compressing SHGM.

3.3.2. Quasi-static Compressive Behavior of Tubes

The quasi-static mechanical response of empty, HGM-filled, and SHGM-filled tubes has been characterized by axial compression tests. Fig. 3-4a shows typical stress-strain curves of the steel tubes. Upon quasi-static compression, the empty tube first deforms in a linear elastic manner. As the stress reaches a critical value of 12.5 MPa, the tube wall starts to buckle, and the stress drops quickly to a lower level. As the compression progresses, a stress plateau corresponding to a relatively large tube wall deformation is formed. The fluctuation of this plateau is caused by the fold initiation, formation, and collapse on the tube wall. The buckling mode of the empty tube is shown in Fig. 3-4b. As the buckling is initiated, the tube wall continually folds, forming three

corners per lobe. At ε = 0.6, a total of four folds is observed, which agrees well with the undulations in the post-buckling stress plateau in Fig. 3-4a. Thus, the empty steel tube buckles inwards in a typical non-axisymmetric diamond mode [119,120].

As the tube is filled with HGM, the buckling initiation stress is promoted to 14 MPa due to the rigid filler. Compared to the empty tube, the stress level of the post-buckling plateau is increased to about 8 MPa. This is due to the reinforcement effect of the HGM filler. During this process, the HGM continually crushes along with the tube wall folding. Furthermore, since the mechanical response of HGM is smoothly rising (Fig. 3-3a), the amplitude of the fluctuations in the plateau is much reduced. The characteristics of the buckling mode of HGM-filled tube is quite similar to that of empty tube. No crack on the tube wall is observed, indicating the high-strength and ductility of the steel tube. Fig. 3-4c shows the microspheres are almost completely crushed during the quasi-static compression of HGM-filled tubes.

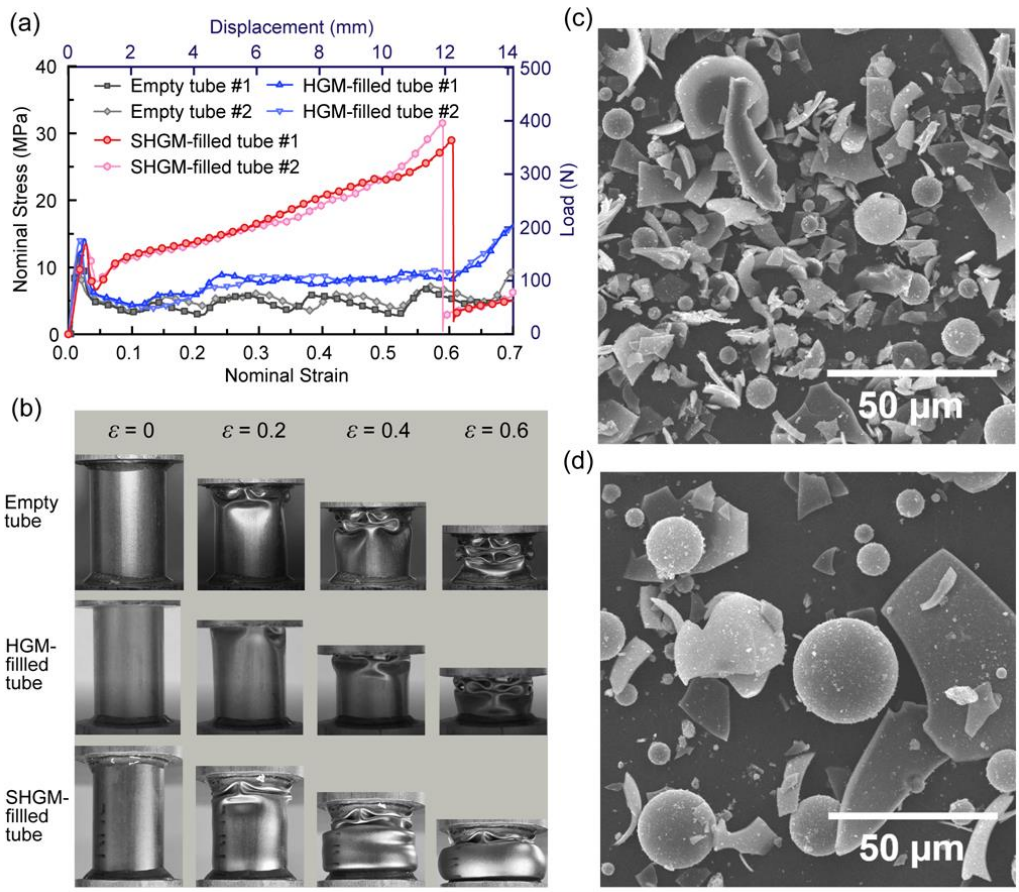

Figure 3-4: (a) Typical stress-strain curves of steel tubes under quasi-static compression. Stress-strain and load-displacement axes are inter-changeable. For each type of tube, curves of two samples are shown here for clarity. (b) Snapshots of the progressive deformation mode of empty tube, HGM-filled tube, and SHGM-filled tube under quasi-static compression. (c) SEM images of the microspheres in HGM-filled tube after quasi-static compression. (d) SEM images of the microspheres in SHGM-filled tube after quasi-static compression.

For SHGM-filled tube, the buckling initiation process is similar to that of HGM-filled tube. The tube buckles at 13.5 MPa, after which the stress drops to 6.7 MPa. This reduced stress level is due to the inevitably introduced air bubbles in between the microspheres and water. As a result, the tube wall forms a folding lobe at the top, as shown in Fig. 3-4b. As the strain reaches 0.05, the hydrostatic pressure starts to build up in the tube and rapidly rises to 11 MPa. Thereafter, a wide post-buckling plateau with much-enhanced stress level is formed, showing the high compressibility of the SHGM-filled tube. This plateau corresponds to the crushing of the HGM suspending in water. As shown in Fig. 3-4b, the buckling mode of the tube transforms from the

non-axisymmetric diamond mode to the axisymmetric concertina mode, finally leading to the bulging of the tube wall. As the stress increases to around 30 MPa at ε = 0.6, the inner hydrostatic pressure reaches the hoop stress of the tube wall, resulting in the burst of the whole composite structure. The liquid suspension flows out and the tube deforms like cracked empty tube. Consequently, the stress level after tube burst is slightly lower than that of pristine empty tube. Fig. 3-4d shows the microstructures of dried SHGM after tube compression and the HGM with diameter larger than 30 μm are completely fractured. Those remaining intact microspheres with diameter smaller than 30 μm indicates that the energy absorption capacity of SHGM has not been fully utilized.

Table 3-1: Comparison of empty, HGM-filled, and SHGM-filled tubes under quasi-static compression

E=0-0.6	Mass (g)	Height (mm)	EA (J)	SEA (J/g)
Empty tube	1.27 ± 0.03	20.3 ± 0.1	7.7 ± 0.3	6.1 ± 0.2
HGM-filled tube	1.92 ± 0.05	20.3 ± 0.1	11.3 ± 0.2	5.9 ± 0.1
SHGM-filled tube	2.87 ± 0.06	20.3 ± 0.1	25.1 ± 0.7	8.7 ± 0.3

The energy absorption performance of tubes under quasi-static compression is summarized in Table 3-1. The *SEA* of empty tube at strain of 0.6 is around 6.1 J/g. The HGM-filled tube exhibits a small decrease in *SEA* compared to that of empty tube, indicating that the dry HGM filler compromises the energy absorption performance of the resulted thin-walled structure. In contrast, the *SEA* of SHGM-filled tube is 8.7 J/g, showing a 43% increase compared with empty tube. This much-enhanced energy absorption behavior of the SHGM-filled tube is mainly due to the reinforced liquid-solid interaction between the liquid SHGM filler and the solid tube wall.

3.3.3 Filler-Tube Wall Interaction

Previous studies have demonstrated that the energy absorption capacity of foam-filled tubes consists of three contributing components, namely the buckling of the tube wall, the deformation of the filler, and the interaction effect between the filler and tube wall [114] [121]. To quantify the contribution of each component, the corresponding absorbed energy has been calculated. The *EA* of empty tube and filled tubes, as shown in Table 3-1, are determined from the integration of their load-displacement curves. Since not all the microspheres are crushed during the tests (Fig. 3-4c and 3-4d), the *EA* of the filling materials is determined from the difference between their energy absorption capacity before and after tube compression, as shown in Fig. 3-5a and 3-5b. For HGM-filled tube, the *EA* is equal to the sum of the HGM filler and empty tube (Fig. 3-5c), indicating that there is negligible contribution from the filler-tube wall interaction. By contrast, the *EA* of SHGM-filled tube is much larger than the sum of SHGM filler and empty tube, which must be attributed to the enhanced SHGM liquid filler-tube wall interaction.

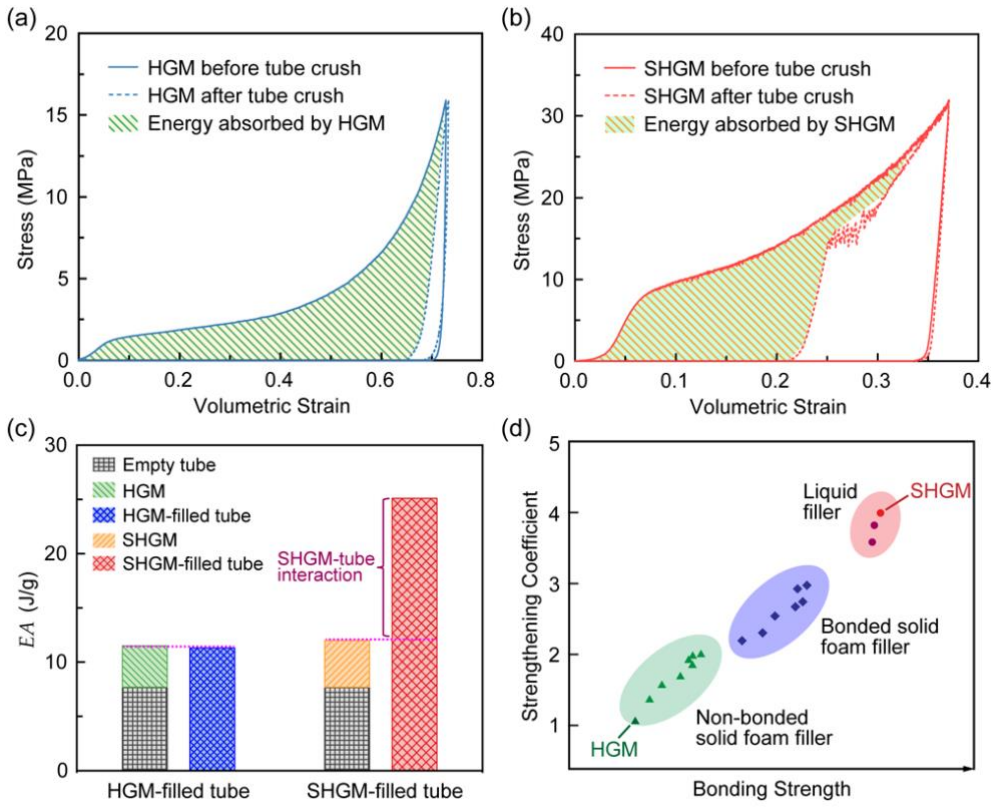

Figure 3-5: (a) Typical mechanical response of HGM filler before and after tube compression. (b) Typical mechanical response of SHGM filler before and after tube compression. (c) Energy absorbed by each component in HGM-filled and SHGM-filled tubes. (d) The strengthening coefficients in various foam-filled tubes, including SHGM-filled tube in this work, liquid nanofoam-filled tubes [114,122,123], bonded solid foam-filled tubes [124–130] and non-bonded solid foam-filled tubes [129,131–136].

To better understand the effect of SHGM-tube wall interaction on the energy absorption performance of the composite structure, it has been further quantified by the strengthening coefficient (denoted as C) of foam filling [137–139] which is defined as

$$E_{ft} = E_t + C \cdot E_f \qquad (3-4)$$

Where E_{ft}, E_t, and E_f are the energy absorbed by the composite tube, empty tube, and filling material, respectively. Fig. 3-5d summarizes the results of the strengthening coefficient of various foam-filled tubes. The average C of HGM-filled tube is around 1.0. This zero filler-interaction is consistent with its unaltered buckling mode compared with empty tube (Fig. 3-4b). The average C

of SHGM-filled tube is about 4.0, much higher than that of solid foam-filled tube, revealing that the filler-tube wall interaction is much enhanced. This enhancement is due to the intimate contact of the SHGM liquid filler and the rigid tube wall, leading to an ultra-high strength "liquid-solid bonding" between them. The filler-tube wall interaction increases with the bonding strength between the filler and tube wall, as demonstrated by previous studies [130,139,136] and illustrated in Fig. 3-5d.

The SHGM filler-tube wall interaction contributes to the overall energy absorption of the composite tube via two main mechanisms, namely the load transfer between the SHGM filler and the tube wall and the transform of the buckling mode from inward diamond mode to outward concertina mode [114]. Firstly, the perfect "liquid-solid bonding" allows for stable and efficient load transfer between the SHGM filler and tube wall. Consequently, hydrostatic pressure built-up in the SHGM uniformly (Fig. 3-3a) and all SHGM filler is involved in the deformation process without any dead zones [140], preventing the sharp load drop due to tube wall folding collapse. Instead, the SHGM-filled tube shows a smoothly increasing mechanical strength. Secondly, the filler-tube wall interaction suppresses the inward buckling of the tube and induces an outward buckling mode with increased cross-sectional area to bear more load. More importantly, the enhanced interaction leads to more severe plastic deformation of the tube wall and the attendant strain hardening [141] further promotes the stress level of the composite tube.

The promoted plastic deformation of the tube wall caused by the enhanced SHGM filler-tube wall interaction is further demonstrated using 3D digital image correlation (3D-DIC) technique. The empty and SHGM-filled tubes are spray painted with patterns of 3-7 pixel-sized speckles. The deformation contour of the patterns is tracked and captured by two angled cameras (Aramis V8, Trillion Quality Systems, LLC) at the rate of 1 fps, and later analyzed by the GOM Correlate Pro

software. Fig. 3-6 shows typical strain field of the tube wall in empty and SHGM-filled tubes. For empty tube, the major strain is zero initially. At ε = 0.1, the tube reaches a maximum major strain of 0.07 at the center line of the first tube wall fold, while the predominated unfolded part remains with a major strain less than 0.02. As the quasi-static compression progresses, more folds of the tube wall are formed. However, the characteristic of the plastic deformation pattern of the tube wall maintains. That is, the majority of tube wall in the region between adjacent folds, undergoes little plastic deformation. For SHGM-filled tube, the major strain of tube wall gradually increases from nearly zero to 0.17 as the quasi-static compression progresses. It can be observed that nearly all tube wall region undergoes relatively uniform plastic deformation due to the stable load transfer effect of the SHGM liquid filler. This severe plastic deformation promotes the energy absorption capacity of the tube wall and contributes to the overall performance of the composite structure.

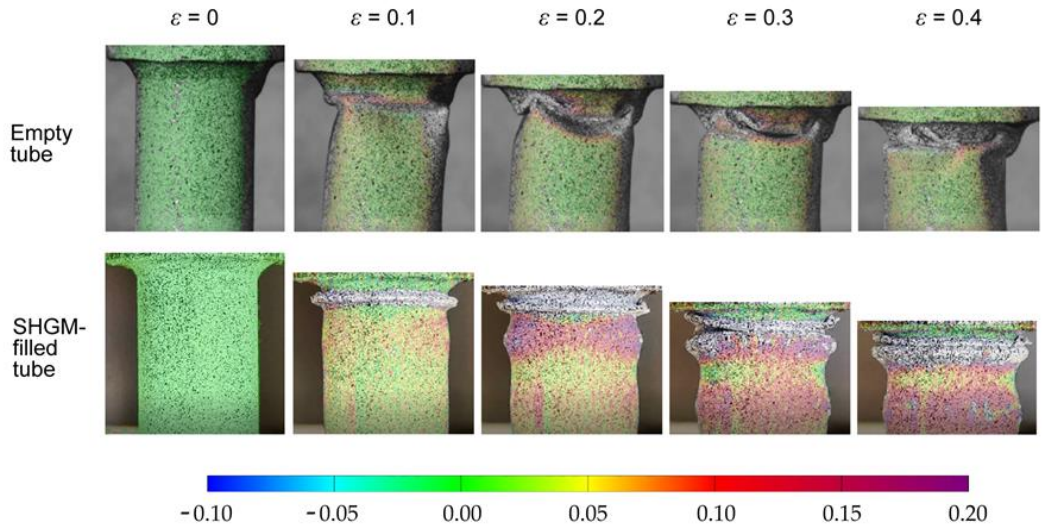

Figure 3-6: Typical strain field of the tube wall in empty and SHGM-filled tubes as the quasi-static compression progresses[142].

3.3.4. Dynamic Crushing Response of SHGM Filler

Fig. 3-7 represents typical dynamic response of the SHGM liquid filler under drop weight impact tests. Only the SHGM filler is evaluated under dynamic condition since it shows the best

performance in quasi-static compression tests. Under dynamic impact, initially, the crushing stress of SHGM filler is quite similar to that under quasi-static compression. As the strain reaches 0.25, the stress rises quickly and a reduced deformability of the SHGM material due to the inertia effect under high strain rate impact [143,144] can be observed. However, since only the SHGM with lower crushing strength engages in the reinforcement of the tube (Fig. 3-5b), this reduced deformability can be neglected and the mechanical response of SHGM filler is strain rate insensitive.

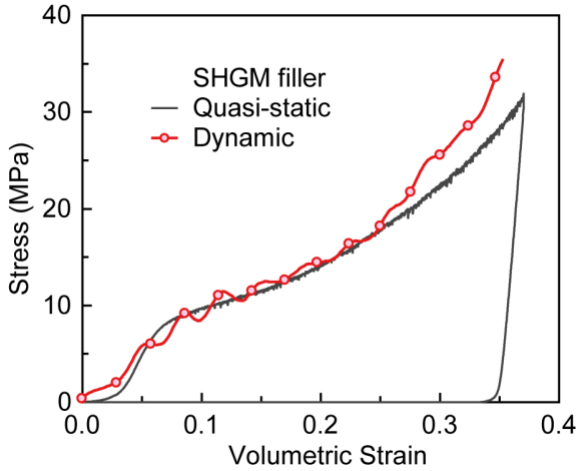

Figure 3-7: Typical dynamic crushing response of SHGM filler under drop weight impact test.

3.3.5. Dynamic Crushing Response of Tubes

The dynamic response of empty and SHGM-filled tubes has been evaluated under drop weight impact at the incident speed of 3.0 m/s. Typical dynamic stress-strain curves of tubes are shown in Fig. 3-8. The empty tube buckles at a similar initiation stress to that in quasi-static test, after which a post-buckling stress plateau is formed. The number and pattern of the undulations in the post-buckling plateau is almost the same as the quasi-static one, indicating that the increased strain rate does not alter the tube buckling mode. The average post-buckling stress is slightly higher than that in quasi-static test, which is due to the rate sensitivity of the tube wall material 304 stainless steel [145].

For SHGM-filled tube, the SHGM filler is activated at ε = 0.08, followed by a broad stress plateau. Given that the empty tube and SHGM filler show little strain rate sensitivity, the average post-buckling stress of SHGM-filled tube as shown in Fig. 3-8b is quite close to that in quasi-static test as expected. The SHGM-filled tube bursts at an average strain of 0.58. After tube burst, the SHGM liquid filler cannot flow out immediately under high strain rate impact and can function as a relatively low-strength filler. Therefore, the stress level after burst under dynamic impact is higher than that in quasi-static test. The performance of tubes under dynamic impact is summarized in Table 3-2. The *SEA* of empty tube at strain of 0.6 is around 6.5 J/g, while the *SEA* of SHGM-filled tube is 9.2 J/g, which is increased by 41%.

Table 3-2: Comparison of empty and SHGM-filled tubes under drop weight impact

ε = 0~0.6	Mass (g)	Height (mm)	*EA* (J)	*SEA* (J/g)
Empty tube	1.27 ± 0.03	20.3 ± 0.1	8.3 ± 0.4	6.5 ± 0.3
SHGM-filled tube	2.87 ± 0.06	20.3 ± 0.1	26.2 ± 1.7	9.2 ± 0.6

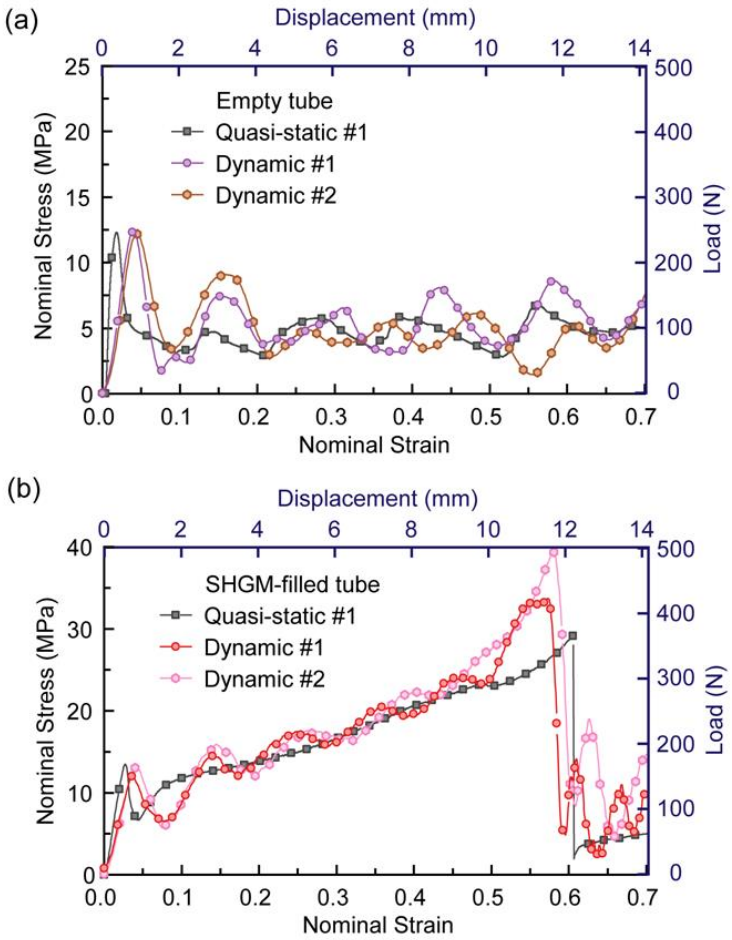

Figure 3-8: Typical stress-strain curves of (a) empty tubes (b) SHGM-filled tubes under drop weight impact. Stress-strain and load-displacement axes are inter-changeable. For each type of tube, curves of two samples are shown here for clarity.

Fig. 3-9 summarizes the energy absorption performance of tubes under both quasi-static compression and dynamic impact tests. In terms of *SEA*, the SHGM-filled tube is slightly lower than the empty tube at smaller strain. When the strain reaches 0.3, the *SEA* of SHGM-filled tube starts to exceed the empty tube. As the strain increases, the difference in *SEA* is further promoted. This higher *SEA* of SHGM-filled tube indicates the SHGM is a perfect filling material to improve the energy absorption capacity of thin-walled structures. With regard to energy absorption efficiency, the empty tube shows an average η of 0.37 in quasi-static test and 0.43 under dynamic impact. For SHGM-filled tube, η increases to about 0.70 in quasi-static test and 0.65 under dynamic impact. The increased η suggests that SHGM-filled composite structure

possesses a much more stable force response and can be used as a good energy absorber for vehicle crashworthiness.

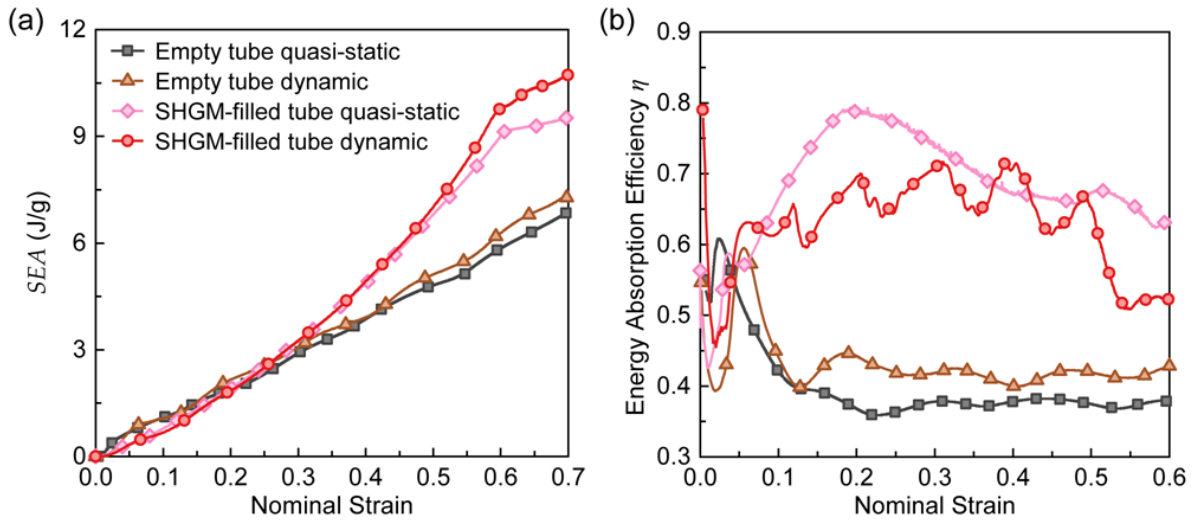

Figure 3-9: Comparison in (a) specific energy absorption SEA (b) energy absorption efficiency η of empty and SHGM-filled tubes under quasi-static compression and dynamic impact tests.

3.4 Conclusion

In this study, the SHGM was used as the filling material for thin-walled steel tubes and the crushing responses of this composite structure under both quasi-static compression and dynamic drop weight impact conditions have been evaluated experimentally. The energy absorption performance of SHGM-filled tube has been assessed using a number of crashworthiness indicators and compared to those of empty tube and HGM-filled tube. The underlying reinforcing mechanisms of SHGM-filled tube have also been investigated. Within the limitation, the following conclusions can be drawn:

(1) The SHGM filler significantly promotes the specific energy absorption *SEA* of the composite tube by 43% under quasi-static compression and 41% under dynamic impact compared to that of empty tube. The improvement of *SEA* is due to the much-enhanced SHGM filler-tube wall interaction as well as the high energy absorption capacity of SHGM.

(2) The enhanced SHGM filler-tube wall interaction in the composite tube is quantified by a strengthening coefficient of 4.0, much higher than that in best solid foam-filled metallic tubes. Due to its intrinsic fluidity, the SHGM filler maintains intimate contact with the tube wall during the tube crushing process, leading to an ultra-high strength "liquid-solid bonding" at the interface. Since the strengthening coefficient is positively related to the bonding strength, this "interfacial bonding" endows the SHGM-filled tube a much-enhanced interaction effect.

(3) The reinforcing mechanisms of this filler-tube wall interaction includes the load transfer effect between the SHGM filler and tube wall and the suppression of inward buckling, resulting in much more severe plastic deformation of the tube wall. This promoted plastic deformation is further demonstrated using 3D DIC technique. The empty tube wall shows a major strain of 0.07 at the center line of folds and ~0.02 at the predominated region between adjacent folds, while the whole SHGM-filled tube wall exhibits a relatively uniform major strain of 0.17 at ε=0.4. Thus, more tube material is engaged in the energy absorption process and promotes the crushing performance of the composite structure.

(4) The SHGM-filled tube exhibits an average energy absorption efficiency η of 0.70 under quasi-static compression and 0.65 under dynamic impact, much higher than those of empty tubes, i.e., 0.37 under quasi-static compression and 0.43 under dynamic impact. The high η of SHGM-filled tube is due to its relatively stable force response, especially the smoothly increasing post-buckling plateau.

In summary, the SHGM filling material shows great potential in promoting the energy absorption performance of thin-walled structures. The findings in this study have merit in designing next generation light-weight composite structures for vehicle crashworthiness.

Chapter 4 Interaction between LN and Thin-Walled Tubes with Imperfection

The previous chapter demonstrates advanced strategy to improve the energy absorption efficiency by applying the glass-bubble as a filler in the thin-walled tubes. However, the structure imperfection exists and is inevitable during transporting and handling process. To address this problem, this chapter validates LN filler is able to suppress the negative impact of structural imperfection. The mechanical performance of empty tubes and LN-filled tubes (LNFT) with different dent imperfections has been evaluated by quasi-static uniaxial compression tests. We verified that empty tube is susceptible to structural imperfection, as a V-shaped dent with 1.5 mm depth reduces the energy absorption capacity by about 20 %. In contrast, the mechanical performance of LNFT is insensitive to the existence and depth of the dent. The enhanced imperfection insensitivity of LNFT is due to the intimate liquid-solid interaction at the LN filler and the tube wall interface, which effectively suppresses the curvature growth of the dent and the localized folding. The findings provide an efficient approach for designing and engineering thin-walled energy absorption devices that are resilient and of high energy absorption capacity. The material presented in this chapter was published in *Thin-Walled Structures*.

4.1 Introduction

Thin-walled tubes have been widely applied as energy absorbers, due to their low cost, lightweight and high specific energy absorption capacity. To further improve their energy absorption performance, foam materials are usually employed as fillers in thin-walled tubes [66,146,147]. The axial compressive behaviors of foam-filled thin-walled tubes have been studied by many researchers [148–152]. Sun et al.[153] explored the effect of topological configurations on the

energy absorption performance of foam-filled multi-cell tubes and proposed approaches for crashworthiness topology optimization. Zhang et al.[154] and Fang et al. [155] investigated the effect of density gradient of foam fillers on the performance of thin-walled tubes and demonstrated the energy absorption capacity of graded foam-filled tubes outperformed their uniform counterparts. Many other strategies have also been developed for performance enhancement, including but not limited to foam-filled bitubal structures [156,157] ex-situ ordered cellular structure filled tubes [158], tube-filled syntactic foam [159], and metal/CFRP hybrid structures [160].

Despite the enhanced energy absorption performance of thin-walled tubes and their foam-filled counterparts, during the manufacturing, transporting, and handling processes, structural imperfections are inevitably introduced. It has been demonstrated that the load carrying capacity, the post-buckling strength and the energy absorption capacity of thin-walled tubes are significantly compromised when structural imperfections exist [161–166]. However, there is lack of solution to effectively suppress the negative impact of structural imperfections on the mechanical performance of thin-walled tubes.

To address above problem, liquid nanofoam-filled tube (LNFT), has shown significantly improved specific energy absorption capacity compared to empty tube and solid foam-filled tubes [123]. To investigate the effect of the LN filler on thin-walled tubes with structural imperfection, quasi-static uniaxial compression tests have been conducted on LNFTs containing single dent with controlled shape and depth. The mechanical response as well as energy absorption capacity of defective LNFTs have been evaluated to validate the suppression effect of LN filler on dent-induced performance loss.

4.2 Experimental Setup

4.2.1 Material and Dent Generation

In this study, the selected nanoporous material was a reversed phase silica gel (Supelco-C8) purchased from Sigma-Aldrich (No. 60759). The Supelco-C8 was hydrophobic as its surface was covered by octylsilane surface groups. The average pore size, specific pore volume, and particle size of the Supelco-C8 were 90 Å, 0.43 cm^3 /g, and 40–63 μm, respectively. The typical LN filler was composed of 0.5 g Supelco-C8 and 1.0 mL deionized (DI) water.

The cylindrical thin-walled tube used in this study was made of stainless steel (SS) 304 and acquired from Microgroup (No. 304F10500 × 006SL). The outer diameter and the wall thickness of the tube were 12.7 mm and 0.15 mm, respectively. The tube was cut into L = 25.4 mm segments for tube sample preparation. One V-shaped dent was generated at the midspan of each thin-walled tube sample with controlled depth (dent located at 1/2 L). As depicted in Fig. 4-1 (a), a V-notched solid steel rod template with a diameter of 12.3 mm was first inserted into the tube sample. Then, a dent with controlled depth, d, was generated on the tube wall by a wedge attached to an Instron machine (Model 5982).

4.2.2 Sample Preparation of LNFT

Before adding the LN filler into the defective tube, one end of the tube was inserted into an Aluminum cap and sealed by J-B Weld epoxy adhesive (No. 50112). A thin layer of adhesive was uniformly applied to both the outer surface of the tube and the inner surface of the cap. After the adhesive was fully cured at room temperature for 24 h, the LN filler with minimized air content was slowly injected into the tube. Additional DI water was injected into the tube to completely fill the inner space of the tube. A thin layer of grease was carefully placed on the top of the LN filler to eliminate direct contact of water and the adhesive. The tube end was capped

and sealed by the same method described above. Once the adhesive layers were applied, the LN-filled tube was vertically clamped on a vice for 24 h to make good alignment of the caps. The effective tube length of 20.3 mm was measured cap-to-cap distance as shown in Fig. 4-1b. Empty tubes sealed with two Aluminum caps were used as reference samples.

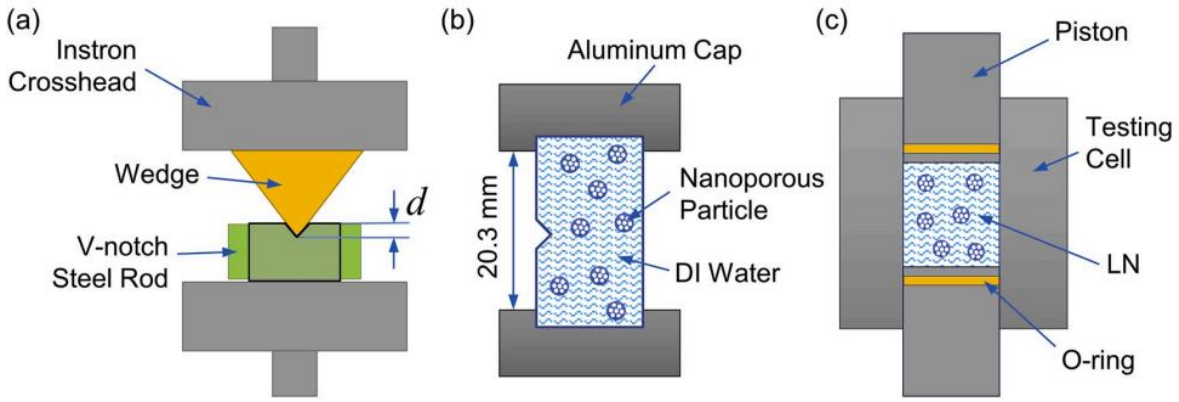

Figure 4-1: Defective LNFT sample preparation and experimental setup. (a) Schematic of dent generation with controlled shape and depth, (b) Typical LNFT sample, (c) Schematic of quasi-static compression tests for the LN filler.

4.3 Quasi-Static Compression Tests

For the pre-compression and liquid infiltration test of the LN filler, an SS316 testing cell was adopted as sketched in Fig. 4-1c. The LN filler was sandwiched by two pistons in a cylindrical sleeve. The sealing was accomplished by the O-ring fixed on each piston. The cross-sectional area of the cell, A, was 126 mm^2. The difference between pre-compression and liquid infiltration tests was the applied peak force which was 1.85 kN for pre-compression tests and 18 kN for liquid infiltration tests. The loading rate was 2 mm/min for both types of tests. No liquid leakage was observed in all tests.

Uniaxial quasi-static compression tests were conducted on empty tubes and LNFTs. The sample was placed on the Instron platen, and compressed at the loading rate of 2 mm/min. For

each dent depth, three samples were tested as shown in Table 4-1. No liquid leakage was observed at both sealed ends before tube bursting.

Table 4-1: LNFT sample with dent Category

Sample	Empty Tube	LNFT
Dent Depth (mm)	0	0
	0.5	0.5
	1.0	1.0
	1.5	1.5

4.4 Results and Analysis

Fig. 4-2a shows typical liquid infiltration behavior of the prepared LN filler. The applied external pressure is calculated as F/A, where F is the applied compression force. The specific volume change is the system volume change normalized by the mass of Supelco-C8 used in the LN filler. The system volume change is calculated as $V = D \cdot A$, where D is the measured axial displacement of the Instron platen. Under quasi-static loading, the mechanical response of the LN filler is composed of three sections. In the first linear elastic section, the applied external pressure is lower than P_{in} = 17 MPa, and no liquid molecules can enter the nanopores. In the second plateau section, the liquid molecules overcome the capillary effect and flow into the nanopores with the aid of the applied external pressure. The pressure plateau is defined as the liquid infiltration plateau. The width of the liquid infiltration plateau, ΔV, is about 0.43 cm^3/g and matches the total pore volume of Supelco-C8. In the third linear elastic section, all the nanopores are filled by liquid molecules and the LN filler performs as an incompressible liquid. When the applied external pressure is removed, the internal pressure of the LN filler drops

quickly to zero. The area enclosed in the hysteretic loading-unloading curve is the specific energy absorption capacity of the LN filler.

Fig. 4-2b shows the typical stress-strain curves of empty tube and the LNFT. For the empty tube, the initial buckling and post-buckling behaviors are clearly identified. Accordingly, the initial buckling strength (σ_i) is the stress at the ending point of the tube linear elastic response and the post-buckling strength (σ_p) is the average stress of the post-buckling plateau. As illustrated in Fig. 4-2b, when the strain, ε, is smaller than 0.10, the mechanical response of the LNFT is similar to that of an empty tube. This is because of the air trapped in the LN filler. Although pre-compression technique has been applied to minimize the air content, the hydrophobic nature of Supelco-C8 forms gas-liquid-solid interface around each particle. When ε is between 0.10 and 0.15, the air effect is eliminated by the tube deformation and then the LNFT performance is dominated by the liquid infiltration behavior of the LN filler. At ε = 0.15, the liquid infiltration is activated at an engineering stress of 11 MPa, which seems lower than the characterized P_{in} of the LN filler. This is due to the lateral expansion of the LNFT, which makes the engineering stress smaller than the true stress value. When $0.15 = \varepsilon \leq 0.60$, a stress plateau with smallest slope in Fig. 4-2 is observed. This is attributed to the increased cross-sectional area of the LNFT as well. The plateau width, equivalent to a strain of 0.46, is determined by the total pore volume of Supelco-C8 in the LN filler. At ε = 0.61, the hoop stress developed in the tube wall reaches the failure strength of SS 304 and the LNFT bursts, followed by leakage of the LN filler. The mechanically failed LNFT deforms as an empty tube with vertical dent and has reduced post-buckling strength compared to empty tube, which is dent-free.

The typical continuum behavior of empty tubes and LNFTs with dent is exhibited in Fig. 4-3 a and b. In general, the buckling behavior of tubes with dent is similar to that of intact tubes,

which is a high-stress initial buckling followed by a post-buckling plateau. With the presence of dent, (σ_i) of tubes with and without LN filler and σ_p of empty tubes are reduced, while (σ_p) of LNFTs does not vary too much.

4.5 Discussion

4.5.1 Negative Impact of Dent on Initial Buckling Strength

As described above, when the axial strain is small ($\varepsilon < 0.15$), the LN filler has no effect on the tube buckling behavior due to the small amount of air trapped at the particle-liquid interface. This is confirmed by Fig. 4-4a, σ_i of both empty tube and LNFT linearly decreases with increased d. The strength reduction is attributed to the increased size of the dominant structural defect on the tube, i.e. the dent, and the local bending behavior of the defective tube [167]. As the artificial dent is the largest defect on the tube, it acts as the weakest chain and determines σ_i of the resulted tube. In addition, the defective tubes are geometrically asymmetric. The dent-induced localized folding leads to bending of the tubes instead of stabilized buckling, which further reduces σ_i. As revealed in Fig. 4-4b and c, the dent-induced bending is observed in all defective tubes when $\varepsilon < 0.15$. Therefore, the presence of the dent negatively affects σ_i of both empty tube and LNFT due to the combined dent size effect and dent-induced local bending.

4.5.2 Dent Effect on Post-Buckling Behavior of Empty Tube

As shown in Fig. 4-3a, once the external load reaches σ_i, the load carrying capacity of all empty tubes drops abruptly by following a same pathway except the defective tube with d =1.5 mm (inset of Fig. 4-3a). The detailed progressive tube buckling is summarized in Table 4-2. At $\varepsilon = 0.15$, local plastic hinges are fully developed at the top buckling fold of the intact empty tube. Therefore, the tube collapses and temporarily loses all its load carrying capacity till the formation of the 2nd fold. In comparison, for the defective empty tube with d = 1.5 mm, the dent-

induced bending leads to a larger buckling fold at the bottom half of the tube. The development of the plastic hinges is inhibited by the "central vertical ribbon", which provides the defective tube with additional loading carrying capacity.

With increased axial deformation, the intact empty tube repeats the buckling fold and formation of next fold from one end to the other. As shown in Fig. 4-3a, the average axial strain of the intact empty tube associated with each buckling fold is around 0.15. After four consecutive diamond buckling folds [168], the tube is solidified. Both the length and the number of buckling fold match well with the theoretical prediction [162,165,166].

With the presence of dent, the post-buckling behavior of the defective tube always initiates at the dent location. As illustrated in Table 1, when d = 0.5 mm, the width of the dent in the lateral direction increases. Meanwhile, at $\varepsilon = 0.3$, a normal diamond mode wrinkle forms at the top end of the tube. The deformation history of the tube agrees well with the first bump in the post-buckling stress plateau (green curve in Fig. 4-3a). The peak stress of the bump is close to that of an intact empty tube. At this dent depth, the localized buckling fold development is not affected by the dent. As tube buckling progresses ($0.35 < \varepsilon < 0.5$), the tube wall deformation is dominated by the inwards folding of the dent. With increased inwards deformation and dent width, plastic hinges are developed around the dent, which leads to the local collapse of the tube. Therefore, in this dent-dominated region, the stress of the defective tube.

When d increases to 1.5 mm, not only the width of the dent but also the curvature of the dent increases with larger strain. The whole bottom half of the defective empty tube is dominated by the X-shaped dent-induced plastic hinge (Table 4-2). The collapse of the plastic hinge leads to a lower and much flatter stress plateau ($0.10 < \varepsilon < 0.45$, red curve in Fig. 4-3a, which is consistent with previously reported results [169,170]. When the curved and extended dent is in contact with the

bottom cap at ε around 0.45 (Table 4-2), the tube stiffness increases. Thereafter, only one diamond buckling fold is developed in the top half of the defective empty tube, as also indicated by the only bump at ε = 0.52 in the red curve in Fig. 4-3a. With increased dent depth, the dent-induced plastic hinge collapse dominates the post-buckling behavior of the defective tube. Consequently, less buckling folds in diamond mode are fully developed and the load carrying capacity of defective tube is further weakened.

4.5.3 Dent-Inert Post-Buckling Behavior of LNFT

From the stress-strain curves in Fig. 4-3b, the post-buckling behavior of LNFT is inert to the presence of the dent and the dent depth. Smooth stress plateaus with similar width and stress range are formed in all LNFT tubes with different dent depths. The dent-inert post-buckling behavior of LNFT is attributed to the effect of the LN filler on the dent growth pattern as well as the tube buckling mode. As shown in Table 4-2, although the width of the dent grows with increased axial strain of the LNFT with d = 1.5 mm, the curvature of the dent does not change. The pattern of dent growth in LNFT is different from the one in defective empty tube as most of the external loading is carried by the LN filler. Even if plastic hinges were fully developed on the tube wall, the LNFT would not collapse and lose its load carrying capacity. Therefore, the dent-induced local deformation is suppressed by the LN filler.

In addition, the inward diamond buckling fold is prohibited and outward concertina buckling wrinkles are formed along the tube, due to the internally built hydrostatic pressure in the LNFT [123,171]. At larger strain (ε > 0.30), a mixed buckling mode of diamond fold and concertina wrinkle is observed in the LNFT, where the initial buckling fold is formed due to the trapped air in LN filler. The mixed buckling portion of the intact LNFT is much shorter than that of the defective LNFT, which has nearly no effect on the continuum behavior of the LNFTs. Therefore, the

buckling behavior of LNFT in the mixed zone is dominated by the concertina buckling triggered by the LN filler. For the rest part of the LNFT, single wrinkle in defective LNFT or multiple wrinkles in the intact LNFT grow into bulged tubes. The adverse effect of dent is further mitigated by the LN filler, as the localized diamond folding of empty tube is converted into global bulging of the LNFT.

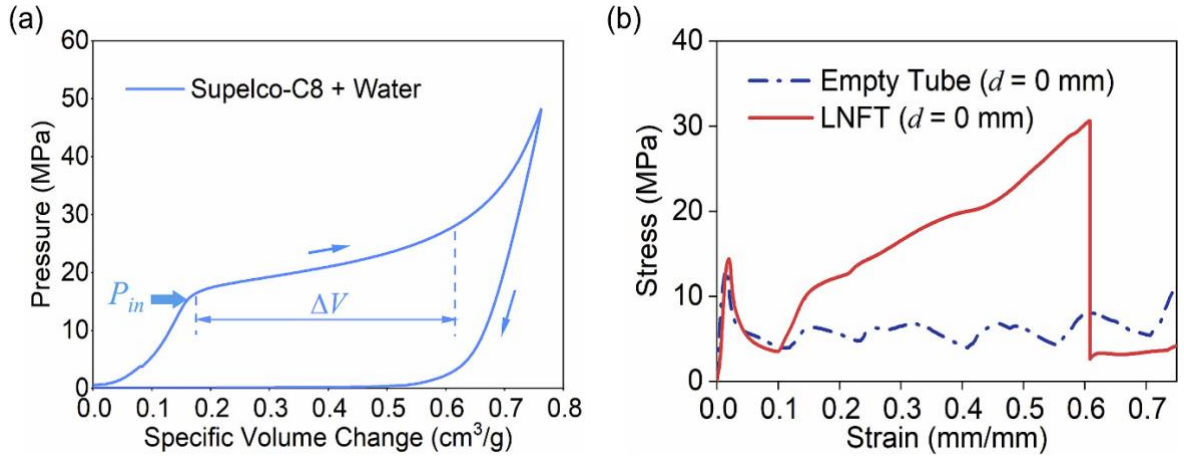

Figure 4-2: (a) Liquid infiltration behavior of LN filler composed of Supelco-C8 and DI water, (b) Continuum behavior of empty tube and LNFT without structural imperfection.

The subtle differences in the stress plateaus in Fig. 4-3b provide more insight on the suppression effect of the LN filler on dent-induced deformation. As shown in the inset of Fig. 4-3b, at the onset of the post-buckling plateau ($0.15 < \varepsilon < 0.30$), the stress of LNFTs decreases with increasing dent depth. From the snapshots listed in Table 4-2, the dent grows in lateral direction and the area around the dent folds inwards. This is due to the relatively weak filler-tube wall interaction, which is not sufficient to fully suppress the dent-induced inwards folding. Previous studies have demonstrated that the filler-tube wall interaction is related to the strength of solid fillers or the infiltration pressure of LN fillers [123,171,172]. Due to the pore size distribution of Supelco-C8, larger nanopores are firstly triggered for liquid infiltration, which provides a relatively lower P_{in} of 17 MPa. Therefore, the stress of defective LNFTs is adversely affected by the dent. As $\varepsilon > 0.40$, the higher P_{in} associated with smaller nanopores in the LN enhances the

filler-tube wall interaction, so that the inwards folding of the dent is fully suppressed. Apparently, no dent-induced collapse is allowed in LNFT. Meanwhile, the tube wall itself becomes more prone to buckle inwards as the folding collapse progresses. The dent-induced plastic deformation of the tube wall leads to an enhanced strain hardening effect [171,173] which results the improved filler-tube wall interaction as well as the load-bearing capacity of the defective LNFT and helps the tube wall to hold higher P_{in} [174] at the end of the post-buckling plateau ($0.40 < \varepsilon < 0.60$ in Fig. 4-3b). Therefore, the burst stress of LNFT is increased from 30 MPa to 34 MPa as dent depth changes from 0 to 1.5 mm (Fig. 4-3b).

As an energy absorber, it is vital to evaluate the energy absorption capacity [175,176] EA, of the empty tubes and LNFTs with various dent depths by using Eq. (4-1), and their specific energy absorption capacity (energy per unit mass), SEA, given by Eq. (4-2).

$$EA = V_0 \int_0^{\varepsilon_b} \sigma d\varepsilon \qquad (4-1)$$

$$SEA = \frac{E}{m} \qquad (4-2)$$

Where $V_0$the effective tube volume and m is the mass.

The results are summarized in Table 4-3. The energy absorption capacity of the intact empty tube and the LNFT are 8.6 J and 24.2 J, respectively. Fig. 4-5a depicts the relationship between the retained energy absorption capacity and the dent depth of both empty tubes and LNFTs. For empty tubes, by increasing d from 0 mm to 1.5 mm, the retained energy absorption capacity linearly decreases to 82% of the intact empty tube. For LNFTs, the retained energy absorption capacity slightly decreases (< 2%) with the presence of dent, which is mainly resulted from the reduced σ_i. Similar trends are also observed in the *SEA* curves in Fig. 4-5b. The *SEA* of empty tubes keeps decreasing with increased dent depth, while the *SEA* of LNFT slightly increases due to the reduced mass of the whole composite structure. Clearly, the negative impact of the dent on

the post-buckling behavior of thin-walled tube is effectively suppressed by the LN filler. With the existence of the LN-filler, hydrostatic pressure is uniformly built up in the LNFTs, which is independent from the compression direction. However, the compression direction may alter the tube wall buckling mode into a bending one. The additional LN-filler effectively enhances the bending stiffness of the LNFTs and thus enhances the energy dissipation in the bending mode as well.

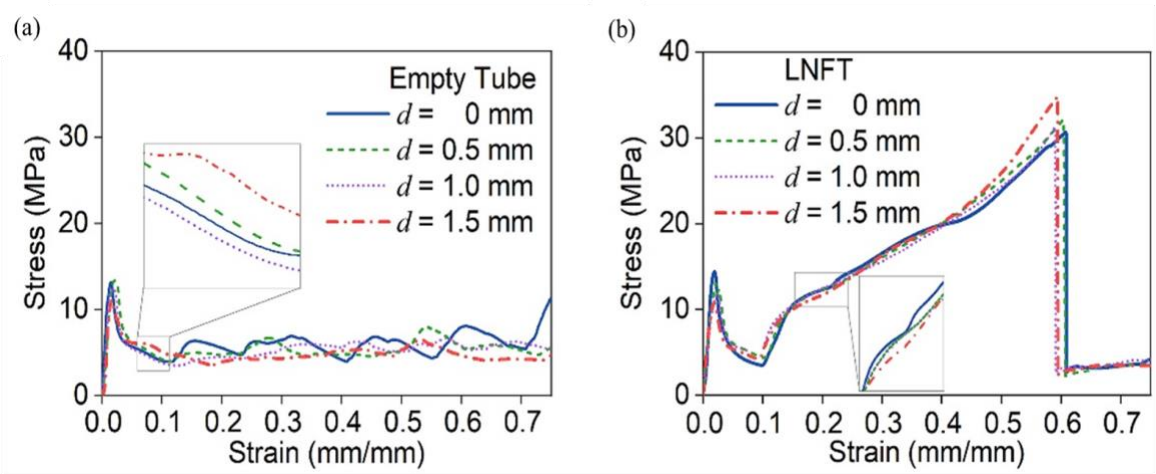

Figure 4-3: (a) Continuum behavior of empty tubes with different dent depths, and (b) Continuum behavior of LNFTs with different dent depths.

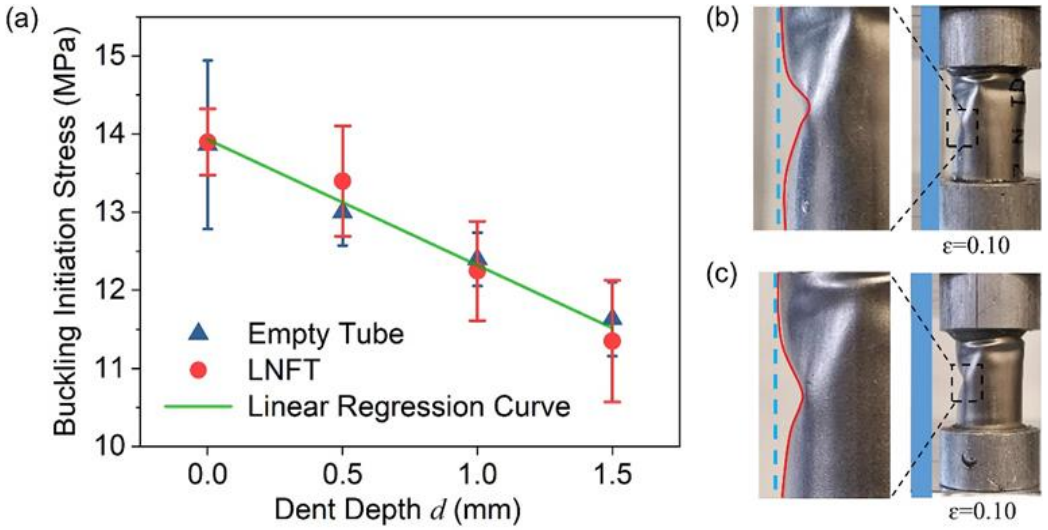

Figure 4-4: Dent effect on initial buckling strength and dent-induced bending of empty tube and LNFT. (a) The linearly reduced initial buckling strength with increased dent depth (The error bar is calculated based on three samples), (b–c) Side view of deformed tubes (b) Empty tubes with d = 1.5 mm, and (c) LNFT with d = 1.5 mm.

Table 4-2: Snapshots of Progress Tube Buckling

ε (mm/mm)		0	0.15	0.30	0.45	0.60
Empty Tube		Reinforcement		Dent-reduced post-buckling		
	d=0mm					
	d=0.5mm					
	d=1.5mm					
LNFT		Trapped air		Dent-suppression by LN filler		
	d=0mm					
	d=0.5mm					
	d=1.5mm					

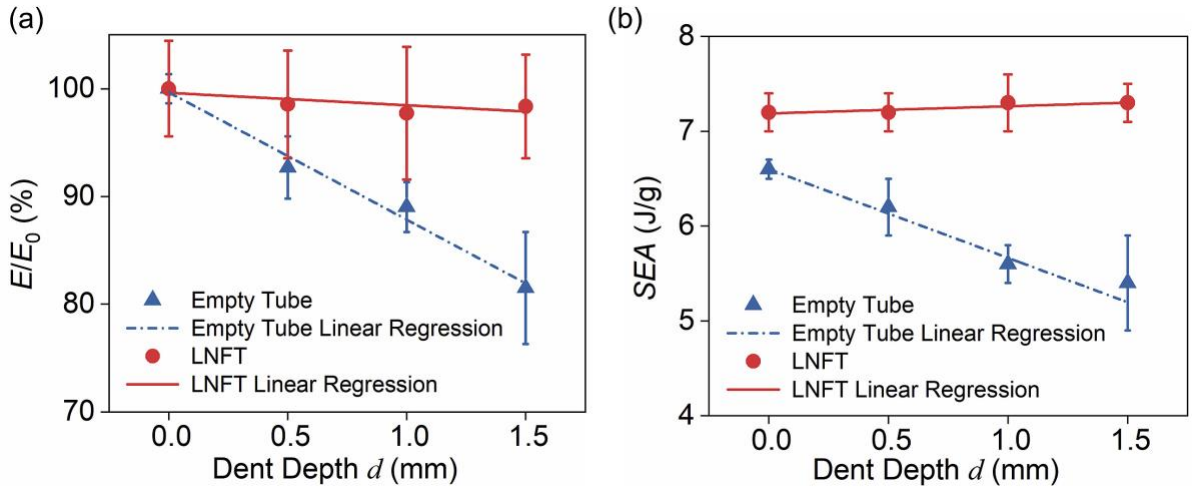

Figure 4-5: Dent-suppression effect of the LN filler. (a) The retained energy absorption capacity of defective empty tubes and LNFTs compared to their intact counterparts, and (b) The SEA of empty tubes and LNFTs with various dent depths (The error bar is calculated based on three samples).

Table 4-3: Energy absorption performance of empty tubes and LNFTs with various dent depths (The error bar is calculated based on three samples)

	d (mm)	Mass (g)	E (J)	SEA (J/g)	E/E_0 (%)
Empty Tube	0	1.29 ± 0.03	8.6 ± 0.2	6.6 ± 0.1	100 ± 2
	0.5	1.29 ± 0.03	8.0 ± 0.4	6.2 ± 0.3	92 ± 3
	1.0	1.29 ± 0.03	7.3 ± 0.3	5.6 ± 0.2	89 ± 2
	1.5	1.29 ± 0.03	7.0 ± 0.6	5.4 ± 0.5	81 ± 5
LNFT	0	3.35 ± 0.05	24.2 ± 0.5	7.2 ± 0.2	100 ± 4
	0.5	3.30 ± 0.07	23.8 ± 0.6	7.2 ± 0.2	99 ± 5
	1.0	3.26 ± 0.08	23.6 ± 0.8	7.3 ± 0.3	98 ± 6
	1.5	3.24 ± 0.08	23.5 ± 0.6	7.3 ± 0.2	98 ± 5

4.6 Dent Location Effect

To further study the effect of dent location, empty tube and LNFT samples with dent located at 1/4 of the tube length were prepared and evaluated under the same testing conditions Fig. 4-6 shows the effect of dent location on the mechanical response of empty tubes and LNFTs. For empty tubes, as the dent location changes from 0.5 *L* to 0.25 *L*, the post-buckling behavior remains the same except that the stress level is slightly reduced (Fig. 4-6a). This stress reduction is attributed to the asymmetry induced system instability. The mechanical response of LNFTs with different dent locations is stable, indicating the dent location effect is negligible. This is further validated by the *SEA* shown in Fig. 4-6b. The dent-suppression effect of the LN-filler is independent from the dent location.

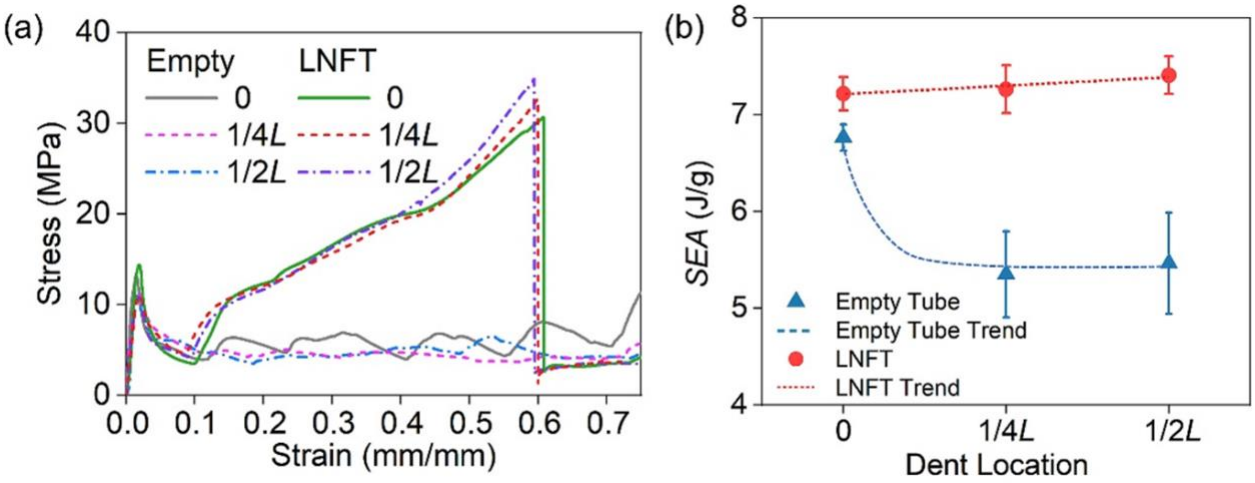

Figure 4-6: Effect of dent location on the performance of empty tubes and LNFTs with dent depth *d* = 1.5 mm. Dent location at 0 means dent-free. (a) Continuum behavior of empty tubes and LNFTs with different dent locations, and (b) The SEA of empty tubes and LNFTs with different dent locations.

4.7 Conclusion

The effect of dents on thin-walled tubes with and without LN filler has been investigated by quasi-static uniaxial compression tests. Based on the comparison of energy absorption performance of thin-walled tubes with and without LN filler, the following conclusions are

drawn: (a) The empty tube is vulnerable to dent which greatly reduces the initial buckling strength, the post-buckling strength, and the energy absorption capacity. (b) The reduction in mechanical performance of empty tube is linearly proportional to the dent depth. In contrast, the LNFT is inert to dent depth and location, as demonstrated by the preserved energy absorption capacity. (c) The underlying mechanism of the dent-inert energy absorption performance of LNFT is the intimate liquid-solid interaction at the LN filler and the tube wall interface, suppressing the curvature growth of the dent and the localized folding [122].

4.8 Summary

In this chapter, we have validated that the LN filler in the thin-walled can effectively suppress the imperfection in the tube. The LN filler not only increases the energy absorption capacity and SEA of LNFT, but also provides an economical approach to reduce the cost on quality control and handling of thin-walled structures. These findings not only address the puzzling question regarding the imperfection on the tube, but also provide guidance for designing high-performance liquid nanofoam-based energy absorption materials and devices.

Chapter 5 Interaction between LN and Biotissues

This chapter presents the protective impact of the LN-functionalized material on biotissue. Blunt force trauma (BFT), the injury of the body by forceful impacts such as falls, motor vehicle crashes and collisions, causes damage to bio-organs that can lead to life-threatening situations. To address the unmet need of bioprotection materials for BFT, we developed a novel, liquid nanofoam (LN) based system. The LN system employs a unique mechanism of energy absorption, i.e. the external force aided nanoscale liquid flow. Under mechanical loading, the LN system effectively protected human cells from force-induced deformation and cell death. Moreover, LN mitigated upregulation of stress and inflammatory genes relevant to traumatic injuries. Strikingly, LN prevented blunt-force damage of multiple vital organs including liver, heart, and lungs. To our knowledge, this is the first material of its kind that is biocompatible and capable of effectively protecting biotissues from mechanical loading-induced damage on molecular, cellular and tissue levels. The material presented in this chapter was submitted to *Scientific Reports*.

5.1 Introduction

Blunt force trauma (BFT) refers to injury of the body by forceful impacts such as falls, motor vehicle crashes and collisions. It is expected that BFT will become the third largest contributor to the burden of disease with 46,980 deaths and 5.4 million injuries caused by motor vehicle crashes in 2021 alone [177]. A significant adverse outcome of BFT is internal injuries. It is estimated that at least 65% of all severe trauma cases involve vital organs such as the liver, kidneys, heart and lungs, necessitating urgent medical intervention and potentially causing long-term complications or even life-threatening situations [178,179]. Liver rupture, for example, often caused by a direct impact on the abdomen at specific velocities and energies, can lead to severe blood loss, shock, and immediate death [180,181]. Patients of acute kidney injury experience long-

term risk of developing fibrosis and chronic kidney disease [182–186]. Cardiac injuries ranging from insignificant contusion to fatally rupture is related to 75% of traumatized patients. They significantly increased the risk of thoracic and intra-abdominal injuries [187,188]. Lung contusion affects 17% - 25% of adult BFT patients and can increase the risk of pneumonia, severe acute lung injury, and the acute respiratory distress syndrome [189]. Therefore, there is a critical need to develop an effective personal protection device to prevent and reduce severe blunt-force injury to biological tissues.

Stochastic and periodic foams are widely used in energy absorption devices for automotive, aerospace, packing, contact sports, and military applications [190–194]. Foams have attractive physical and mechanical properties including extremely lightweight, large deformability and easy fabrication. The main energy mitigation mechanism of foams is based on the permanent deformation including bending, buckling, and stretching of the cellular structures. When the foam structure is crushed, the externally applied energy is dissipated into heat.

While these materials are highly effective as cushioning in packages and protection devices of infrastructures, the protection of biological tissues from BFT remains a unique challenge. This is mainly attributed to the low energy mitigation efficiency, and the dissimilar properties between the foams and biological tissues. For currently used foam materials, the measured energy mitigation efficiency is in the range of 0.5 J/g - 20 J/g [55]. For biotissue protection, the working pressure of the foams has an upper limit at the order of 1 MPa [54], which limits the energy mitigation efficiency to the lower end of the above range, which is insufficient for the protection from BFT. Data has shown that advanced foam liners implemented in sports helmets in recent years are not effective in concussion prevention [195–197]. In addition, under mechanical loading, foams can be deboned from the surface they are initially adhered to, which leads to a much lower real energy

mitigation efficiency than the experimentally measured values [198]. By far, a non-solid energy mitigation material has yet to be developed.

To address the unmet need of efficient biotissue protection from impact, we have designed a novel, liquid nanofoam (LN)-based material [199–202]. The LN is a liquid suspension of hydrophobic nanoporous particles (NpPs) in a non-wettable liquid. At ambient condition, the liquid molecules cannot enter the empty nanopores contained by the NpPs due to the energy barrier at the interface of the liquid and the nanopore surface. When an external force is applied on the LN, hydrostatic pressure builds up in the liquid. Once the pressure surpasses a critical threshold named as the infiltration pressure of LN, the potential energy stored in the liquid molecules is high enough to overcome the surface energy barrier. Consequently, the liquid molecules flow into the nanopores and the potential energy carried by them is dissipated as heat. This infiltration process leads to an extremely high energy efficiency, up to 100 J/g, which is 10 times higher than the energy absorption efficiency of solid foam-based protection materials [203].

The unique property of high energy mitigation efficiency and fluid-like nature raises the possibility of using LN to protect biological tissues from blunt force trauma. To test this possibility, we investigated the biocompatibility of LN using human culture cells. In addition, we analyzed the protective efficiency of LN on both cultured cells and whole animal organs. Our study revealed the high biocompatibility and low cytotoxicity of the LN material. In addition, the LN demonstrated significant and substantial protection of multiple biological tissues from quasi-static compressions. This research suggests the potential of LN as a novel and effective energy-absorbing medium for the protection of biological tissues from BFT.

5.2 Material and Methodology

5.2.1 Cell Culture Treatment

In this investigation, HEK 293T cells are employed, and the procedural framework of culture treatment is outlined in Fig. 5-1. The culture medium consisted of Dulbecco's Modified Eagle's Medium (DMEM) supplemented with 10% Fetal Bovine Serum (FBS), 1% antimycotic-antibiotics, and 2 mM L-glutamine. Thaw the cell vial with gentle agitation in a 37 °C water bath. Transfer the vial contents to a centrifuge tube containing 9.0 ml of culture medium and aspirate cells by gently pipetting. Dispense cells into two 10-cm dishes (Thermo Fisher, Nunc™ EasYDish™ Dishes) at a density of 1 x 10^6 cells per dish. Maintaining the dishes in an incubator at 37 °C under 5% CO_2 conditions (Fig. 5-1a).

Upon achieving confluency of 90% within 2-3 days, the culture medium is aspirated and removed, followed by a thorough rinsing with Ca++/Mg++ free Dulbecco's phosphate-buffered saline (D-PBS). Subsequent to this, 2 ml of 0.05% Trypsin-EDTA solution is introduced into the dish, allowing a 10-minute incubation period for detachment of the cell layer. Following detachment, 8 ml of culture medium is added, and cells are gently detached by pipetting. These cells are then collected into a 15 ml-conical tube and subsequently seeded onto coverslips in a 24-well plate (Thermo Fisher, Nunc™ Cell-Culture Treated Multidishes) for their intended utilization in the compression test Fig. 5-1b.

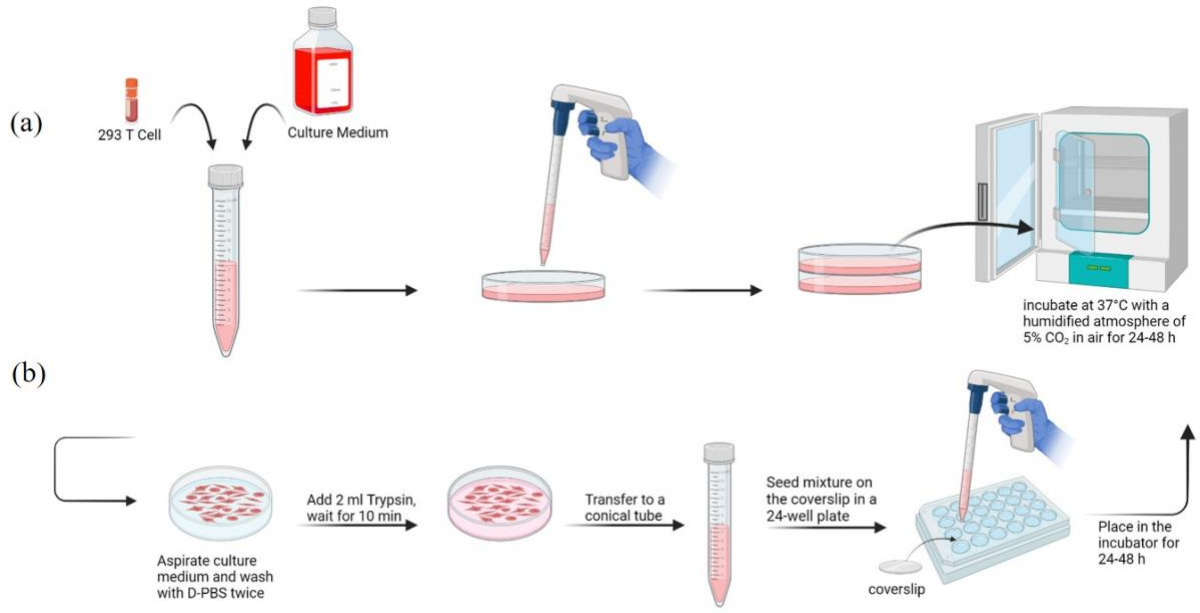

Figure 5-1: Cell culturing (a) Schematic of 293 T cell seeding process and culture procedure. (b) 293 T cell culture on the Poly-L-lysine coating coverslip.

5.2.2 Coverslip-Coating Protocol

The coverslip (Bellco Glass Inc. Round German Coverslip 12Mm, #1 Thick) intended for cell seeding in the compression test undergoes an initial cleaning process using 70% alcohol before being positioned within a designated location in a 24-well plate. Add 2 ml of Poly-L-Lysine solution (Sigma Aldrich, CAS-No: 25988-63-0, 0.1% in sterile water) to each well of a flame-cleaned 24-well plate. After application, allow the solution to evenly coat the glass surface for 20 minutes, facilitating enhanced cell adhesion and protein absorption by modifying surface charges on the culture substrate. Subsequently, remove the solution by suction. The coverslip undergoes three subsequent washes with D-PBS before being left to dry for 15 minutes under ultraviolet sterilization and an additional hour at room temperature. Subsequently, cells are seeded onto the coverslip at a density of 0.05 x 10^6 cells per well. The seeded 24-well plate is then incubated at 37 °C under 5% CO_2 conditions to facilitate cell adherence and growth.

5.2.3 Infiltration Tests of LN

A type of hydrophobic nanoporous silica (Perform-O-Sil 668, Nottingham Corp.), is chosen as the NpPs for this investigation because of the extremely large porosity to maximize the total deformation of the LN system. Initially received in powder form, the average particle size and nanopore diameter of the NpPs are 4 μm and 115 nm, respectively. The LN samples containing 0.10 g of NpPs and 2.0 mL liquid are sealed in a stainless-steel (SS316) cylindrical testing chamber by two pistons equipped with o-rings. The cross-sectional area of the testing chamber, *A*, is 286 mm^2. The LN samples are compressed by a universal tester (Model 5982, Instron) at a constant loading rate of 2 mm/min (Fig. 5-4a). Once a peak loading force of 3.0 kN is reached, the cross head of the Instron is moved back at the same rate. During all tests, no leakage of liquid is observed.

To ensure the biocompatibility of the LN, various cell growth mediums are selected for sample preparation, including 293T culture medium [Dulbecco's Modified Eagle's Medium (DMEM), 10% Fetal Bovine Serum (FBS), 1% antimycotic-antibiotics, and 2mM L-glutamine], PBMC culture medium [Roswell Park Memorial Institute (ROMI-1640) media with 10% FBS, 1% sodium pyruvate, 1% nonessential amino acds, 1% Beta-Mercaptoethanol, 1% L-GLU, 1% p/s] and stem cell culture medium (mTeSR™ Plus Basal Medium and 20% mTeSR™ Plus 5x Supplement). Deionized water is also selected as the liquid phase for the control group.

5.2.4 Quasi-static Compression Tests on Cells Covered by LN

Cells are seeded onto coverslips (Bellco Glass Inc. Round German Coverslip 12 Mm, #1 Thick) treated with Poly-L-Lysine solution (Sigma Aldrich, CAS-No: 25988-63-0, 0.1% in sterile water) and the experimental setup for cell compression testing parallels the methodology employed for LN infiltration. Coverslips with seeded cells are positioned within a cleaned SS316

testing chamber treated with 70% alcohol. A layer of 0.10 g of NpPs is then added on the surface of the liquid, followed by the insertion of the top piston. The identical setup without NpPs serves as a control group. Post-compression analysis includes an assessment of cell viability via trypan-blue staining and deformation, both with and without NpPs. To ensure the credibility and replicability of results, each specific experimental condition is subjected to triplicate testing.

5.2.5 Cell Viability Assay

Prior to usage, ensure the glass hemocytometer and coverslip are thoroughly cleaned using 70% alcohol. The cell viability assay procedure is indicated in the Fig. 5-2. Step 1, return coverslips containing cells from the compression test to the 24-well plate with fresh culture medium. Step 2, gently remove excess culture medium to expose the cells to air. To disperse the cell layer, add 200 µL of Trypsin-EDTA per well, ensuring complete coverage of the coverslip, and allow it to sit for 10 minutes. Subsequently, add 200 µL of culture medium into the well and gently pipette to aspirate the cells. Transfer collected cells into a 0.5 ml Eppendorf tube, ensuring even distribution through gentle pipetting. Step 3, take 10 µL of the suspension liquid into a new 0.5 ml Eppendorf tube and mix it with 10 µL of 0.4% Trypan Blue (Fisher Scientific, Gibco™ 15250061). Apply a drop of the Trypan Blue/cell mixture onto a hemocytometer. Place the hemocytometer on the stage of a microscope and focus on the cells. Proceed to count the unstained (viable) and stained (nonviable) cells separately within the hemocytometer. Each sample is subjected to three counts to mitigate potential outliers, and the resulting average is considered as the final outcome.

$$\text{Viability } (\%) = \frac{\#\text{ of Live cells}}{\#\text{ of Live cells} + \#\text{ of Dead cells}} \times 100\ \% \qquad (5-1)$$

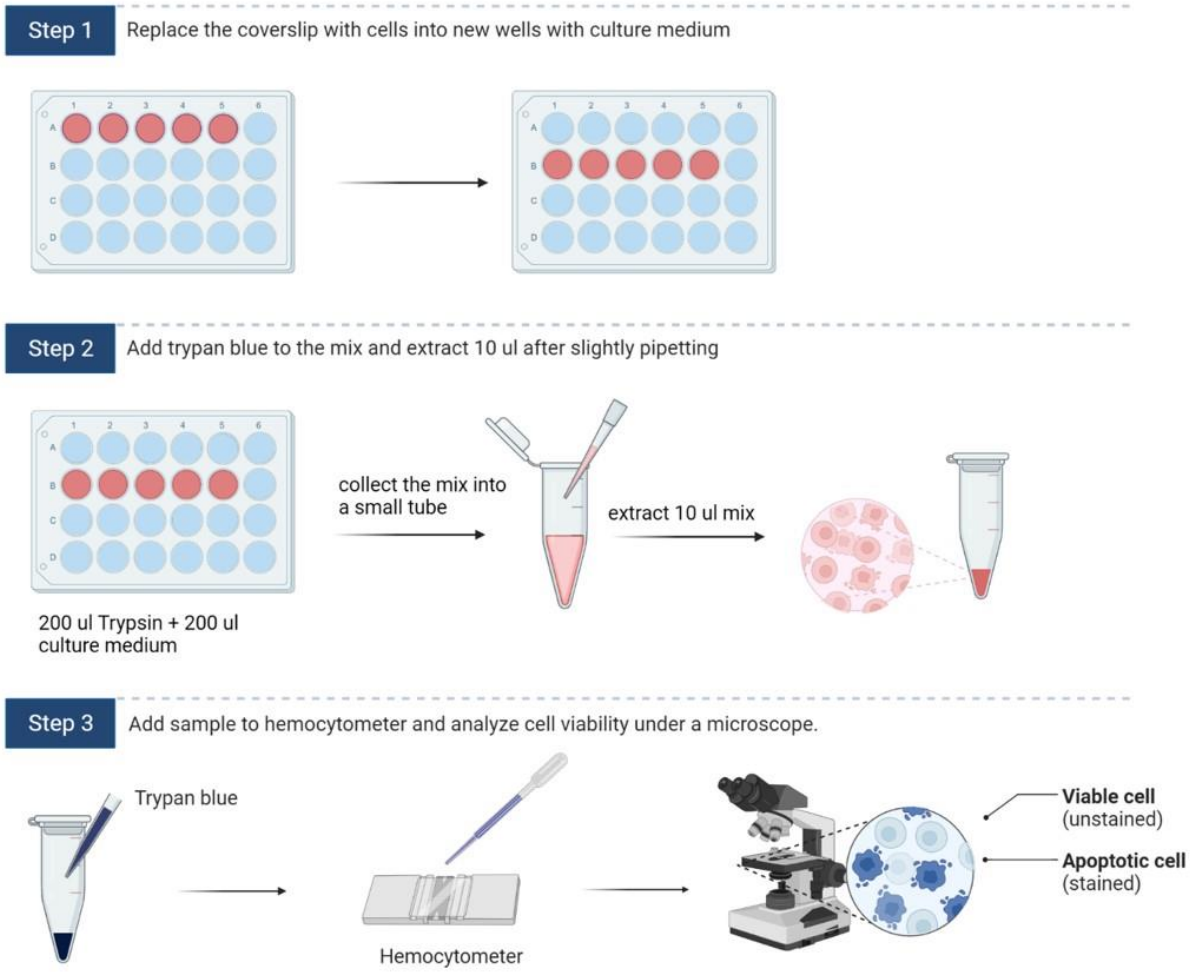

Figure 5-2: Cell collection and viability assessment using the Trypan Blue method after compression test. (step1) Place cells in newly filled wells with fresh culture medium, (step 2) Detach cells from the coverslip and collect them into a small tube, (step 3) Perform viability. Assessment by utilizing Trypan Blue.

5.2.6 RNA Isolation, cDNA Synthesis, and Polymerase Chain Reaction (qPCR)

RNA isolation

After the compression, the collected cell mixture in a 0.5 ml Eppendorf tube is centrifuged at 300 g for 5 min to form a cell pellet. Following this, 500 µL of Trizol and 100 µL of Chloroform are added, and the mixture is incubated at room temperature for 3 minutes. Subsequently, the solution is centrifuged at 12,000 g at 4 °C for 15 min. The upper mRNA liquid is carefully

extracted into a 0.5 ml tube and subjected to washing with 70% alcohol and RNase-free water several times to obtain the final RNA pellet, as depicted in Fig. 5-3a. In the post-compression test, the isolation of five distinct RNA types is imperative. These include RNA samples from uncompressed cells, cells subjected to low input energy with and without exposure to LN, as well as cells exposed to high input energy with and without LN.

cDNA synthesis

The computed RNA amount is annealed with 1 µL of primer Oligonucleotide (dT), 1 µL of dNTP, and the required volume of H_2O (The total volume, comprising the calculated RNA amount and H_2O, is 10 µL), employing the Superscript IV system (Thermo Fisher 18091050). This process involves heating to 65 °C for 5 min to facilitate primer annealing, succeeded by incubation on ice. Subsequently, the components of reverse transcription (RT) mix, including 4 µL 5x SSIV buffer, 1 µL-100Mm DTT, 1 µL ribonuclease inhibitor, and 1 µL reverse transcriptase, are prepared. The prepared RT mix is then added to the annealed RNA template, thoroughly mixed, and incubated in a thermal cycler under the conditions of 23 °C for 10 min, 52.5 °C for 10 min, and 80 °C for 10 min. Following these incubation steps, the cDNA synthesis reactions undergo RNA removal via RNaseH treatment and are further incubated at 37 °C for 20 minutes Fig. 5-3b.

qPCR

Total RNA is isolated using the Purelink RNA Mini Kit, and reverse transcription is performed using the SuperScript IV First-Strand Synthesis System following the manufacturer's instructions. The qPCR reaction is performed using primers (TCTCTTACTACCACTCACCC and TGGAGTGTATCAGTCAGCTC for c-Fos; CCACAGACCTTCCAGGAGAATG and GTGCAGTTCAGTGATCGTACAGG for IL-1b; and TTGTAGCCCTCTGTGTGCTCAAG and

reverse GCCTGACCAAGGAAAGCAAAGTC for GAPDH) with the SYBR Green PCR Master Mix on the QuantStudio 7 Flex Real-Time PCR instrument. The PCR cycling condition is denaturation at 90 °C for 1 min and 40 cycles of 56 °C for 15 s and 72 °C for 2 min. Fold changes in gene expression are calculated with C_T (cycle threshold) measurements according to the literature [204,205].

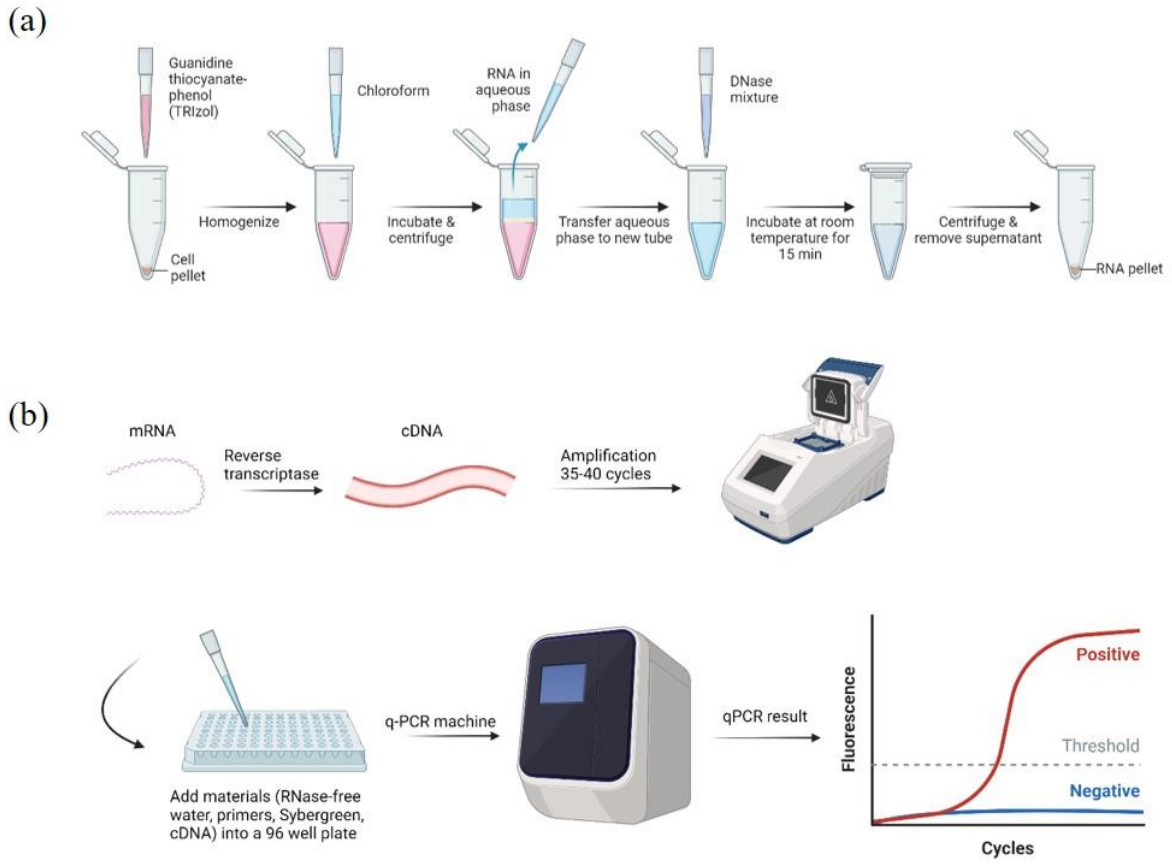

Figure 5-3: RT-qPCR test procedure. (a) mRNA extraction procedure on control and tested cell samples under various loading condition, (b) cDNA synthesis and qPCR testing.

5.3 Result and Discussion

5.3.1 Infiltration Behavior of LN Containing Cell Culture Medium

Under the quasi-static loading, the initial response of the LN is purely elastic as the system internal pressure is insufficient to overcome the energy barrier at the liquid and nanopore

interface (Fig. 5-4b). When the internal hydrostatic pressure reaches P_{in}, the liquid molecules start to infiltrate into the nanopores. As the liquid molecules continuously flow into the nanopores, a pressure-plateau is observed. The width of the pressure-plateau is defined as the total liquid infiltration volume, V_{in}. The measured value, 1.8 cm^3/g is close but smaller than the total porosity of the NpPs. Due to the extremely large porosity, these NpPs start to deform at extremely low pressure even before the liquid infiltration process [206]. When the system internal pressure reaches P_{in}, the liquid infiltration process of the LN is activated. As the liquid molecules flow into the nanopores at a faster rate than the deformation of the NpPs, the remaining nanopore volume is accessible for liquid flow and no further deformation of the NpPs is allowed [206].

Once the nanopores are fully filled by the liquid molecules, the system internal pressure increases again at the rate similar to the value of the initial elastic response of the LN. With the removal of the externally applied force, the internal hydrostatic pressure drops immediately and then gradually reduces to zero. The pressure associated with the unloading process is much lower than the loading one. The liquid molecules flow into the nanopores may or may not flow out from the nanopores during the unloading process [207–210]. The area enclosed in the loading-unloading curve of the LN (shaded area in Fig. 5-4b) represents the volumetric energy mitigation efficiency of the LN.

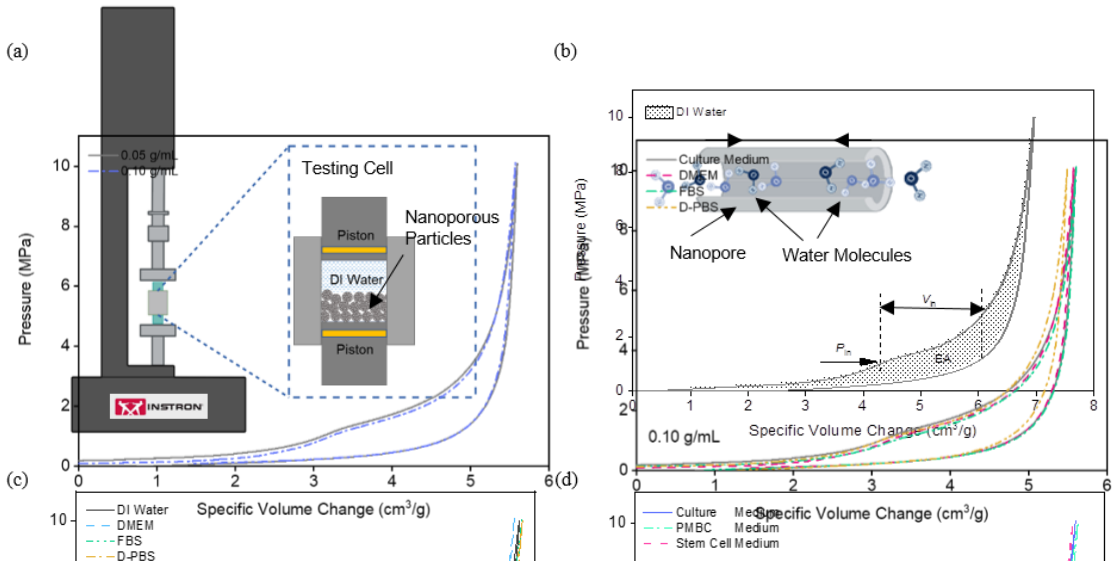

Figure 5-5: (a) Effects of varying concentration of cell culture medium on liquid infiltration. (b) Overlay of liquid infiltration curves of complete 293T cell culture media and its individual components.

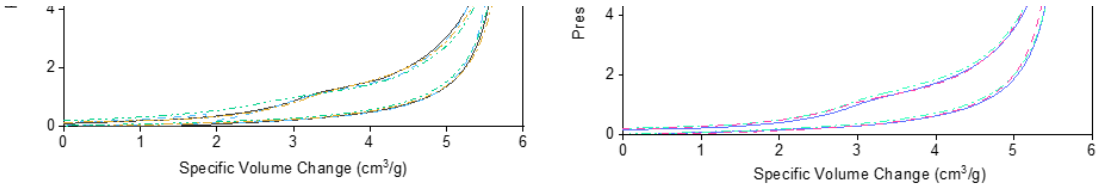

Figure 5-4: Liquid nanofoam schematic (a) and its typical infiltration behavior with DI water (b) and effect of cell culture medium on liquid infiltration, demonstrated by (c) 293T cell culture medium components, (d) complete 293T cell culture medium, PBMC medium and Stem cell medium.

It is necessary to validate that the fluid used in cell culture has no effect on the liquid infiltration so that the NpPs can be directly mixed with cells for future testing. Fig. 5-4c and d show that the infiltration behavior of LN is independent from the cell culture medium, PBMC and stem cell media, as both the P_{in} and V_{in} are constants. In addition, Fig. 5-5a and b further demonstrate that the infiltration behavior of the LN is independent from the ratio between the NpPs and liquid, and the liquid compositions. These results confirm that the surface tension of the cell culture media is similar to the value of DI water, which is ideal for cell growth and proliferation [211].

5.3.2 Biocompatbility of LN

To study the biocompatibility of LN, we cultured 293T cells with LN with different ratios between NpP and the cell culture medium (0, 0.03 g/mL, 0.05 g/mL and 0.1 g/mL). These particle to liquid ratios were chosen to match the LN samples used for the protection of cells and whole organs. We observed no adverse effect on cell viability with this range of NpP to liquid ratios during three days of culture (Fig. 5-6a). In addition, long-term culture of cells over nine days showed no reduction in viability with 0.05 g/mL NpP to liquid ratio. The specific NpP to liquid ratio was selected because this is the value used for all testing samples. These results verify that NpP exhibits low toxicity and excellent biocompatibility with human culture cells (Fig. 5-6b).

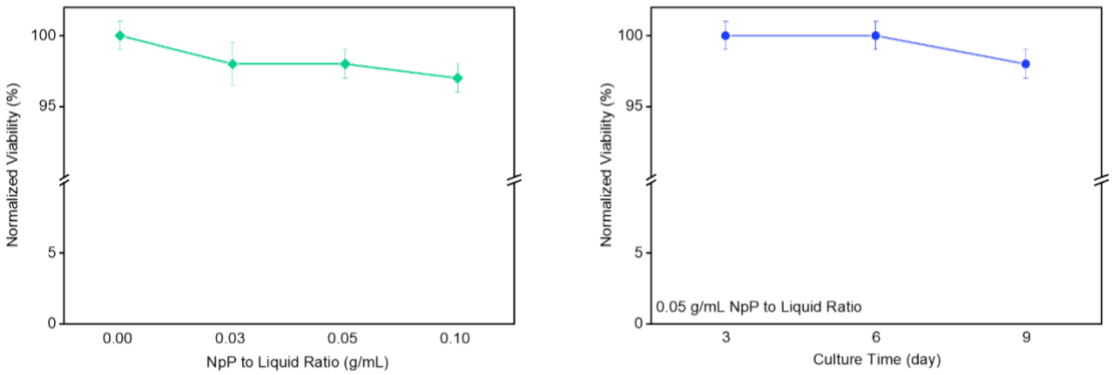

Figure 5-6: Biocompatibility of LN with living cells. (a) Cell viability upon addition of indicated concentrations of nanoporous particles (b) Cell viability with continued presence of nanoporous particles over nine days.

5.3.3 LN Protection of Cells under Low Energy Loading Condition

Before the internal system pressure reaches P_{in}, the energy mitigation mechanism, i.e. the liquid infiltration is not activated for the LN. Therefore, it is necessary to validate that at the onset of the liquid infiltration, cells are not damaged by the external loading. To that end, we have conducted a series of compression tests on LN and live cells under low energy loading. We

subjected 293T cells to 0.26 J over the sample area of 286 mm^2 in the presence or absence of NpPs. Post-compression, we observed cell morphology with confocal microscopy and found

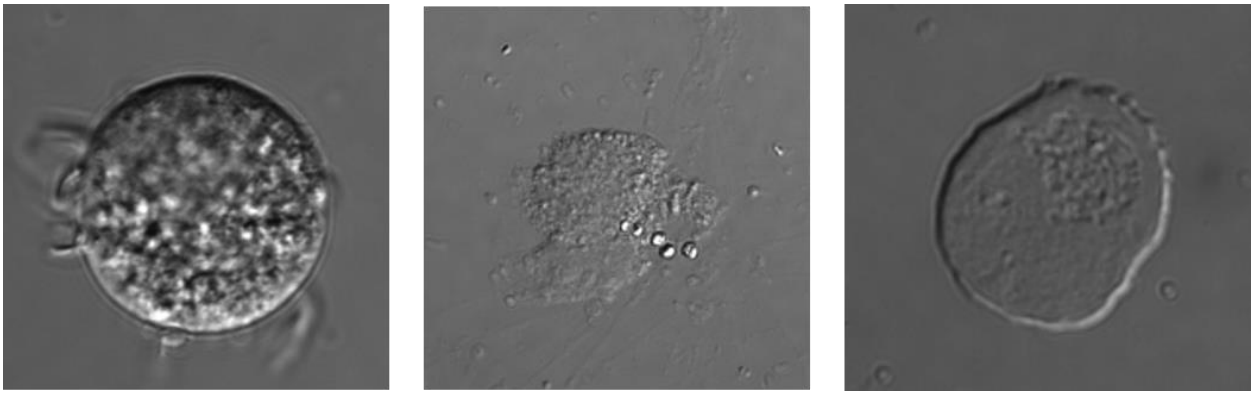

Figure 5-7: Protective effect of LN on living cells under low energy loading. Representative images of a live cell (left), a dead cell (middle) and a deformed cell (right) by confocal microscopy.

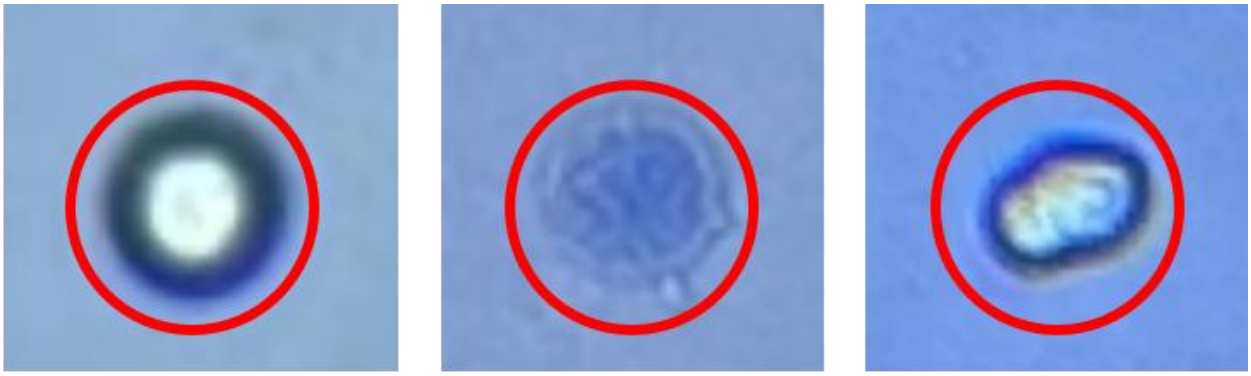

Figure 5-8: Representative images of trypan blue staining demonstrating live (left), dead (middle) and deformed (right) cells.

populations of live (round cells with intact membrane), dead (cell debris with ruptured membrane) and deformed (cells with changed shape in response to the external force) [212–216] cells when NpPs were absent (Fig. 5-7). These observations were confirmed with Trypan blue staining. (Fig. 5-8).

The addition of NpPs significantly increased cells that remained viable post compression from 74% to 100% (Fig. 5-9a). In addition, NpPs addition decreased the percentage of deformed cells by 505% (Fig. 5-9b). These results suggest that the LN acts as a buffer against cellular damage

induced by external energy, safeguarding cellular integrity and minimizing the risk of damage. However, the energy mitigation mechanism is not based on the nanoscale liquid flow as the lower energy loading cannot trigger liquid infiltration. This is due to the special physical properties of the NpPs used in this study. As shown in the liquid infiltration test, 10% of the nanopores are crushed at extremely low pressure to dissipate energy. Although this mechanism is somewhat

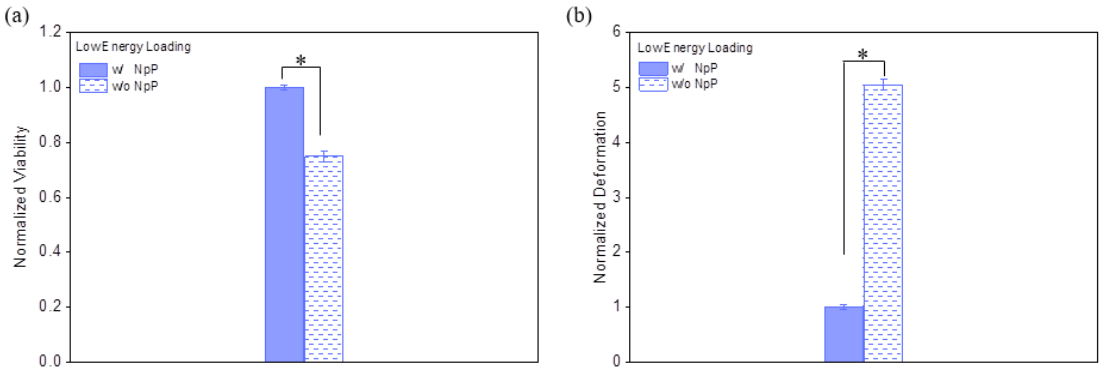

Figure 5-9: Protective effect of LN on living cells under low energy loading. (a) Quantification of cell viability with or without nanoporous particles. (b) Quantification of cell deformation with or without nanoporous particles. *, P <0.05, Student's t-test.

similar to conventional foams, a solid-based foam does not exhibit additional energy mitigation capacity for higher energy loadings as the energy mitigation capacity is predetermined by the low working pressure of the solid-based foam. In next section, the high energy mitigation capacity of the LN based on the unique liquid infiltration mechanism will be demonstrated.

In addition to changes in gross-morphology and cell viability, external force may cause gene expression changes. To test this possibility, we measured the expression levels of the stress response genes c-Fos. An archetype of cellular immediate-early genes, c-Fos is known to a marker for cell response to external stress and can couple short-term signals elicited by extracellular stimuli to long-term changes in cellular phenotype by orchestrating alterations in target gene expression [217–220]. Consistent with the function of c-Fos as a stress response gene, energy loading

significantly increased its expression levels in living cells. Notably, the presence of NpPs in the LN system reduced the upregulation of c-Fos by 72% (Fig. 5-10a).

Given that blunt force trauma is associated with a pro-inflammatory state relevant for its long-term high comorbidity, we also measured the expression levels of IL-1b, a potent cytokine that induces inflammation [221–223]. Energy loading upregulated the expression levels of IL-1b, which

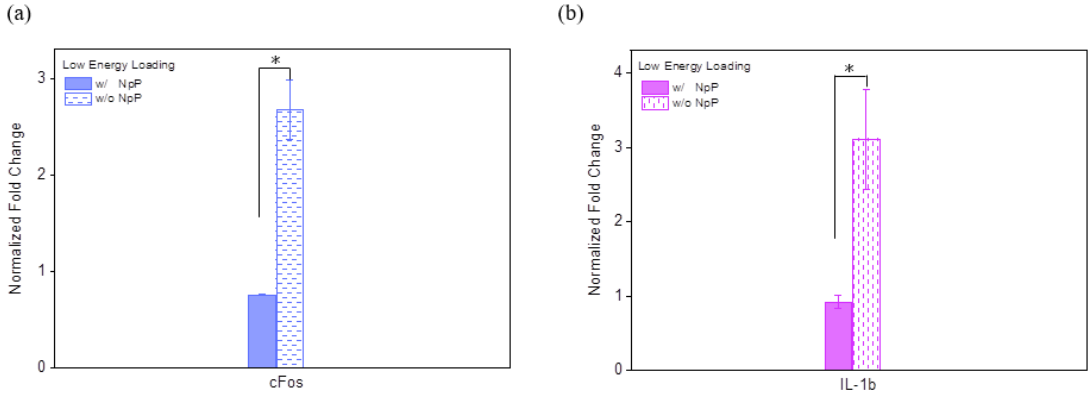

Figure 5-10: Regulatory effect of LN on stress gene expression in living cells under low energy loading. Relative expression levels of (a) c-FOS, (b) IL-1b. *, P <0.05, Student's t-test.

again was effectively attenuated by the LN system by 70% (Fig. 5-10b). Collectively, these results suggest that low energy loading leads to stress and inflammatory responses that can be mitigated by LN.

5.3.4 LN Protection of Cells under High Energy Loading Condition

The high energy loading is set to 0.78 J over the sample area of 286 mm^2. This is the total energy needed to complete the liquid infiltration process of the selected LN, which is calculated based on the testing curves shown in Fig.5-4. Under high energy loading, we observed a significant protective effect of LN on 293T cells, in terms of both viability and deformability (Fig. 5-11). With the additional NpPs, the cell viability under high energy loading was about 100%, while without the NpPs, the cell viability was only 67%. In addition, NpPs addition decreased the percentage of deformed cells by 1041%. Furthermore, LN protected cells from upregulation of

stress and pro-inflammatory genes (Fig. 5-12) The presence of NpPs reduced the upregulation of c-Fos and IL-1b by 82% and 89%, respectively. These results demonstrate that the nanoscale liquid flow of LN can significantly reduce cellular damage under high energy impacts.

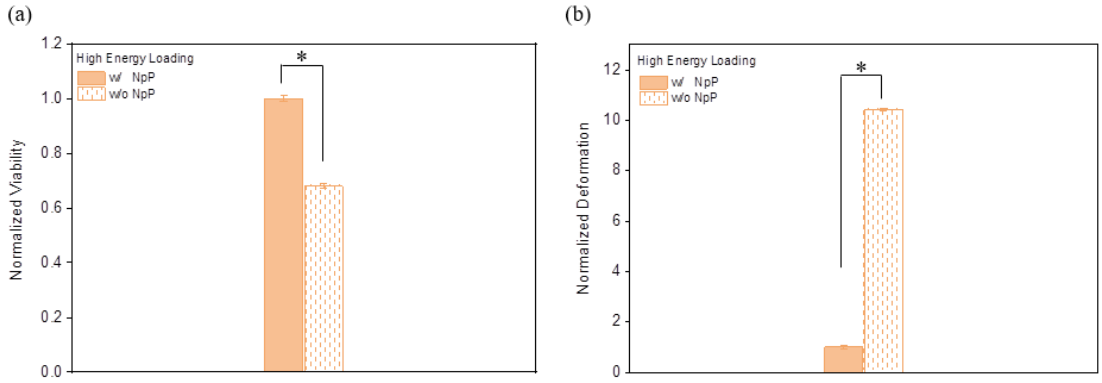

Figure 5-11: Protective effect of LN on living cells under high energy loading. (a) Quantification of cell viability with or without nanoporous particles. (b) Quantification of cell deformation with or without nanoporous particles. *, P <0.05, Student's t-test.

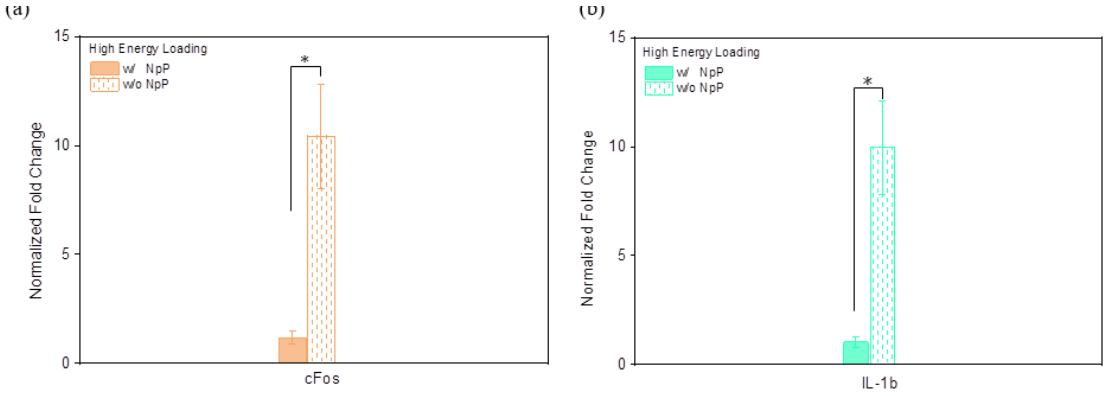

Figure 5-12: Regulatory effect of LN on stress gene expression in living cells under high energy loading. Relative expression levels of (a) c-FOS, (b) IL-1b *, P <0.05, Student's t-test.

When the external input energy is increased from 0.26 J (low energy loading) to 0.78 J (high energy loading), cells under direct compression without the protection of LN shows a reduced cell viability and much increased deformed cells, and stress and inflammation gene expressions. Together with the addition of the NpPs, the cell culture medium is converted into the LN system, which effectively mitigate the cell damage at both low and high energy loading conditions. More importantly, the LN significantly reduced the upregulation of c-Fos and IL-1b, which may induce

cancers [224] such as osteosarcoma and endometrial carcinoma, depression [225], autoimmune diseases [226] such as such as arthritis, thyroid disease, and septic shock, and autoinflammatory syndromes [227,228] including Cryopyrin-Associated Periodic Syndromes (CAPS) and intestinal dysbiosis.

5.3.5 LN Protection of Whole Organs under Compression

Given the protective effect of LN on cultured cells, we further tested whether LN protects whole animal organs from mechanical loading. LN composed of 0.25 g NpPs and 1.5 mL 39% LiCl aqueous solution was sealed in a TPU pouch with a diameter of 25.4 mm and a thickness of 6.4 mm (Fig. 5-13). The sealing strength is much higher than the loading conditions used for all experiments. No pouch burst was observed in all experiments. The sealed LN pouch was then stacked with the organ specimen for quasi-static compression tests. A total external energy of 1.74 J was applied over the area of 506 mm^2. The energy level was increased because of the larger sample aera and the increased amount of NpPs in the pouch. As the LN is not in direct contact with the biotissues, the liquid phase was changed to electrolyte solutions. This makes the LN has wider working temperature range to satisfy the temperature requirements of protective

devices such as football helmets. The liquid infiltration behavior of the LN pouch is similar to the LN containing DI water (Fig. 5-14).

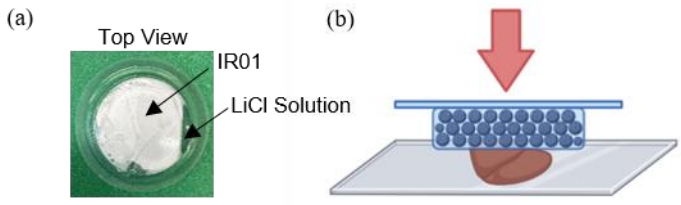

Figure 5-13: Schematic of organ compression tests. (a) A TPU pouch containing LN, and (b) Schematic of quasi-static compression test conducted on a mouse organ.

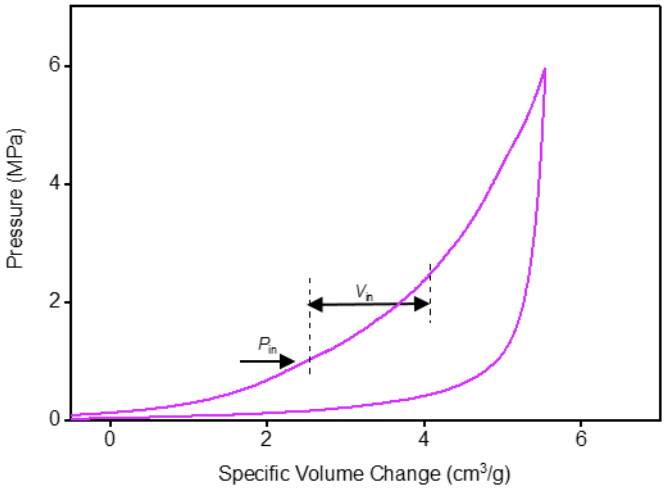

Figure 5-14: Typical quasi-static compression curves of a LN pouch.

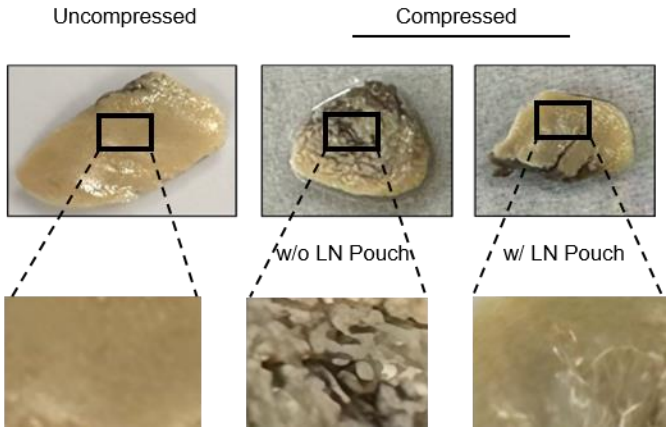

Figure 5-15: Protective effect of LN on whole liver by light microscopy. Representative images of mouse liver under uncompressed (left) and compressed (right) conditions, with or without LN pouch.

Similar to the scenario in BFT, mechanical loading caused numerous cracks on the mouse liver. Strikingly, the thin LN pouch almost completely protected mouse liver from tearing (Fig. 5-15). This finding was further supported by H&E staining of liver (Fig. 5-16). The total area of the cracks is quantified by a specific image processing method as detailed in Fig. 5-17. The compressed liver sample without the LN pouch shows a 33% of crack area, while the additional LN pouch limits the crack area to 1% only. Therefore, the LN pouch reduces the structural damage of the liver by 97%.

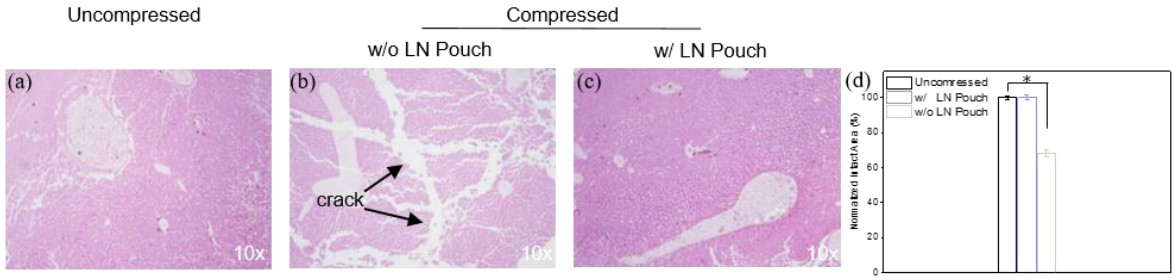

Figure 5-16: Protective effect of LN on whole liver by H&E staining, 10x magnification. Representative images of H&E staining of mouse liver under uncompressed (a) and compressed (b and c) conditions, with or without LN pouch, with arrows pointing to cracked areas under compression. (d) Quantification of intact areas of mouse liver under the indicated conditions. *, $P < 0.05$, Student's t-test.

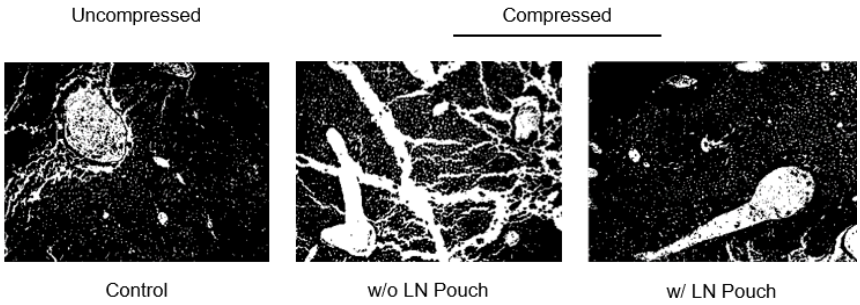

Figure 5-17: Image J results of representative images of mouse liver under uncompressed (left) and compressed (right conditions, with or without LN pouch.

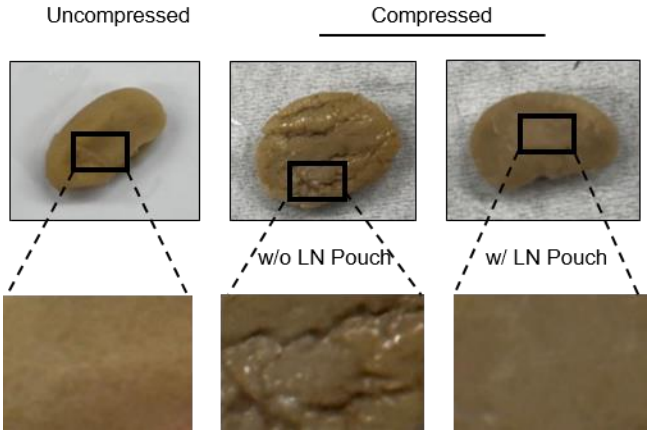

Figure 5-18: Protective effect of LN on whole kidney by light microscopy. Representative images of mouse kidney under uncompressed (left) and compressed (right) conditions, with or without LN pouch.

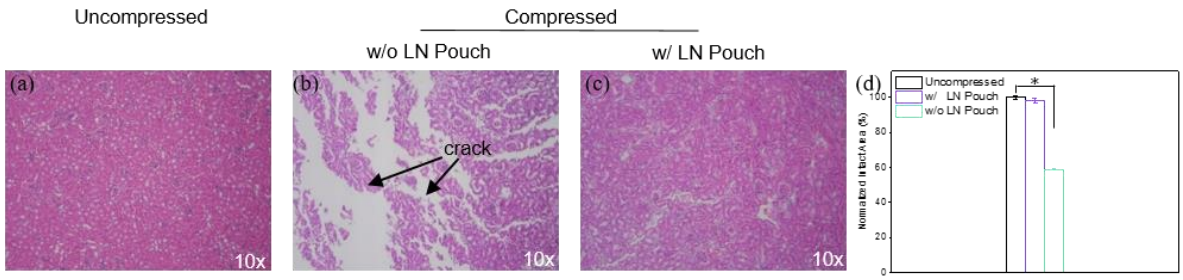

Figure 5-19: Protective effect of LN on whole kidney by H&E staining, 10x magnification. Representative images of H&E staining of mouse kidney under uncompressed (a) and compressed (b and c) conditions, with or without LN pouch, with arrows pointing to cracked areas under compression. (d) Quantification of intact areas of mouse liver under the indicated conditions. *, $P < 0.05$, Student's t-test.

We performed the same loading test on additional organs implicated in severe BFT, including whole kidney, heart and lung samples. As shown in Figs. 5-18, 19 and 20, the compressed kidney sample without the LN pouch shows a 41% of crack area, while the additional LN pouch limits

the crack area to 2% only. Therefore, the LN pouch reduces the structural damage of the kidney by 95%.

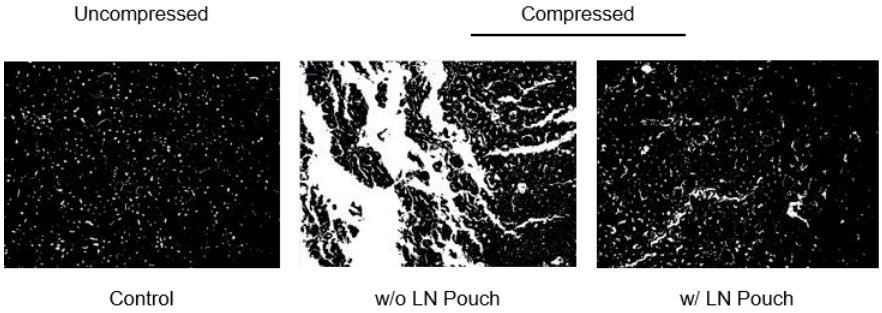

Figure 5-20: Image J results of representative images of mouse kidney under uncompressed (left) and compressed (right conditions, with or without LN pouch.

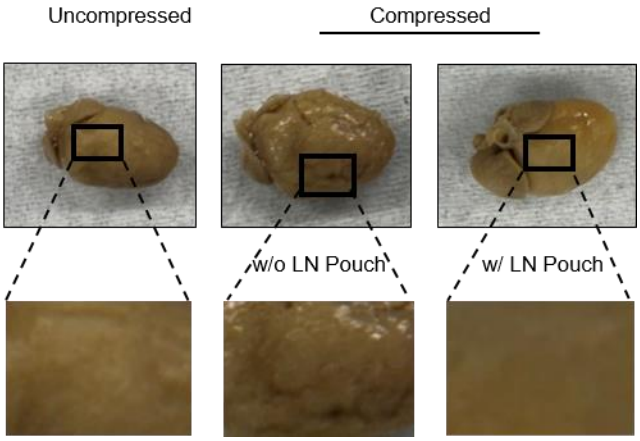

Figure 5-21: Protective effect of LN on whole heart by light microscopy. Representative images of mouse heart under uncompressed (left) and compressed (right) conditions, with or without LN pouch.

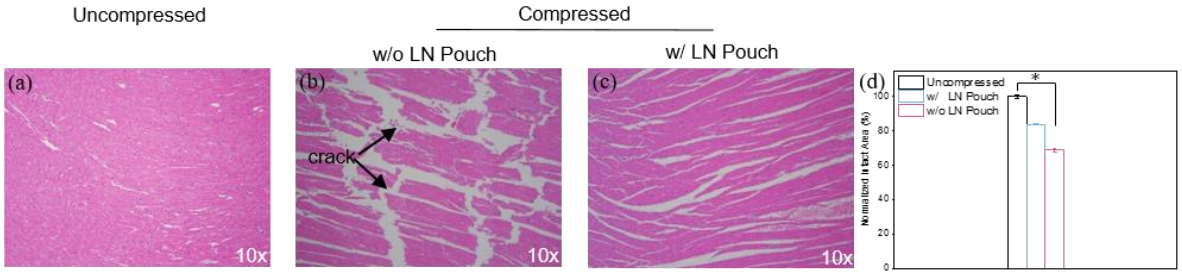

Figure 5-22: Protective effect of LN on whole heart by H&E staining, 10x magnification. Representative images of H&E staining of mouse heart under uncompressed (a) and compressed (b and c) conditions, with or without LN pouch, with arrows pointing to cracked areas under compression. (d) Quantification of intact areas of mouse liver under the indicated conditions. *, $P < 0.05$, Student's t-test.

As shown in Figs. 21, 22 and 23, the compressed heart sample without the LN pouch shows a 31% of crack area, while the additional LN pouch decreased the crack area to 16%. Therefore, the LN pouch reduces the structural damage of the heart by 48%.

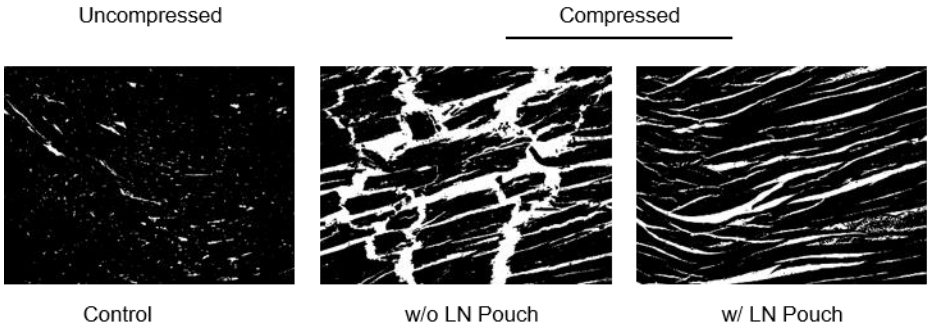

Figure 5-23: Image J results of representative images of mouse heart under uncompressed (left) and compressed (right conditions, with or without LN pouch.

As shown in Figs. 24, 25 and 26, the compressed lung sample without the LN pouch shows a 28% of crack area, while the additional LN pouch limits the crack area to 1% only. Therefore, the LN pouch reduces the structural damage of the lung by 96%.

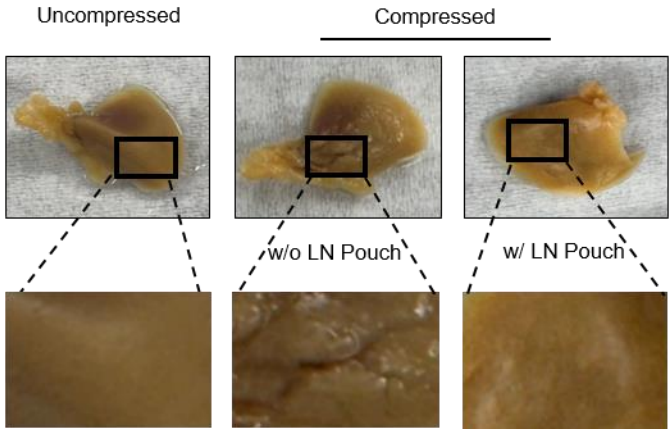

Figure 5-24: Protective effect of LN on whole lung by light microscopy. Representative images of mouse lung under uncompressed (left) and compressed (right) conditions, with or without LN pouch.

As shown in the above testing results, the biotissues protected by the LN pouch exhibit resilience and maintain normal shapes under mechanical compression. The external energy triggered liquid infiltration mechanism of the LN efficiently mitigates the input mechanical energy. In addition, during the entire compression process, the LN pouch maintains complete contact with

the biotissue samples, which avoids local stress concentration and damage of the biotissues. Therefore, LN can effectively protect vital organs from blunt force-caused damage.

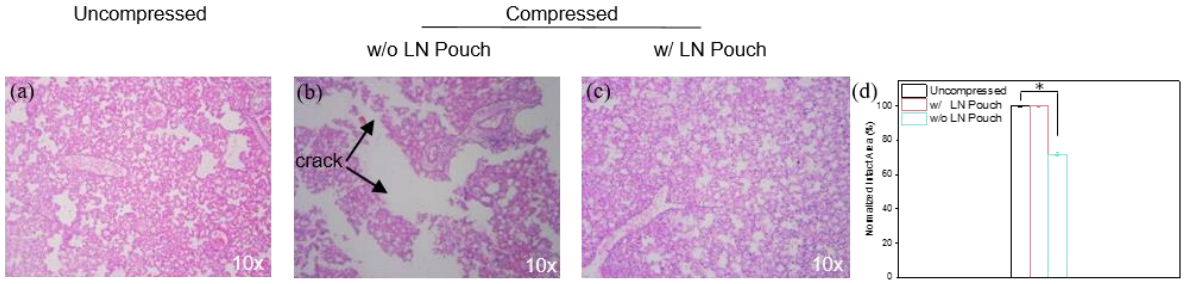

Figure 5-25: Protective effect of LN on whole lung by H&E staining, 10x magnification. Representative images of H&E staining of mouse lung under uncompressed (a) and compressed (b and c) conditions, with or without LN pouch, with arrows pointing to cracked areas under compression. (d) Quantification of intact areas of mouse liver under the indicated conditions. *, $P < 0.05$, Student's t-test.

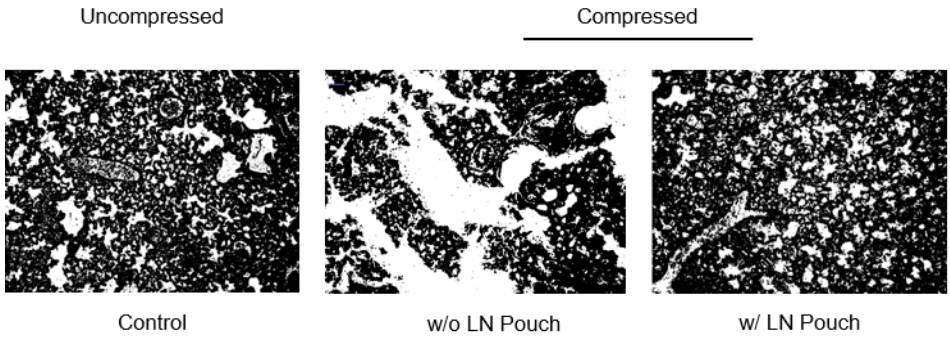

Figure 5-26: Image J results of representative images of mouse lung under uncompressed (left) and compressed (right conditions, with or without LN pouch.

5.4 Conclusion

As the current personal protective devices cannot effectively prevent blunt force trauma, new energy mitigation mechanism is desired to enhance the performance of future material systems. The performance of current energy absorption materials is limited by the energy mitigation efficiency as well as the dissimilar mechanical properties with the biological systems.

To address the above issues, we have developed the liquid nanofoam based on the nanoscale liquid flow energy mitigation mechanism. This new mechanism enables the high energy mitigation

efficiency of the LN. In addition, the fluid-like nature of the LN ensures the integrity of the interface between the LN layer and the protected biotissues, which engages all the NpPs for the energy mitigation process.

In this study, cell culture media are used as the liquid phase of the LN. The resulted LN has extraordinary biocompatibility and is directly mixed with human cells to evaluate its energy mitigation effectiveness. This experimental approach has never been adopted as most of other energy absorption materials are not biocompatible. The performance evaluation is limited to the characterization of their mechanical properties. By using this biological characterization method, we have demonstrated the potential of the LN system as a new energy absorbing material for BFT prevention by showing the following characteristics:

Biocompatibility. LN exhibits excellent biocompatibility, maintaining high cell viability with minimal cytotoxicity and negligible adverse effects on gene expression.

Protection of live cells from loading-induced damage on both the cellular and molecular levels. Without LN, external loading causes cell deformation and death. In addition, these mechanical stimuli upregulate stress response and proinflammatory genes mediating trauma and its co-morbidities. LN can effectively protect cells from these loading-induced damages.

Protection of whole organs against force-induced structural alterations. From a range of vital organs commonly damaged in blunt-force trauma, LN acts as effective shields during compression, significantly reducing tissue damage and preserving tissue integrity compared to uncompressed or non-LN protected organs.

In summary, this study highlights LN's versatility and compatibility for biomedical applications such as the prevention of blunt force trauma. Given its distinct capability to protect

cells and biotissues against mechanical stress, the LN could offer a novel solution to meet the critical needs for effective personal protection devices.

Chapter 6 Conclusions and Future Work

The research delineated in this dissertation has yielded substantial insights into the intricate nuances governing the quasi-static behavior of LN systems, as well as the efficacy exhibited by LN-functionalized materials and structures. These pioneering findings not only deepen our comprehension of fundamental principles but also pave the way for transformative advancements in diverse fields. By unraveling the underlying mechanisms and intricacies, this research sets a solid foundation for future explorations and innovations aimed at harnessing the potential of LN and its applications in various technological domains.

6.1 Contributions

Based on the results in this dissertation, the following conclusions can be drawn:

Strong interaction between compressible fluids and other energy absorption materials and structures. Integration of SHGM into thin-walled tubes has substantially enhanced the average post-buckling strength of the tube under both quasi-static and dynamic conditions. This is attributed to the strong interaction between SHGM and the tube wall. Notably, SHGM exhibits the highest strengthening coefficient among all fillers due to the superior “bonding strength” between SHGM and the tube wall.

Structural imperfection inert performance. The LN filler of thin-walled tubes demonstrates remarkable effectiveness in alleviating the detrimental impacts caused by structural imperfections under quasi-static conditions. The filler induces a notable shift in the folding dynamics of the tube during compression, transitioning from inward to outward folding patterns. It is the strong interaction between the LN filler and the tube wall alters the folding behavior, and thus mitigates the growth of dents and localized folding

Efficient safeguarding for biotissues. LN exhibits excellent biocompatibility, which allows them to directly interact with cells without any harmful effects. Both cell viability testing and qPCR results have demonstrated that LN can effectively protect both cells and organs from mechanical abuse. This suggests LN is a promising energy absorption fluid for the prevention of blunt force trauma.

6.2 Future Work

In other circumstances such as blast waves, the compressible fluids may undergo dynamic deformation at significantly higher strain rates. Consequently, it is necessary to investigate the dynamic performance of the compressible fluids and their interaction with structures by utilizing the Split Hopkinson Pressure Bar (SHPB) apparatus [229–235].

As shown in Fig. 6-1, the SHPB system includes the striker, incident and transmission bars. The striker bar has a diameter of 0.625 inches and a length of 2 feet. Both the incident and transmission bars have the diameter of 0.75 inches and the length of 6 feet. The testing specimens are sandwiched in between the incident and transmission bars. Once the striker is launched and hit the incident bar, a stress wave propagates through the incident bar, the specimen, and then the transmission bar. A pair of photomicrosensors (EE-SPW321/421#, Omron) are configured to measure the velocity of the striker bar. Two strain gauges (WK-06-250BF-10C, Micro-Measurement Inc.) are affixed to the mid-span of the incident and transmission bars to capture the strain waves. The measured electrical signal is filtered and

amplified by signal conditioner (2310B, Micro Measurements) and then recorded by a digitizer (Model No. NI-9215, National Instrument).

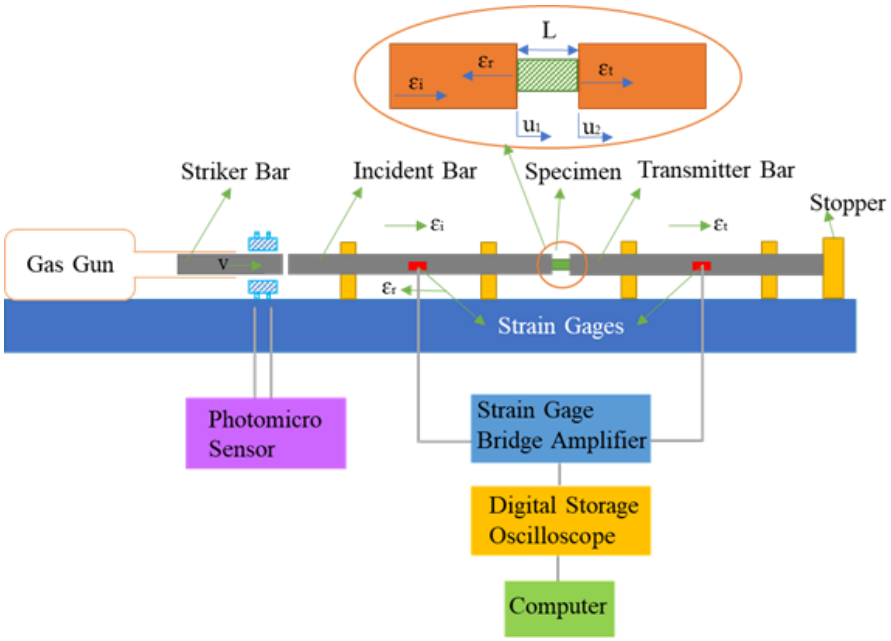

Figure 6-1: Schematic of a typical Split Hopkinson Pressure Bar system.

When the incident stress wave, ε_i reaches the front surface of the sample, part of the wave reflects back as a reflected wave ε_R, the remaining part continues to travel to the transmission bar defined as the transmitted wave, ε_T. From the incident, reflected and transmitted waves detected by the strain gauges, the engineering stress and strain, and the strain rate, experienced by the specimen can be derived as follows.

$$\sigma(t) = \frac{A_B}{A_S} E_B \varepsilon_T(t) \qquad (6-1)$$

$$\varepsilon(t) = \int_o^t \dot{\varepsilon}(\tau) d\tau \qquad (6-2)$$

$$\dot{\varepsilon}(t) = \frac{2C_B}{L_S} \varepsilon_R(t) \qquad (6-3)$$

Where A_B is the cross-sectional area of the bars, E_B is Young's modulus of the bar material, C_B is the 1D elastic longitudinal wave speed in the bars, ($C_B = \sqrt{E_B/\rho_B}$, where ρ_B is the density of the bar material), and A_S and L_S are the initial cross-sectional area and length of the specimen, respectively.

To investigate the dynamic response of compressible fluids, testing samples are placed within the loading cell, which is positioned between the incident and transmission bars. As the fluids have much lower modulus in comparison to that of the bar material, a pulse shaper is needed to achieve the stress equilibrium (Fig. 6-2). Currently, a brass disc with diameter of 8.0 mm and thickness of 0.80 mm is placed at the front surface of the incident bar to modify the incident pulse. This SHPB system will be adopted to quantify the energy absorption performance of the compressible fluids in the future.

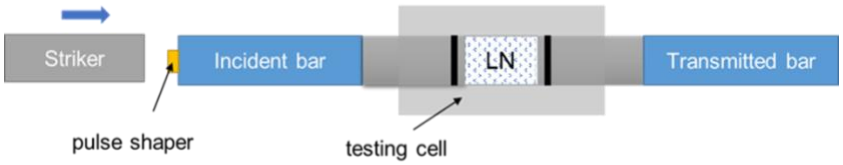

Figure 6-2: Modified Split Hopkinson Pressure Bar system for the characterization of compressible fluid

BIBLIOGRAPHY

1 Z. Fan, G. Lu and K. Liu, *Eng Struct*, 2013, **55**, 80–89.

2 Z. Tang, S. Liu and Z. Zhang, *Thin-Walled Structures*, 2012, **51**, 112–120.

3 W. Liu, Z. Lin, N. Wang and X. Deng, *Thin-Walled Structures*, 2016, **100**, 25–37.

4 G. Sun, D. Chen, X. Huo, G. Zheng and Q. Li, *Compos Struct*, 2018, **184**, 110–124.

5 F. Zhu, G. Lu, D. Ruan and Z. Wang, *International Journal of Protective Structures*, 2010, **1**, 507–541.

6 J. Liu, B. Zheng, K. Zhang, B. Yang and X. Yu, *Int J Impact Eng*, 2019, **126**, 160–171.

7 G. Tiwari, M. A. Iqbal and P. K. Gupta, *Thin-Walled Structures*, 2018, **126**, 246–257.

8 C. J. Shen, G. Lu and T. X. Yu, *Compos Struct*, 2013, **98**, 282–293.

9 D. Ruan, G. Lu, B. Wang and T. X. Yu, *Int J Impact Eng*, 2003, **28**, 161–182.

10 M. A. Yahaya, D. Ruan, G. Lu and M. S. Dargusch, *Int J Impact Eng*, 2015, **75**, 100–109.

11 J. Shen, G. Lu and D. Ruan, *Compos B Eng*, 2010, **41**, 678–685.

12 D. Ruan, G. Lu, F. L. Chen and E. Siores, *Compos Struct*, 2002, **57**, 331–336.

13 G. Lu, J. Shen, W. Hou, D. Ruan and L. S. Ong, *Int J Mech Sci*, 2008, **50**, 932–943.

14 D. RUAN, G. LU, L. ONG and B. WANG, *Compos Sci Technol*, 2007, **67**, 1218–1234.

15 N. S. Ha and G. Lu, *Compos B Eng*, 2020, **181**, 107496.

16 J. J. Knapik, B. L. Hoedebecke, G. G. Rogers, M. A. Sharp and S. W. Marshall, *Sports Medicine*, 2019, **49**, 1217–1232.

17 G. Lu and T. Yu, *Energy absorption of structures and materials*, Woodhead Publishing Limited, 2003.

18 S. Meng, P. Ivarsson and N. Lubbe, *Accid Anal Prev*, , DOI:10.1016/j.aap.2023.107181.

19 G. DiGiacomo, S. Tsai and M. Bottlang, *Ann Biomed Eng*, 2021, **49**, 2805–2813.

20 T. J. Dickson and F. A. Terwiel, *J Sci Med Sport*, 2021, **24**, 1004–1009.

21 E. D. Porter, S. W. Trooboff, M. G. Haff, J. C. Cooros, A. B. Wolffing, A. Briggs, K. K. Rhynhart and A. O. Crockett, in *Journal of Trauma and Acute Care Surgery*, Lippincott Williams and Wilkins, 2019, vol. 87, pp. 1205–1213.

22 P. Care and I. Data, *NFL.com*, 2020, 2019–2022.

23 P. Care, 2023, 3–4.

24 NSC, *National Safety Council (NSC)*, 2023, 1–5.

25 M. A. Kader, M. A. Islam, M. Saadatfar, P. J. Hazell, A. D. Brown, S. Ahmed and J. P. Escobedo, *Mater Des*, 2017, **118**, 11–21.

26 Y. Fei, F. Chen, W. Fang, L. Xu, S. Ruan, X. Liu, M. Zhong and T. Kuang, *Compos B Eng*, 2020, **199**, 108279.

27 F. Hassanpour Roudbeneh, G. Liaghat, H. Sabouri and H. Hadavinia, *Mechanics of Advanced Materials and Structures*, 2020, **27**, 1803–1815.

28 R. Huang, S. Ma, M. Zhang, J. Xu and Z. Wang, *Materials Science and Engineering: A*, 2019, **756**, 302–311.

29 C. Zhan, M. Li, R. McCoy, L. Zhao and W. Lu, *Compos Struct*, 2022, **290**, 115550.

30 L. Cui, S. Kiernan and M. D. Gilchrist, *Materials Science and Engineering A*, 2009, **507**, 215–225.

31 S. He, Y. Lv, S. Chen, G. Dai, J. Liu and M. Huo, *Materials Science and Engineering: A*, 2020, **772**, 138658.

32 X. Xiang, S. Zou, N. S. Ha, G. Lu and I. Kong, *Compos B Eng*, 2020, **198**, 108216.

33 M. Zou, S. Xu, C. Wei, H. Wang and Z. Liu, *Thin-Walled Structures*, 2016, **101**, 222–230.

34 J. Fu, Q. Liu, K. Liufu, Y. Deng, J. Fang and Q. Li, *Thin-Walled Structures*, 2019, **135**, 400–413.

35 P. Wang, F. Yang, P. Li, W. Zhang, G. Lu and H. Fan, *Int J Mech Sci*, 2023, **244**, 108081.

36 N. S. Ha and G. Lu, *Compos B Eng*, 2020, **181**, 107496.

37 P. Wang, F. Yang, P. Li, W. Zhang, G. Lu and H. Fan, *Int J Mech Sci*, 2023, **244**, 108081.

38 M. Zou, S. Xu, C. Wei, H. Wang and Z. Liu, *Thin-Walled Structures*, 2016, **101**, 222–230.

39 A. G. Mamalis, G. L. Viegelahn, D. E. Manolakos and W. Johnson, *Int J Impact Eng*, 1986, **4**, 117–126.

40 T. Ghanbari Ghazijahani, H. Jiao and D. Holloway, *Thin-Walled Structures*, 2014, **80**, 13–21.

41 T. Ghanbari Ghazijahani, H. Jiao and D. Holloway, *Thin-Walled Structures*, 2015, **92**, 48–54.

42 AMAZIGO JC and BIDIANSKY B, *ASME Pap*, 1971, 179–184.

43 W. Guggenberger, *Thin-Walled Structures*, 1995, **23**, 351–366.

44 A. Khamlichi, M. Bezzazi and A. Limam, *Thin-Walled Structures*, 2004, **42**, 1035–1047.

45 M. Kajtaz and A. Subic, *International Conference on Mechanics, Materials*, 2015, 62–74.

46 S. Sărăndan, R. Negru, L. Marşavina, M. S. Mihuţa and D.-A. Şerban, *Mater Today Proc*, , DOI:10.1016/j.matpr.2022.11.500.

47 B. J. Ramirez, U. Misra and V. Gupta, *Mechanics of Materials*, 2018, **127**, 39–47.

48 X. Di, J. Li, M. Yang, Q. Zhao, G. Wu and P. Sun, *J Mater Chem A Mater*, 2021, **9**, 20703–20713.

49 M. Ganly and J. M. McMahon, *BMJ Open Sport Exerc Med*, 2018, **4**, e000464.

50 B. W. Benson, G. M. Hamilton, W. H. Meeuwisse, P. McCrory and J. Dvorak, *Br J Sports Med*, , DOI:10.1136/bjsm.2009.058271.

51 C. Hrysomallis, *J Sci Med Sport*, 2004, **7**, 156–164.

52 S. Sa˘ra˘ndan, R. Negru, L. Marşavina, M. S. Mihuţa and D. A. Şerban, *Mater Today Proc*, , DOI:10.1016/j.matpr.2022.11.500.

53 M. Al Ayyan, T. Aziz, A. El Sherif and O. Bekdache, *Ulus Travma Acil Cerrahi Derg*, 2015, **21**, 527–30.

54 T. A. Schaedler and W. B. Carter, *Annu Rev Mater Res*, 2016, 46, 187–210.

55 N. S. Ha and G. Lu, *Compos B Eng*, 2020, 181.

56 L. Cannon, *J R Army Med Corps*, 2001, **147**, 87–96.

57 Z. Benzait and L. Trabzon, *J Compos Mater*, 2018, **52**, 3241–3263.

58 P. Singh Deora, M. Khurana, Priya, R. Avtar Muhal, D. Upadhyay and C. Goswami, *Mater Today Proc*, 2022, **60**, 2230–2235.

59 P. Liu and M. S. Strano, *Adv Funct Mater*, 2016, **26**, 943–954.

60 A. Baroutaji, M. Sajjia and A. G. Olabi, *Thin-Walled Structures*, 2017, **118**, 137–163.

61 M. Langseth, O. S. Hopperstad and A. G. Hanssen, *Thin-Walled Structures*, 1998, **32**, 127–150.

62 K. Fall and K. Varadhan, *J Appl Mech*, 1983, **50**, 179–191.

63 K. R. F. Andrews, G. L. England and E. Ghani, *Int J Mech Sci*, 1983, **25**, 687–696.

64 S. R. Guillow, G. Lu and R. H. Grzebieta, *Int J Mech Sci*, 2001, **43**, 2103–2123.

65 N. S. Ha and G. Lu, *Thin-Walled Structures*, 2020, **157**, 106995.

66 A. Baroutaji, M. Sajjia and A. G. Olabi, *Thin-Walled Structures*, 2017, **118**, 137–163.

67 H. Liu, Z. X. C. Chng, G. Wang and B. F. Ng, *Int J Mech Sci*, 2021, **210**, 106731.

68 N. S. Ha, T. M. Pham, H. Hao and G. Lu, *Int J Mech Sci*, 2021, **201**, 106464.

69 J. Chen, E. Li, Q. Li, S. Hou and X. Han, *Compos Struct*, 2022, **283**, 115109.

70 M. A. Kader, M. A. Islam, M. Saadatfar, P. J. Hazell, A. D. Brown, S. Ahmed and J. P. Escobedo, *Mater Des*, 2017, **118**, 11–21.

71 F. Hassanpour Roudbeneh, G. Liaghat, H. Sabouri and H. Hadavinia, *Mechanics of Advanced Materials and Structures*, 2020, **27**, 1803–1815.

72 A. Baykasoğlu, C. Baykasoğlu and E. Cetin, *Thin-Walled Structures*, , DOI:10.1016/j.tws.2020.106630.

73 E. Cetin and C. Baykasoğlu, *Int J Mech Sci*, 2019, **157–158**, 471–484.

74 Z. Wang and J. Liu, *Compos B Eng*, 2019, **165**, 626–635.

75 L. Yan, K. Zhu, N. Chen, X. Zheng and M. Quaresimin, *Compos Struct*, 2021, **255**, 112946.

76 M. Li and W. Lu, *Physical Chemistry Chemical Physics*, 2017, **19**, 17167–17172.

77 Y. Zhang, M. Li, Y. Gao, B. Xu and W. Lu, *Nanoscale*, 2018, **10**, 18444–18450.

78 M. Li and W. Lu, *Physical Chemistry Chemical Physics*, 2017, **19**, 17167–17172.

79 M. Li, J. Li, S. Barbat, R. Baccouche and W. Lu, *Compos Struct*, 2018, **200**, 120–126.

80 M. N. Garaga, M. Persson, N. Yaghini and A. Martinelli, *Soft Matter*, 2016, **12**, 2583–2592.

81 S.-J. Lee, G.-M. Kim and C.-L. Kim, *Polym Test*, 2023, **117**, 107855.

82 J. Kim, J. Kim, J. Ahn and J. Lee, *J Appl Polym Sci*, 2021, **138**, 50060.

83 B. Yuan, C. Zhao, X. Sun and J. Liu, *Adv Funct Mater*, 2020, **30**, 1910709.

84 X. Nie, Y. Yoo, H. Hewakuruppu, J. Sullivan, A. Krishna and J. Lee, *Sci Rep*, 2020, **10**, 6661.

85 X. Yu, F. Yao, W. Huang, D. Xu and C. Chen, *Renew Energy*, 2022, **194**, 129–136.

86 Y. Sun, H. He, X. Huang and Z. Guo, *ACS Appl Mater Interfaces*, 2023, **15**, 4799–4813.

87 J. F. Peters, M. Muthuswamy, J. Wibowo and A. Tordesillas, *Phys Rev E Stat Nonlin Soft Matter Phys*, 2005, **72**, 1–8.

88 T. V. Garza-Cruz and M. Nakagawa, *Granul Matter*, 2012, **14**, 309–318.

89 J. Atkinson, in *Encyclopedia of Geology*, Elsevier, 2005, vol. c, pp. 184–193.

90 G. Lu and T. Yu, *Energy Absorption of Structures and Materials*, 2003.

91 X. Yang, T. An, Z. Wu, T. Zou, H. Song, J. Sha, C. He and N. Zhao, *Compos Struct*, 2020, **245**, 112357.

92 A. Baroutaji, M. Sajjia and A. G. Olabi, *Thin-Walled Structures*, 2017, **118**, 137–163.

93 I. Duarte, L. Krstulović-Opara and M. Vesenjak, *Compos Struct*, 2018, **192**, 184–192.

94 M. Su, H. Wang and H. Hao, *Compos Struct*, 2019, **226**, 111197.

95 J. Fang, Y. Gao, X. An, G. Sun, J. Chen and Q. Li, *Compos B Eng*, 2016, **92**, 338–349.

96 N. Movahedi, G. E. Murch, I. V. Belova and T. Fiedler, *Mater Des*, 2019, **168**, 107652.

97 J. Fu, Q. Liu, K. Liufu, Y. Deng, J. Fang and Q. Li, *Thin-Walled Structures*, 2019, **135**, 400–413.

98 B. C. Chen, M. Zou, G. M. Liu, J. F. Song and H. X. Wang, *Int J Impact Eng*, 2018, **115**, 48–57.

99 F. Duddeck, S. Hunkeler, P. Lozano, E. Wehrle and D. Zeng, *Structural and Multidisciplinary Optimization*, 2016, **54**, 415–428.

100 G. Sun, T. Liu, X. Huang, G. Zhen and Q. Li, *Eng Struct*, 2018, **155**, 235–250.

101 M. Abada and A. Ibrahim, *Compos B Eng*, 2020, **183**, 107720.

102 K. Wang, Y. Liu, J. Wang, J. Xiang, S. Yao and Y. Peng, *Eng Struct*, 2022, **254**, 113907.

103 D. Karagiozova, D. W. Shu, G. Lu and X. Xiang, *Int J Mech Sci*, 2016, **105**, 102–116.

104 R. A. Alia, W. J. Cantwell, G. S. Langdon, S. C. K. Yuen and G. N. Nurick, *Compos B Eng*, 2014, **61**, 127–135.

105 S. Li, X. Guo, J. Liao, Q. Li and G. Sun, *Compos B Eng*, 2020, **196**, 108029.

106 A. G. Hanssen, M. Langseth and O. S. Hopperstad, *Int J Mech Sci*, 1999, **41**, 967–993.

107 S. Santosa and T. Wierzbicki, *Comput Struct*, 1998, **68**, 343–367.

108 F. Garai, G. Béres and Z. Weltsch, *Materials Science and Engineering A*, , DOI:10.1016/j.msea.2020.139743.

109 A. K. Toksoy, M. Tanoglu, M. Guden and I. W. Hall, *J Mater Sci*, 2004, **39**, 1503–1506.

110 S. Santosa and T. Wierzbicki, *Comput Struct*, 1998, **68**, 343–367.

111 L. Bonaccorsi, E. Proverbio and N. Raffaele, *J Mater Sci*, 2010, **45**, 1514–1522.

112 M. Li, S. Barbat, R. Baccouche, J. Belwafa and W. Lu, *Compos B Eng*, 2020, **193**, 108047.

113 F. Yang, M. Li and W. Lu, *Thin-Walled Structures*, 2020, **151**, 106716.

114 M. Li, S. Barbat, R. Baccouche, J. Belwafa and W. Lu, *Compos B Eng*, 2020, **193**, 108047.

115 G. Zhu, J. Liao, G. Sun and Q. Li, *Int J Impact Eng*, 2020, **141**, 103509.

116 J. F. Peters, M. Muthuswamy, J. Wibowo and A. Tordesillas, *Phys Rev E Stat Nonlin Soft Matter Phys*, 2005, **72**, 1–8.

117 T. V. Garza-Cruz and M. Nakagawa, *Granul Matter*, 2012, **14**, 309–318.

118 J. Atkinson, in *Encyclopedia of Geology*, Elsevier, 2005, vol. c, pp. 184–193.

119 A. Baroutaji, M. Sajjia and A.-G. Olabi, *Thin-Walled Structures*, 2017, **118**, 137–163.

120 I. Duarte, M. Vesenjak, L. Krstulović-Opara and Z. Ren, *Compos Struct*, 2015, **124**, 128–139.

121 I. Duarte, L. Krstulović-Opara and M. Vesenjak, *Compos Struct*, 2018, **192**, 184–192.

122 F. Yang, M. Li and W. Lu, *Thin-Walled Structures*, 2020, **151**, 106716.

123 M. Li, J. Li, S. Barbat, R. Baccouche and W. Lu, *Compos Struct*, 2018, **200**, 120–126.

124 S. P. Santosa, T. Wierzbicki, A. G. Hanssen and M. Langseth, *Int J Impact Eng*, 2000, **24**, 509–534.

125 A. K. Toksoy and M. Güden, *Thin-Walled Structures*, 2005, **43**, 333–350.

126 I. Duarte, L. Krstulović-Opara and M. Vesenjak, *Compos Struct*, 2015, **121**, 154–162.

127 R. D. Hussein, D. Ruan, G. Lu and I. Sbarski, *Compos Struct*, 2016, **140**, 166–179.

128 Q. Liu, J. Fu, J. Wang, J. Ma, H. Chen, Q. Li and D. Hui, *Compos B Eng*, 2017, **130**, 236–247.

129 F. Garai, G. Béres and Z. Weltsch, *Materials Science and Engineering A*, , DOI:10.1016/j.msea.2020.139743.

130 A. K. Toksoy, M. Tanoglu, M. Guden and I. W. Hall, *J Mater Sci*, 2004, **39**, 1503–1506.

131 M. Taherishargh, M. Vesenjak, I. V. Belova, L. Krstulović-Opara, G. E. Murch and T. Fiedler, *Mater Des*, 2016, **99**, 356–368.

132 L. Wang, B. Zhang, J. Zhang, Y. Jiang, W. Wang and G. Wu, *Thin-Walled Structures*, 2021, **160**, 107364.

133 X. Luo, J. yu Xu, L. Nie, Y. Gao, J. Zhu and W. Li, *Compos Struct*, 2015, **133**, 124–130.

134 X. Yang, T. An, Z. Wu, T. Zou, H. Song, J. Sha, C. He and N. Zhao, *Compos Struct*, 2020, **245**, 112357.

135 S. Li, X. Guo, J. Liao, Q. Li and G. Sun, *Compos B Eng*, 2020, **196**, 108029.

136 A. K. Toksoy and M. Güden, *Thin-Walled Structures*, 2005, **43**, 333–350.

137 H. Kavi, A. K. Toksoy and M. Guden, *Mater Des*, 2006, **27**, 263–269.

138 X. Zhang and G. Cheng, *Int J Impact Eng*, 2007, **34**, 1739–1752.

139 S. P. Santosa, T. Wierzbicki, A. G. Hanssen and M. Langseth, *Int J Impact Eng*, 2000, **24**, 509–534.

140 M. Taherishargh, M. Vesenjak, I. V. Belova, L. Krstulović-Opara, G. E. Murch and T. Fiedler, *Mater Des*, 2016, **99**, 356–368.

141 Y. Liu, T. A. Schaedler, A. J. Jacobsen, W. Lu, Y. Qiao and X. Chen, *Compos Struct*, 2014, **115**, 29–40.

142 Z. P. Wang and C. T. Sun, *Wave Motion*, 2002, **36**, 473–485.

143 Z. P. Wang and C. T. Sun, *Wave Motion*, 2002, **36**, 473–485.

144 V. S. Deshpande and N. A. Fleck, *Int J Impact Eng*, 2000, **24**, 277–298.

145 Y. Zhang, X. Ren, D. Han, X. Cheng, W. Jiang, X. G. Zhang, X. Y. Zhang and Y. M. Xie, *Int J Impact Eng*, 2022, **164**, 104193.

146 J. Fang, G. Sun, N. Qiu, N. H. Kim and Q. Li, *Structural and Multidisciplinary Optimization*, 2017, **55**, 1091–1119.

147 I. Duarte, L. Krstulović-Opara, J. Dias-de-Oliveira and M. Vesenjak, *Thin-Walled Structures*, 2019, **138**, 124–136.

148 A. R. C. Duarte, F. Mano, R. L. Reis and K. F. Jensen, *Langmuir*.

149 M. Taherishargh, M. Vesenjak, I. V. Belova, L. Krstulović-Opara, G. E. Murch and T. Fiedler, *Mater Des*, 2016, **99**, 356–368.

150 E. Linul, D. Lell, N. Movahedi, C. Codrean and T. Fiedler, *Compos B Eng*, 2019, **167**, 122–134.

151 L. Pan, Y. Yang, M. U. Ahsan, D. D. Luong, N. Gupta, A. Kumar and P. K. Rohatgi, *Materials Science and Engineering: A*, 2018, **731**, 413–422.

152 M. Su, H. Wang and H. Hao, *Compos Struct*, 2019, **226**, 111197.

153 G. Sun, T. Liu, X. Huang, G. Zheng and Q. Li, *Eng Struct*, 2018, **155**, 235–250.

154 Z. Yi, H. Si-yuan, L. Jia-gui, Z. Wei, G. Xiao-lu and Y. Jin, *Compos Struct*, 2019, **220**, 451–459.

155 J. Fang, Y. Gao, X. An, G. Sun, J. Chen and Q. Li, *Compos B Eng*, 2016, **92**, 338–349.

156 G. Sun, Z. Wang, H. Yu, Z. Gong and Q. Li, *Compos Struct*, 2019, **209**, 535–547.

157 Y. Zhang, G. Sun, G. Li, Z. Luo and Q. Li, *Mater Des*, 2012, **38**, 99–109.

158 H. Wang, M. Su and H. Hao, *Compos Struct*, 2020, **239**, 112039.

159 N. Movahedi, G. E. Murch, I. V. Belova and T. Fiedler, *J Alloys Compd*, 2020, **822**, 153465.

160 G. Zhu, J. Liao, G. Sun and Q. Li, *Int J Impact Eng*, 2020, **141**, 103509.

161 A. G. Mamalis, G. L. Viegelahn, D. E. Manolakos and W. Johnson, *Int J Impact Eng*, 1986, **4**, 117–126.

162 T. Ghanbari Ghazijahani, H. Jiao and D. Holloway, *Thin-Walled Structures*, 2014, **80**, 13–21.

163 T. Ghanbari Ghazijahani, H. Jiao and D. Holloway, *Thin-Walled Structures*, 2015, **92**, 48–54.

164 AMAZIGO JC and BIDIANSKY B, *ASME Pap*, 1971, 179–184.

165 W. Guggenberger, *Thin-Walled Structures*, 1995, **23**, 351–366.

166 A. Khamlichi, M. Bezzazi and A. Limam, *Thin-Walled Structures*, 2004, **42**, 1035–1047.

167 B. Prabu, A. V. Raviprakash and A. Venkatraman, *Thin-Walled Structures*, 2010, **48**, 639–649.

168 K. R. F. Andrews, G. L. England and E. Ghani, *Int J Mech Sci*, 1983, **25**, 687–696.

169 K. Yang, S. Xu, S. Zhou, J. Shen and Y. M. Xie, *Thin-Walled Structures*, 2017, **112**, 31–40.

170 N. S. Ha, G. Lu and X. Xiang, *Int J Mech Sci*, 2018, **148**, 409–421.

171 Y. Liu, T. A. Schaedler, A. J. Jacobsen, W. Lu, Y. Qiao and X. Chen, *Compos Struct*, 2014, **115**, 29–40.

172 A. K. De, J. G. Speer, D. K. Matlock, D. C. Murdock, M. C. Mataya and R. J. Comstock, *Metallurgical and Materials Transactions A*, 2006, **37**, 1875–1886.

173 A. K. De, J. G. Speer, D. K. Matlock, D. C. Murdock, M. C. Mataya and R. J. Comstock, *Metallurgical and Materials Transactions A*, 2006, **37**, 1875–1886.

174 D. Camilleri, D. Mackenzie and R. Hamilton, *Proceedings of the Institution of Mechanical Engineers, Part E: Journal of Process Mechanical Engineering*, 2007, **221**, 89–100.

175 G. Sun, H. Yu, Z. Wang, Z. Xiao and Q. Li, *Int J Mech Sci*, 2019, **150**, 767–783.

176 W. Zhang, S. Yin, T. X. Yu and J. Xu, *Int J Impact Eng*, 2019, **125**, 163–172.

177 NSC Injury Facts, *National Safety Council (NSC)*, 2022.

178 S. Umale, C. Deck, N. Bourdet, P. Dhumane, L. Soler, J. Marescaux and R. Willinger, *J Mech Behav Biomed Mater*, 2013, **17**, 22–33.

179 S. Arumugam, A. Al-Hassani, A. El-Menyar, H. Abdelrahman, A. Parchani, R. Peralta, A. Zarour and H. Al-Thani, *J Emerg Trauma Shock*, 2015, **8**, 193–198.

180 Y. Shao, D. Zou, Z. Li, L. Wan, Z. Qin, N. Liu, J. Zhang, L. Zhong, P. Huang and Y. Chen, *PLoS One*, , DOI:10.1371/journal.pone.0052366.

181 D. Rangaswamy and K. Sud, *Nephrology*, 2018, 23, 969–980.

182 B. J. Stewart, J. R. Ferdinand, M. D. Young, T. J. Mitchell, K. W. Loudon, A. M. Riding, N. Richoz, G. L. Frazer, J. U. L Staniforth, F. A. Vieira Braga, R. A. Botting, D.-M. Popescu, R. Vento-Tormo, E. Stephenson, A. Cagan, S. J. Farndon, K. Polanski, M. Efremova, K. Green, M. Del Castillo Velasco-Herrera, C. Guzzo, G. Collord, L. Mamanova, T. Aho, J. N. Armitage, A. C. P Riddick, I. Mushtaq, S. Farrell, D. Rampling, J. Nicholson, A. Filby, J. Burge, S. Lisgo, S. Lindsay, M. Bajenoff, A. Y. Warren, G. D. Stewart, N. Sebire, N. Coleman, M. Haniffa, S. A. Teichmann, S. Behjati and M. R. Clatworthy, *Spatiotemporal immune zonation of the human kidney*, .

183 B. B. Lake, R. Menon, S. Winfree, Q. Hu, R. M. Ferreira, K. Kalhor, D. Barwinska, E. A. Otto, M. Ferkowicz, D. Diep, N. Plongthongkum, A. Knoten, S. Urata, L. H. Mariani, A. S. Naik, S. Eddy, B. Zhang, Y. Wu, D. Salamon, J. C. Williams, X. Wang, K. S. Balderrama, P. J. Hoover, E. Murray, J. L. Marshall, T. Noel, A. Vijayan, A. Hartman, F. Chen, S. S. Waikar, S. E. Rosas, F. P. Wilson, P. M. Palevsky, K. Kiryluk, J. R. Sedor, R. D. Toto, C. R. Parikh, E. H. Kim, R. Satija, A. Greka, E. Z. Macosko, P. V. Kharchenko, J. P. Gaut, J. B. Hodgin, R. Knight, S. H. Lecker, I. Stillman, A. A. Amodu, T. Ilori, S. Maikhor, I. Schmidt, G. M. McMahon, A. Weins, N. Hacohen, L. Bush, A. Gonzalez-Vicente, J. Taliercio, J. O'toole, E. Poggio, L. Cooperman, S. Jolly, L. Herlitz, J. Nguyen, E. Palmer, D. Sendrey, K. Spates-Harden, P. Appelbaum, J. M. Barasch, A. S. Bomback, V. D. D'Agati, K. Mehl, P. A. Canetta, N. Shang, O. Balderes, S. Kudose, L. Barisoni, T. Alexandrov, Y. Cheng, K. W. Dunn, K. J. Kelly, T. A. Sutton, Y. Wen, C. P. Corona-Villalobos, S. Menez, A. Rosenberg, M. Atta, C. Johansen, J. Sun, N. Roy, M. Williams, E. U. Azeloglu, C. He, R. Iyengar, J. Hansen, Y. Xiong, B. Rovin, S. Parikh, S. M. Madhavan, C. R. Anderton, L. Pasa-Tolic, D. Velickovic, O. Troyanskaya, R. Sealfon, K. R. Tuttle, Z. G. Laszik, G. Nolan, M. Sarwal, K. Anjani, T. Sigdel, H. Ascani, U. G. J.

Balis, C. Lienczewski, B. Steck, Y. He, J. Schaub, V. M. Blanc, R. Murugan, P. Randhawa, M. Rosengart, M. Tublin, T. Vita, J. A. Kellum, D. E. Hall, M. M. Elder, J. Winters, M. Gilliam, C. E. Alpers, K. N. Blank, J. Carson, I. H. De Boer, A. L. Dighe, J. Himmelfarb, S. D. Mooney, S. Shankland, K. Williams, C. Park, F. Dowd, R. L. McClelland, S. Daniel, A. N. Hoofnagle, A. Wilcox, S. Bansal, K. Sharma, M. Venkatachalam, G. Zhang, A. Pamreddy, V. R. Kakade, D. Moledina, M. M. Shaw, U. Ugwuowo, T. Arora, J. Ardayfio, J. Bebiak, K. Brown, C. E. Campbell, J. Saul, A. Shpigel, C. Stutzke, R. Koewler, T. Campbell, L. Hayashi, N. Jefferson, R. Pinkeney, G. V. Roberts, M. T. Eadon, P. C. Dagher, T. M. El-Achkar, K. Zhang, M. Kretzler and S. Jain, *Nature*, 2023, **619**, 585–594.

184 A. Karimi and A. Shojaei, *IRBM*, 2017, **38**, 292–297.

185 A. Zuk and J. V. Bonventre, *Annu Rev Med*, 2016, **67**, 293–307.

186 Y. Kirita, H. Wu, K. Uchimura, P. C. Wilson and B. D. Humphreys, , DOI:10.1073/pnas.2005477117/-/DCSupplemental.

187 T. D. M. D. ; F. T. C. M. D. ; R. B. J. M. D. ; W. R. E. M. D. ; F. R. P. M. D. , PH. D. MARTIN, .

188 P. G. R. Teixeira, C. Georgiou, K. Inaba, J. DubBose, D. Plurad, L. S. Chan, C. Toms, T. T. Noguchi and D. Demetriades, *Journal of Trauma - Injury, Infection and Critical Care*, 2009, **67**, 1259–1264.

189 K. Raghavendran, B. A. Davidson, J. D. Helinski, C. J. Marschke, P. Manderscheid, J. A. Woytash, R. H. Notter and P. R. Knight, *Anesth Analg*, 2005, **101**, 1482–1489.

190 T. A. Schaedler, A. J. Jacobsen, A. Torrents, A. E. Sorensen, J. Lian, J. R. Greer, L. Valdevit and W. B. Carter, *Ultralight Metallic Microlattices*, 2011, vol. 24.

191 M. Avalle, G. Belingardi and R. Montanini, *Characterization of polymeric structural foams under compressive impact loading by means of energy-absorption diagram*, 2001, vol. 25.

192 L. Gong, S. Kyriakides and W. Y. Jang, *Int J Solids Struct*, 2005, **42**, 1355–1379.

193 S. Rowson, S. M. Duma, R. M. Greenwald, J. G. Beckwith, J. J. Chu, K. M. Guskiewicz, J. P. Mihalik, J. J. Crisco, B. J. Wilcox, T. W. Mcallister, A. C. Maerlender, S. P. Broglio, B. Schnebel, S. Anderson and P. G. Brolinson, *J Neurosurg*, 2014, **120**, 919–922.

194 L. Bin Tan, K. M. Tse, H. P. Lee, V. B. C. Tan and S. P. Lim, *Int J Impact Eng*, 2012, **50**, 99–112.

195 I. R. Casson, D. C. Viano, J. W. Powell and E. J. Pellman, *Sports Health*, 2010, **2**, 471–483.

196 I. S. Scher, R. M. Greenwald and N. Petrone, *Snow Sports Trauma and Safety*, .

197 T. J. Dickson, S. Trathen, F. A. Terwiel, G. Waddington and R. Adams, *Scand J Med Sci Sports*, 2017, **27**, 236–244.

198 M. Li, J. Li, S. Barbat, R. Baccouche and W. Lu, *Compos Struct*, 2018, **200**, 120–126.

199 M. Li and W. Lu, *AIP Adv*, , DOI:10.1063/1.4984231.

200 Y. Zhang, M. Li, Y. Gao, B. Xu and W. Lu, *Nanoscale*, 2018, **10**, 18444–18450.

201 F. Yang, M. Li and W. Lu, *Thin-Walled Structures*, , DOI:10.1016/j.tws.2020.106716.

202 B. X. G. Designed Research; Y and Y. Z. G. Performed Research; Y, *MICHIGAN STATE UNIVERSITY LIBRARIES SERIALS ACQUISITIONS*, 2020, **117**, 25246–25253.

203 B. Xu, X. Chen, W. Lu, C. Zhao and Y. Qiao, *Appl Phys Lett*, , DOI:10.1063/1.4878097.

204 C. D. Warden, Y.-C. Yuan and X. Wu, *Optimal Calculation of RNA-Seq Fold-Change Values*, 2013, vol. 2.

205 K. J. Livak and T. D. Schmittgen, *Methods*, 2001, **25**, 402–408.

206 Y. Zhang, M. Li, Y. Gao, B. Xu and W. Lu, *Nanoscale*, 2018, **10**, 18444–18450.

207 Y. Gao, M. Li, C. Zhan, H. Zhang, M. Yin, W. Lu and B. Xu, *Advanced Materials*, , DOI:10.1002/adma.202303759.

208 Y. Gao, M. Li, H. Zhang, Y. Zhang, W. Lu and B. Xu, *Matter*, 2022, **5**, 266–280.

209 M. Li, C. Zhan and W. Lu, *Appl Phys Lett*, , DOI:10.1063/5.0068910.

210 L. Xu, M. Li and W. Lu, *Langmuir*, 2019, **35**, 14505–14510.

211 B. Majhy, P. Priyadarshini and A. K. Sen, *RSC Adv*, 2021, **11**, 15467–15476.

212 G. B. Blanchard, A. J. Kabla, N. L. Schultz, L. C. Butler, B. Sanson, N. Gorfinkiel, L. Mahadevan and R. J. Adams, *Nat Methods*, 2009, **6**, 458–464.

213 O. Campàs, *Semin Cell Dev Biol*, 2016, 55, 119–130.

214 K. Sugimura, P. F. Lenne and F. Graner, *Development (Cambridge)*, 2016, **143**, 186–196.

215 T. Mammoto and D. E. Ingber, *Development*, 2010, 137, 1407–1420.

216 C. P. Heisenberg and Y. Bellaïche, *Cell*, 2013, 153, 948.

217 D. C. Silvestrea, G. A. Gilb, N. Tomasinic, D. F. Bussolinod and B. L. Caputto, *PLoS One*, , DOI:10.1371/journal.pone.0009544.

218 H. Li, Y. Chen, J. Zhang, Y. Lin, Z. Yang, J. Tan and W. Qiao, *Int J Mol Med*, , DOI:10.3892/ijmm.2021.4889.

219 B. Ying, H. Fan, F. Wen, D. Xu, D. Liu, D. Yang, G. Chen, L. Dou and F. Jiang, *Biochem Biophys Res Commun*, 2006, **347**, 369–372.

220 H. Van Dam and M. Castellazzi, *Distinct roles of Jun : Fos and Jun : ATF dimers in oncogenesis*, .

221 N. Niazy, L. Mrozek, M. Barth, M. B. Immohr, N. Kalampokas, D. Saeed, H. Aubin, Y. Sugimura, R. Westenfeld, U. Boeken, A. Lichtenberg and P. Akhyari, *J Clin Med*, , DOI:10.3390/jcm10214856.

222 B. C. Jiang, T. Y. Ding, C. Y. Guo, X. H. Bai, D. L. Cao, X. B. Wu, W. L. Sha, M. Jiang, L. J. Wu and Y. J. Gao, *Advanced Science*, , DOI:10.1002/advs.202201300.

223 Y. Li, Y. Zhu, S. Feng, Y. Ishida, T. P. Chiu, T. Saito, S. Wang, D. K. Ann and J. hsiung J. Ou, *Cell Rep*, , DOI:10.1016/j.celrep.2021.110284.

224 S. Mahner, C. Baasch, J. Schwarz, S. Hein, L. Wölber, F. Jänicke and K. Milde-Langosch, *Br J Cancer*, 2008, **99**, 1269–1275.

225 *Inflammation and Immunity in Depression Basic Science and Clinical Applications*, .

226 F. POCIOT, J. MØLVIG, L. WOGENSEN, H. WORSAAE and J. NERUP, *Eur J Clin Invest*, 1992, **22**, 396–402.

227 S. L. Masters, A. Simon, I. Aksentijevich and D. L. Kastner, *Annu Rev Immunol*, 2009, 27, 621–668.

228 J. R. Lukens, P. Gurung, P. Vogel, G. R. Johnson, R. A. Carter, D. J. McGoldrick, S. R. Bandi, C. R. Calabrese, L. Vande Walle, M. Lamkanfi and T. D. Kanneganti, *Nature*, 2014, **516**, 246–249.

229 D. Ai, Y. Zhao, Q. Wang and C. Li, *Int J Impact Eng*, 2019, **126**, 135–146.

230 P. Xu, Y. Yu, K. Li and X. Wu, *Polym Test*, 2018, **69**, 431–436.

231 F. Lu, Y. Lin, X. Wang, L. Lu and R. Chen, *Int J Impact Eng*, 2015, **79**, 95–101.

232 P. Wang, S. Xu, Z. Li, J. Yang, C. Zhang, H. Zheng and S. Hu, *Materials Science and Engineering: A*, 2015, **620**, 253–261.

233 Y. Tang, W. Zhang, X. Jiang, J. Zhao, W. Xie and T. Chen, *Compos B Eng*, , DOI:10.1016/j.compositesb.2022.109885.

234 F. Rahimidehgolan and W. Altenhof, *Compos B Eng*, 2023, 253.

235 M. A. Islam, A. D. Brown, P. J. Hazell, M. A. Kader, J. P. Escobedo, M. Saadatfar, S. Xu, D. Ruan and M. Turner, *Int J Impact Eng*, 2018, **114**, 111–122.

236 A. N. Pratomo, S. P. Santosa, L. Gunawan, D. Widagdo and I. S. Putra, *Int J Impact Eng*, , DOI:10.1016/j.ijimpeng.2020.103699.

237 F. B. Mendonça, G. S. Urgessa, R. L. Dutra, R. F. B. Gonçalves, K. Iha and J. A. F. F. Rocco, *Acta Scientiarum - Technology*, , DOI:10.4025/actascitechnol.v42i1.40020.

238 S. Bloodworth-Race, R. Critchley, R. Hazael, A. Peare and T. Temple, *Heliyon*, , DOI:10.1016/j.heliyon.2021.e06990.

239 Y. Cheng, M. Liu, P. Zhang, W. Xiao, C. Zhang, J. Liu and H. Hou, *Int J Mech Sci*, 2018, **145**, 378–388.

240 K. A. Brekken, A. Reyes, T. Børvik, T. Berstad and M. Langseth, *Applied Sciences (Switzerland)*, 2020, **10**, 1–36.

241 H. Andami and H. Toopchi-Nezhad, *International Journal of Protective Structures*, 2020, **11**, 109–130.

242 Y. Li, X. Ren, X. Zhang, Y. Chen, T. Zhao and D. Fang, *Compos Struct*, , DOI:10.1016/j.compstruct.2020.113317.